

Hiroshima University Doctoral Thesis

**First Principal Calculation and Angle-resolved
Photoemission Spectroscopy Study of Ultrathin
Cr₂O₃ and CrTe₂ Films**

(第一原理計算と角度分解光電子分光による Cr₂O₃ 超薄膜
および CrTe₂ 薄膜の研究)

Department of Physics

Graduate School of Science

Hiroshima University

Name: Xueyao Hou

Table of Contents

1. Main thesis

First Principal Calculation and Angle-resolved Photoemission Spectroscopy
Study of Ultrathin Cr₂O₃ and CrTe₂ Films

(第一原理計算と角度分解光電子分光による Cr₂O₃ 超薄膜および CrTe₂ 薄膜の研究)

2. Article

Observation of mid-gap states emerging in the O-terminated interface of Cr₂O₃/graphene: A combined study of ab initio prediction and photoemission analysis

Xueyao Hou, Mansuer Wumiti, Shiv Kumar, Kenya Shimada, Masahiro Sawada

Applied Surface Science, 594 (2022), 153416, 1-10.

Main Thesis

HIROSHIMA UNIVERSITY

Graduate School of Science

DOCTORAL THESIS

First Principal Calculation and Angle-resolved Photoemission Spectroscopy

Study of Ultrathin Cr₂O₃ and CrTe₂ Films

(第一原理計算と角度分解光電子分光による Cr₂O₃ 超薄膜および CrTe₂ 薄膜の研究)

Xueyao Hou

June 2022

Contents

Contents	I
Abstract	- 1 -
Chapter 1 Background	- 3 -
1.1 Multiferroic Materials	- 3 -
1.2 Graphene	- 4 -
1.3 Cr ₂ O ₃	- 9 -
1.3.1 Crystal Structure	- 9 -
1.3.2 Surface Structure.....	- 13 -
1.3.3 Cr ₂ O ₃ -Based Interface.....	- 14 -
1.4 CrTe ₂	- 15 -
1.5 Conclusion	- 17 -
Chapter 2 Experiment Details and DFT Calculation	- 19 -
2.1 Background.....	- 19 -
2.2 Sample Fabrication and Structure Characterization.....	- 19 -
2.2.1 Molecular Beam Epitaxy (MBE)	- 19 -
2.2.2 Auger Electron Spectroscopy (AES)	- 20 -
2.2.3 Low-Energy Electron Diffraction (LEED)	- 22 -
2.2.4 X-Ray Absorption Spectroscopy (XAS).....	- 23 -
2.3 Angle-Resolved Photoemission Spectroscopy (ARPES).....	- 24 -
2.3.1 Photoelectronic Effect.....	- 24 -
2.3.2 Introduction of Electron Spectroscopy	- 25 -
2.3.3 Basic Principles of ARPES	- 27 -
2.3.4 Three Step Model.....	- 30 -
2.3.5 Matrix Element Effect.....	- 34 -
2.3.6 Ratable High-Resolution ARPES Station in HiSOR	- 36 -

2.4 First-Principal Calculations	- 39 -
2.4.1 Density Functional Theory (DFT)	- 40 -
2.4.2 Wave-Function-Based Methods.....	- 46 -
2.4.3 Hartree-Fock Method.....	- 46 -
2.4.4 Drawback of First Principles Calculation	- 47 -
2.4.5 VASP Programs	- 49 -
Chapter 3 DFT Calculation of Cr₂O₃/Graphene Interface	- 51 -
3.1 Introduction.....	- 51 -
3.2 General Calculation Parameters.....	- 51 -
3.3 Structure Modeling of Interfaces	- 54 -
3.3 Total Energy and Density of States.....	- 55 -
3.4 Density of States	- 57 -
3.5 Band Structure	- 60 -
3.6 Conclusion	- 65 -
Chapter 4 ARPES Study of Cr₂O₃/Graphene Interface	- 67 -
4.1 Introduction.....	- 67 -
4.2 Experimental Methods.....	- 67 -
4.3 Sample Characterization	- 68 -
4.4 ARPES Experiment	- 70 -
4.5 Discussion.....	- 77 -
4.6 Conclusion	- 80 -
Chapter 5 DFT Calculation Study of Ultrathin CrTe₂ Films.....	- 83 -
5.1 Introduction.....	- 83 -
5.2 Simulation Parameters	- 84 -
5.3 Magnetic Configuration.....	- 85 -
5.4 CrTe ₂ /Graphene	- 88 -
5.5 Conclusion	- 91 -

Chapter 6 Summary	- 93 -
Reference	- 95 -
Acknowledgement.....	- 101 -

Abstract

The multiferroic materials have attract wide attention due to its controllable ferroic properties by additional parameters of non-conjugate external fields. Thereinto, Cr_2O_3 would be a great research target for its intrinsic multiferroic characteristic. In this work, we use first-principles density functional theory (DFT) calculations and angle-resolved photoemission spectroscopy (ARPES) to study the band structure of $\text{Cr}_2\text{O}_3/\text{Gr}/\text{Ni}(111)$ heterostructure. Our calculations have shown that the electronic band structures are distinct between the O- and Cr-terminated interfaces of the $\text{Cr}_2\text{O}_3/\text{Gr}/\text{Ni}(111)$ heterostructure. An interesting spin-polarized mid-gap states are predicted to exist in the O-terminated model, whose spin direction can be flipped by reversing the substrate magnetization direction. In the ARPES experiments, we have observed the existence of such mid-gap band at the energy of ~ -0.20 eV in interface of Cr_2O_3 and graphene. The mid-gap band was further confirmed to have a Cr nature by resonance photoemission spectroscopy. Our findings indicate that one can control the spin-polarized mid-gap states in the antiferromagnetic Cr_2O_3 as well as the bandgap of graphene by interface engineering, paving the way for spintronic applications.

The calculation for CrTe_2 slabs is performed to examine the electronic structures and corresponding physical properties that can be compared with experiments. The effect of thickness, magnetic configuration and graphene buffer layer are all considered during calculation. We find that the thickness is crucial for its properties, the CrTe_2 slabs recovers to its bulk properties as thickness increases. Besides, the 1unit cell(UC) and 2UC slabs show a stronger spin-oscillation than that of others. With the AFM magnetic configuration, there will be an unusual unoccupied state at 3.5 eV above the E_F , which is distributed by the in-plane states of Cr 3*d* and Te 5*p* orbitals.

The graphene buffer layer will weaken the spin-oscillation of 1UC and 2UC films, and make it recovers to bulk properties.

Chapter 1 Background

1.1 Multiferroic Materials

Multiferroic materials is the materials with two or more ferroicities coexist(**Figure 1.1**[1]), now become one of the most popular topics of condensed matter physics due to its wide range of use in data-storage industries. Since giant magnetoresistance was observed on Fe/Cr superlattices [2], the fundamental application issues in high-density data storage area has been promoted rapidly. The coexistence and coupling of several order parameters introduce novel physical phenomena and offers possibilities for developing new devices, such as magnetic random-access memories (MRAMs), ferroelectric random-access memories (FeRAMs) and spintronic devices.

It's worth to point out that the most widely synthesized and researched multiferroics are originated from transitional metal oxides, which is strongly correlated electronic systems with coupling of spin, charge, orbitals and lattices. The magnetoelectric effect describes the coupling between magnetic and electric field, where the magnetization \mathbf{M} (electric polarization \mathbf{P}) develops as an electric(magnetic) field is applied. With consideration of the crystal symmetry, Curie predicted the Cr_2O_3 has the intrinsic magnetoelectric effect [3], which was confirmed in the experiment for the first time with a coupling efficient of $4.13\text{ps}\cdot\text{m}^{-1}$ [4]. However, it's very difficult to achieve magnetoelectric effect in single-phase compounds because the coupling is rather weak especially in room temperature. Considerable progress has been turn to the composite multiferroic materials that consist of a ferroelectric and a ferromagnetic constituent such as Fe/Cr superlattice [2]. By combining the thin film growth techniques and experimental methods for design of multiferroic materials, the new multiferroics are proven to be a rich source for investigation of

fundamental science of correlated electron system. In the case of single-phase multiferroics, the basic questions of the origin of multiferroics still remain, new theoretical way to better modulation of multiferroic coupling and finding robust room-temperature multiferroics are still challenging.

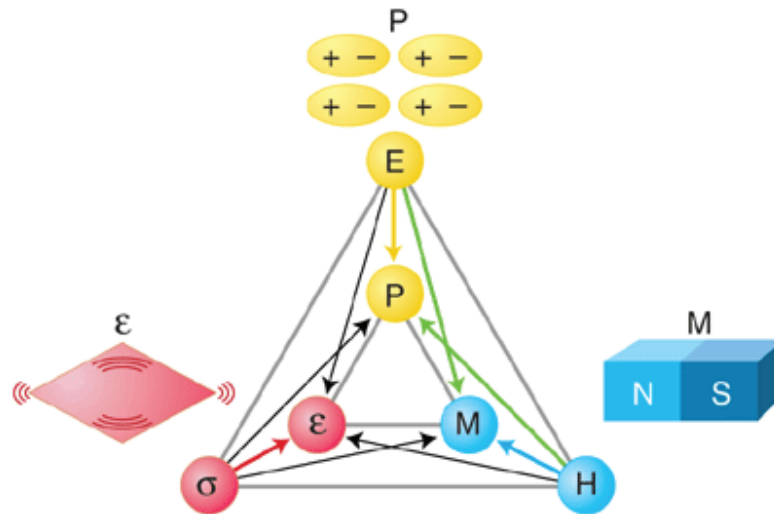


Figure 1.1 Relationship between ferroelectricity and magnetism [1]. Physical parameters of magnetization \mathbf{M} , electric polarization \mathbf{P} and strain σ , can respond to non-conjugate external fields through cross correlation.

1.2 Graphene

Graphene (Gr) has attracted considerable interest in the last past 20 years[5], due to its high electron mobility, massless Dirac fermions, anomalous half integer quantum Hall effect[6], remarkable optical properties [7], high intrinsic strength [8], superior thermal conductivity[9]. Having these characteristic electronic properties, graphene can be served as a promising material for electronic device applications. The novel effects of graphene are related to its structure and electronic structure. With sp^2 hybrids, the carbon atoms share electrons with their three neighbors

and form a honeycomb network of planar structure (**Figure 1.2**). The out-of-plane π bond is formed by p_z orbitals which are perpendicular to the planar structure. The π -bonds provide a weak van der Waals interaction between adjacent graphene layers. Furthermore, the p_z states of graphene forms linear band dispersions (Dirac cones) intersecting at the K and K' points in reciprocal space, where the density of states (DOS) is vanishing (**Figure 1.3**). The valence and conduction bands touch each other at the six topological singular points (Dirac points), and their linearity of dispersion is kept within the binding energy (BE) range of 1 eV around the Fermi level (E_F) [10]. And the conduction and valence bands are named as π and π^* band, respectively. The gapless Dirac points emerging in its band structure are the main reason of aforementioned extraordinary properties of graphene, which are protected by the time reversal symmetry, special inversion symmetry.

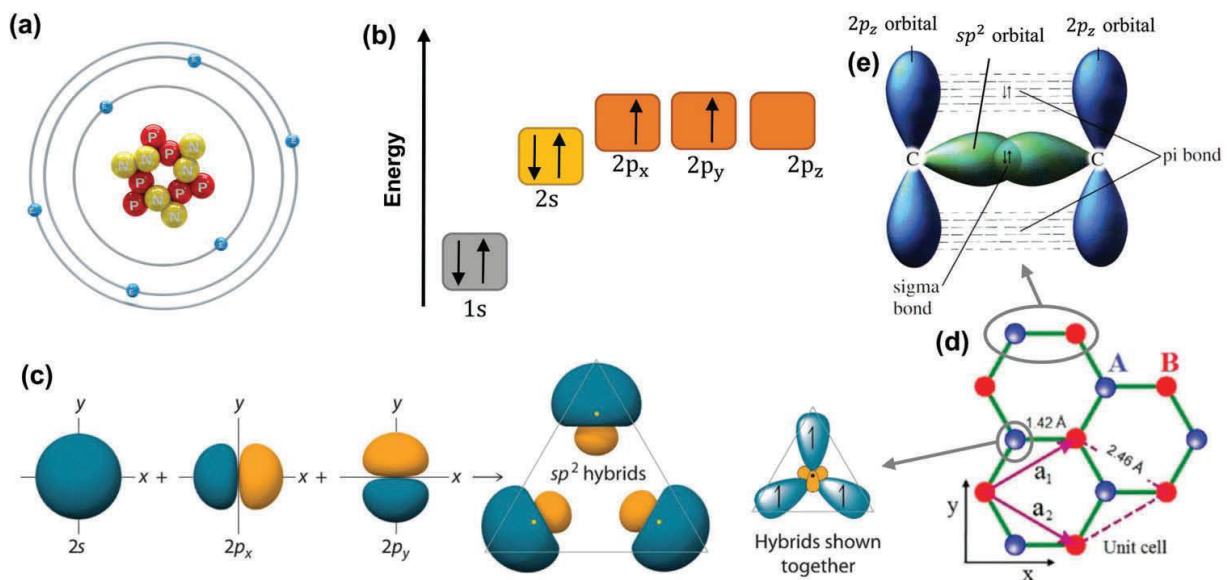


Figure 1.2 (a) Atomic structure and (b) Energy levels and orbital occupation of a carbon atom. (c) Schematic of sp^2 hybridization; (d) crystal lattice of graphene; and (e) bond formed by sp^2 hybridization.[11]

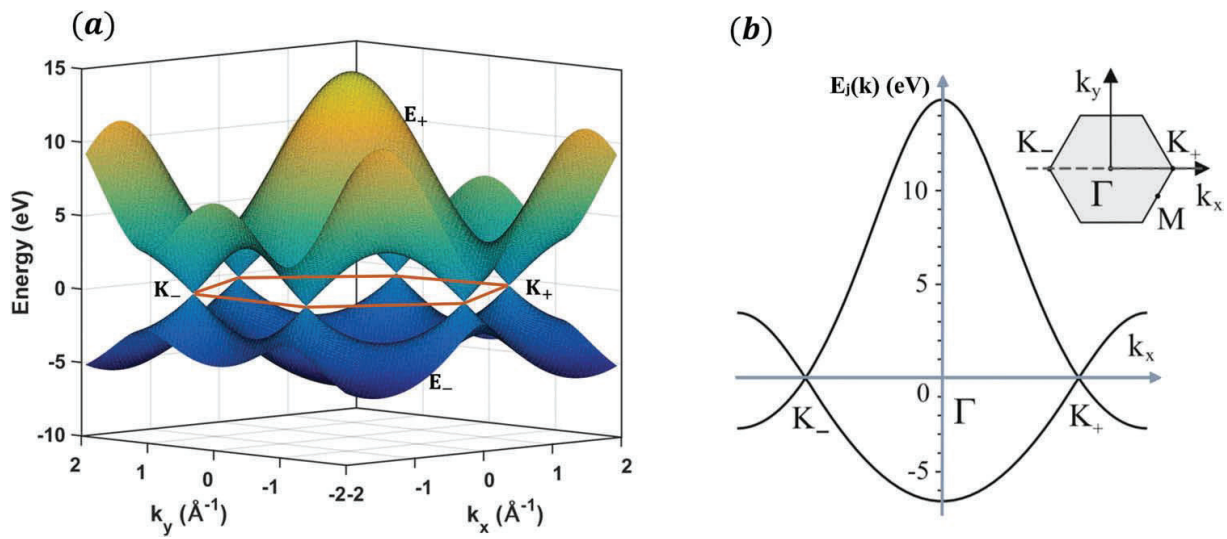


Figure 1.3 (a) Band structure of graphene with a tight-binding method. (b) Cross-section through the band structure, where the energy bands are plotted as a function of wave vector component k_x along the line $k_y = 0$. [11]

Nevertheless, the absence of a bandgap in pristine graphene limits its practical application. One promising approach is to break the inversion symmetry of graphene, and attempts in this direction have revealed unusual magnetic and optical properties[12]. By chemical functionalization with hydrogen and oxygen plasma, the hybridized orbital of graphene transforms from sp^2 to sp^3 , which can induce the bandgap opening(**Figure 1.4(a)**)[13]. By modulating the adsorbents, substrate materials, and surface termination, or by applying strain and electric field, one can manipulate the bandgap at the K and K' points in graphene-based heterostructures (**Figure 1.4 (b-e)**) [14-24]. In some cases, the adsorption site is also an important factor to open a gap in the electronic band structure[13].

Bandgap engineering of the K point is important for developing graphene-based devices, such as spin filters or field-effect transistors. Recently, substrate-induced bandgap opening has attracted considerable attention. Previous studies have shown that graphene is physisorbed and *p*-doped on Al, Cu, Ag, Au, and Pt substrates, whereas it is chemisorbed and *n*-doped on Co, Ni, and Pd [20-23]. In these heterostructures, *p*- and *n*- doping effects are induced by modification of the mid-gap states, which depends on the difference in work functions between the substrate and graphene. The graphene may hybridize with the metal d-band, and its electronic structure is strongly modified due to the interaction with substrate. Circular dichroism measurement of graphene shows a clear difference between the left and right polarization light for the transition from 1s to π^* bands, which suggests the π -orbitals of the graphene are magnetically polarized. The graphene can be fabricated on metal surface in ultra-high vacuum(UHV) using propylene with low pressures. One can easily distinguish the carbon of graphene from the carbide via AES carbon-to-nickel peak ratio and lineshape [25](**Figure 1.5**).

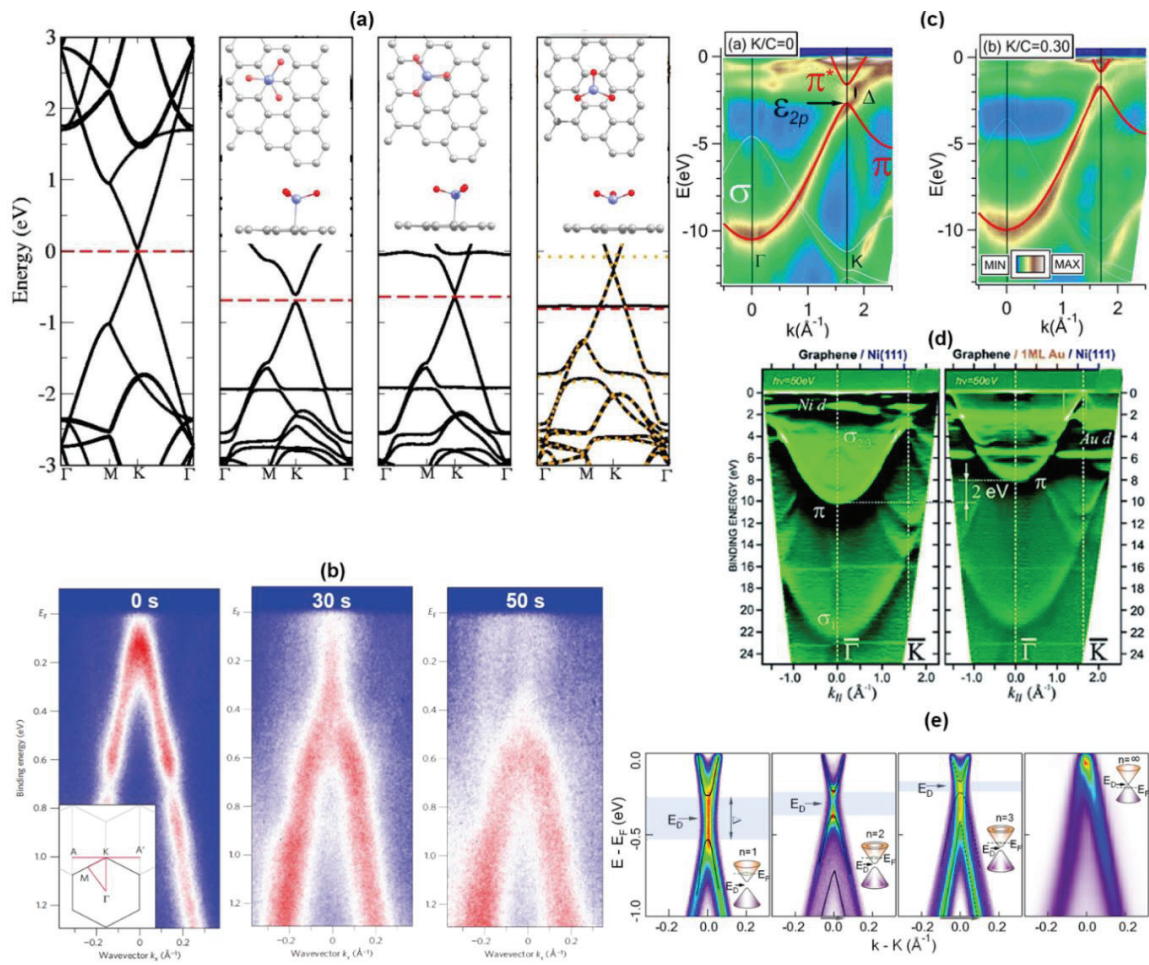


Figure 1.4 (a) Electronic band structure of graphene with different configuration of CrO_3 adsorbent[13]; (b) ARPES spectra of graphene with different dose of atomic hydrogen exposure[24]; (c) ARPES intensities of graphene doped by K[26]; (d) Au intercalation of graphene/Ni(111) [10]; (e) ARPES spectra of band-gap opening and decrease of the size as the graphene thickness increase [19].

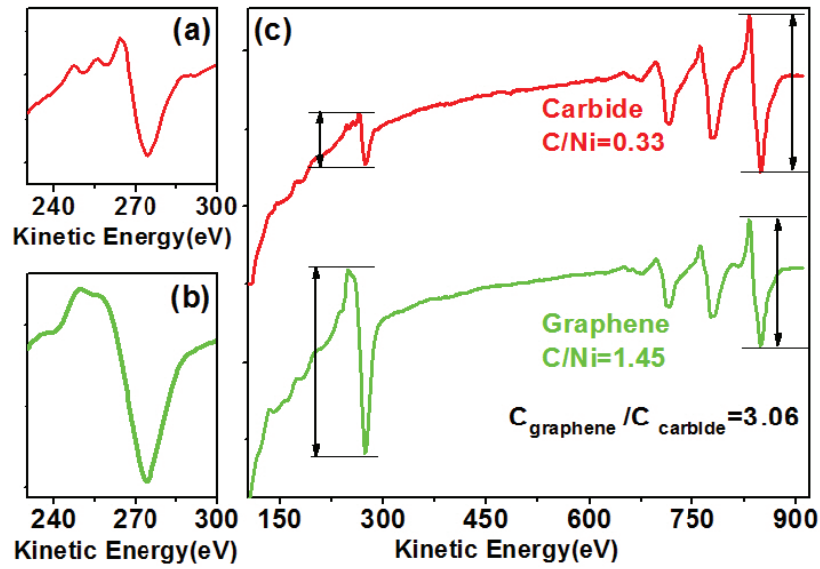


Figure 1.5 Auger electron spectra of monolayer carbide and monolayer graphene on Ni(111) surface.[25]

Graphene can act as an ideal buffer layer to reduce the interaction between epitaxial thin films and substrate. The graphene interfacial layer can provide a flat template for subsequent thin film growth, and forms a non-interacting interface[27]. It plays a vital role in passivating the dangling bonds of the substrate and induces different doping by different fabrication and post-treatment. By post-annealing, the atoms of epitaxial films migrated, embedded and intercalated under graphene honeycomb lattice has been widely observed [28]. The intercalation phenomena provide a method to get high-quality epitaxial thin films without extra interaction or strain with the substrate.

1.3 Cr₂O₃

1.3.1 Crystal Structure

The corundum- type Cr_2O_3 is a typical antiferromagnetic material with a high Néel temperature (~ 307 K) and trigonal corundum crystal structure(space group) (**Figure 1.6 (a)** [29]). The first- and second-nearest neighbor exchange coupling constants, J_1 and J_2 are predominant based on the neutron diffraction measurements[30]. The Cr^{3+} atoms are situated at octahedral sites of an O^{2-} sites. The Cr magnetic moments align antiferromagnetically in a spin configuration as shown in **Figure 1.6 (a)**. Due to its lack of inversion symmetry in the ground state, Cr_2O_3 was experimentally confirmed firstly as prototypical magnetoelectric (ME) materials [31]. In DFT, the band gap of Cr_2O_3 is significantly underestimated compared with the experimental value 3.31 eV [32]. The bandgap is sensitive to Hubbard correction method as illustrated in **Figure 1.6 (b)**[33]. The bandgap of Cr_2O_3 after consideration of $U < 4$ eV matches the experimental value well.

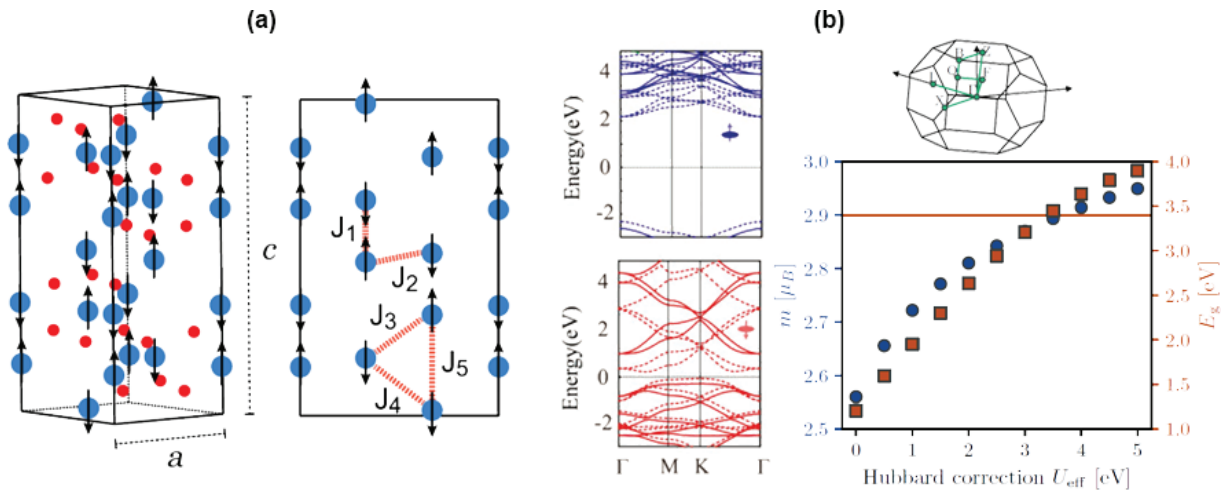


Figure 1.6 (a) schematics of the corundum-type Cr_2O_3 and the exchange coupling interactions of Cr_2O_3 along (110) -plane[29], (b) electronic band structure of Cr_2O_3 [34] and LSDA+ U ground states of Cr_2O_3 as a function of the Hubbard correction [33].

The room temperature multiferroicity (antiferromagnetic and magnetoelectricity) of Cr_2O_3 make it a promising material in magnetoelectric random memory (MERAM) Cells. Besides, the Cr_2O_3 is one of the most stable oxides whose physical properties (bandgap, magnetization) can be modified by dopants. Recent experimental studies have indicated that both bulk single crystals and thin-film Cr_2O_3 exhibit spontaneous ferromagnetic termination (boundary magnetism) **Figure 1.7 (a, c)** [35, 36], which is insensitive to surface roughness. Besides, the surface magnetization of Cr_2O_3 can be switched by electric field. The Pt/ Cr_2O_3 exhibits topological Hall effect below 6 nm around room temperature[37]. By controlling the ferromagnetic termination as a nonvolatile variable state through the ME-driven Néel vector, Cr_2O_3 -based antiferromagnetic (AFM) spintronic devices are superior in terms of robustness against magnetic perturbation and ultrafast dynamics [38].

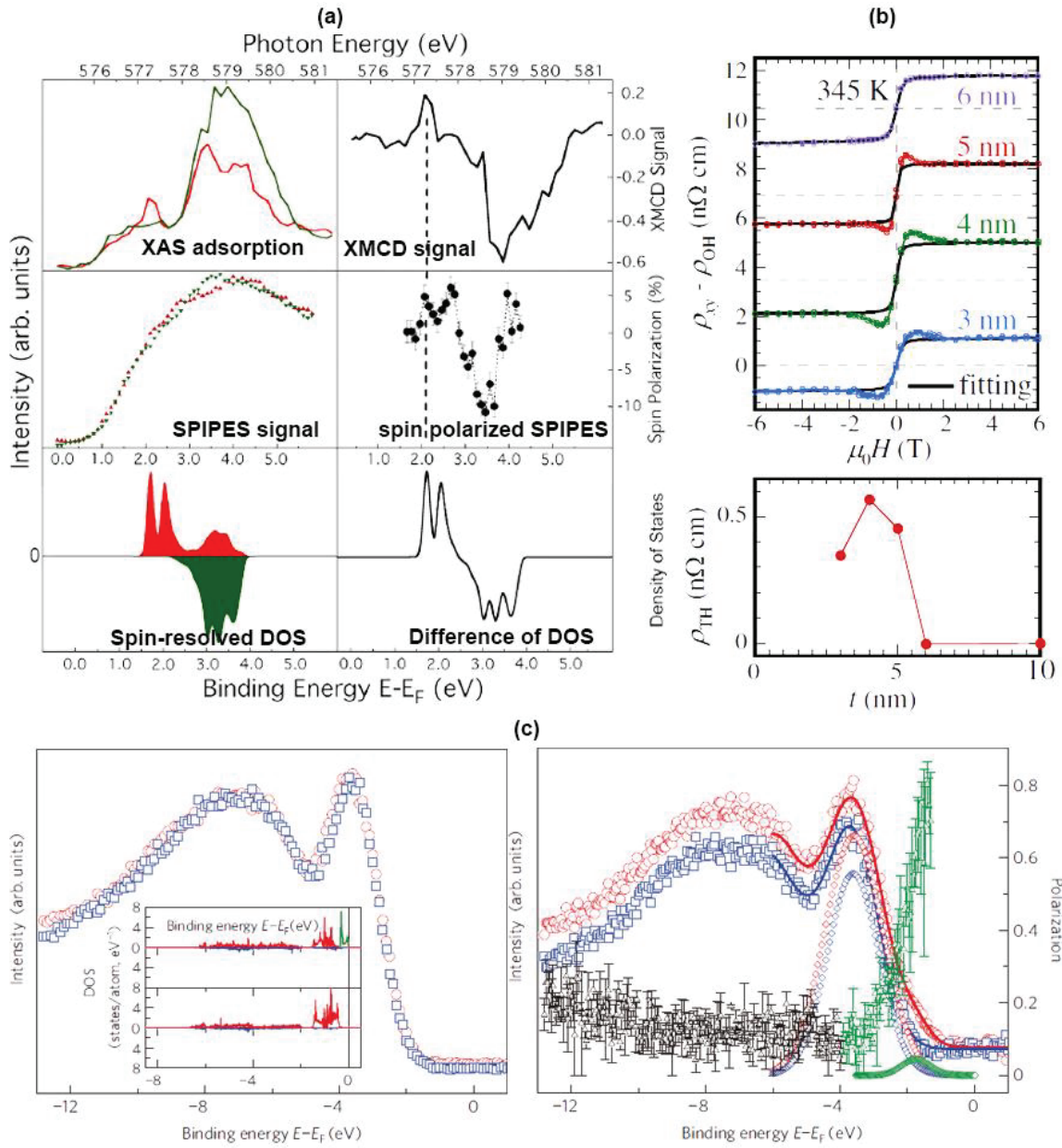


Figure 1.7 (a) XMCD, SPIES and spin-resolved DOS of Cr₂O₃ surface states [35]; (b) Hall resistivity of Pt/Cr₂O₃ bilayers on Al₂O₃(0001) with different thickness[37]; (c) Spin-polarized UPS measurement and layer-resolved DOS[36].

1.3.2 Surface Structure

Surface composition of Cr_2O_3 has been shown to vary with the film thickness and the growth conditions, such as oxygen pressure and temperature [25, 39, 40]. The surface of Cr_2O_3 crystal grown in ultra-high vacuum shows a common structure and the relevant surface should be metal-rich surface rather than oxygen-rich surface terminations. The phenomena has been confirmed by recent work of Kaspar group, in which Cr_2O_3 exhibit a full bilayer of Cr cations on the surface [41]. A consensus regarding ultrathin Cr_2O_3 films fabricated in UHV is that the topmost layers are compressed along the c direction **Figure 1.8(a, b)** [42]. The XPS spectra as shown in **Figure 1.8(c)** proved that surface oxygen coordinated to more Cr-atoms than in a bulk truncation. The occupation of the interstitial sites in the first surface layer could explain the presence of a different charge state for the surface oxygen, further supporting the structural model of **Figure 1.8(b)**.

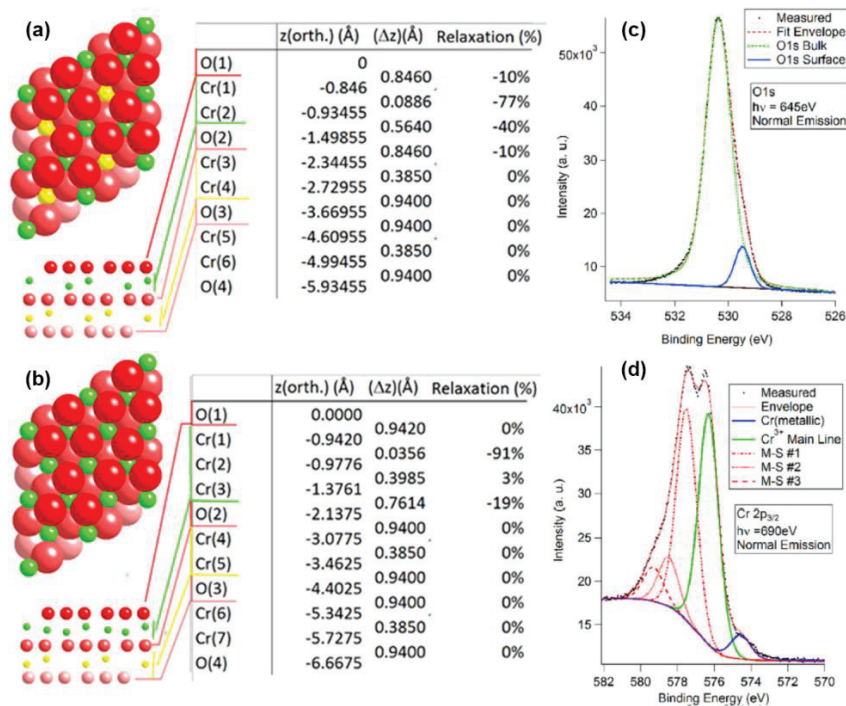


Figure 1.8 (a) and (b) are schematic of different Cr₂O₃(0001) surface atomic model after optimized the z-positions. (c) and (d) are O 1s and Cr 2p_{3/2} peak XPS characterization.[42]

1.3.3 Cr₂O₃-Based Interface

A direct investigation of the surface configuration of Cr₂O₃/Gr are shown **Figure 1.9**. Thus, the band structure of the Cr₂O₃/Gr heterostructure is likely to be specific to its surface or interface structure, which is distinct from that of Cr₂O₃ films or bulk crystals. From this perspective, angle-resolved photoemission spectroscopy (ARPES) is a suitable method to clarify the band structure of ultrathin Cr₂O₃/Gr directly. This can provide valuable information for the design of spintronic devices based on Cr₂O₃/Gr heterostructures. It has been predicted that an asymmetric bandgap opening exists between the K and K' valleys in AFM Cr₂O₃/Gr interface, which is originated from the staggered SOC of Cr₂O₃ (**Figure 1.9**)[38]. The band opening of graphene are strongly influenced by SOC. The SOC-induced symmetry broken allows modulation of Berry curvature and further determination of anomalous Hall conductance (AHC) of graphene. A previous scanning tunneling spectroscopy (STS) study reported that ultrathin α -Cr₂O₃ films growth on graphene covered Ni(111) have a narrower bandgap than bulk crystals [39]. Although there have been extensive studies, experimental observation of the interfacial band structure of Cr₂O₃/Gr is still lacking.

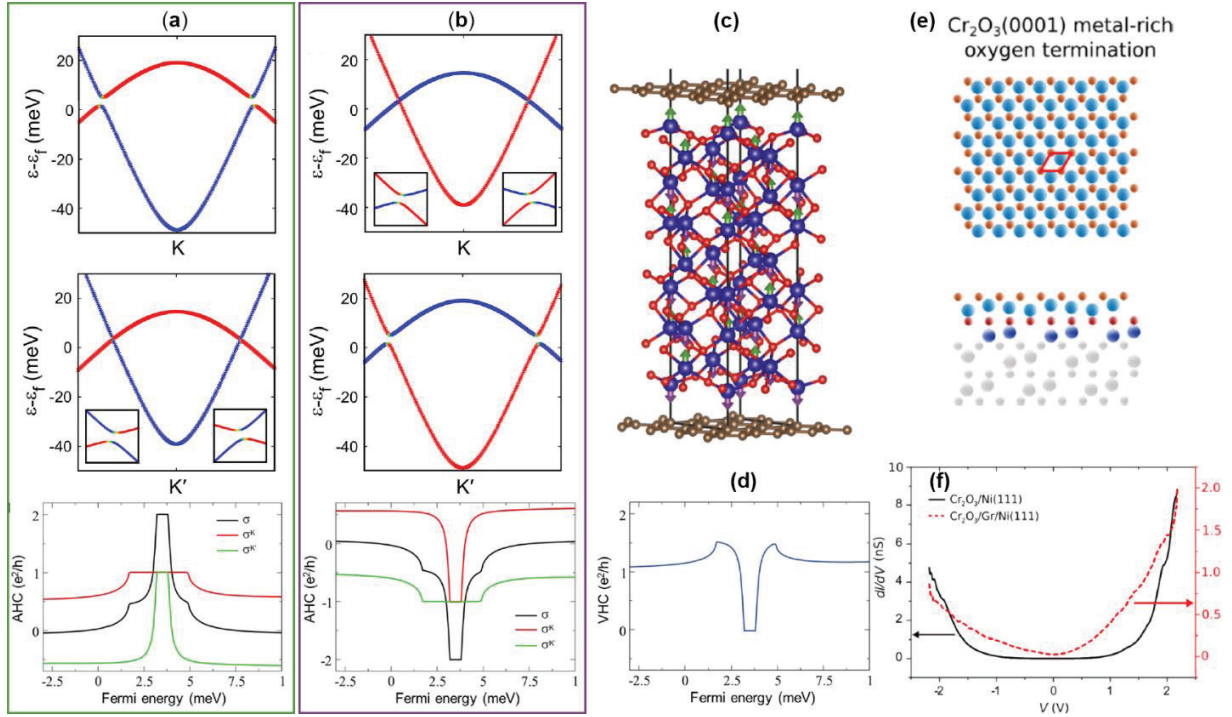


Figure 1.9 DFT-calculated band structure with SOC around K and K' points and corresponding anomalous Hall conductance (AHC) as a function of the Fermi energy. The (a) and (b) has reversed Néel vector in Chromia as illustrated in (c); (d) is the corresponding total AHC[38]. (e) is Cr_2O_3 /graphene interface model, (f) STS spectra of 0.8 nm Cr_2O_3 /graphene/Ni(111) and Cr_2O_3 /Ni(111) [39].

1.4 CrTe_2

Following the study of Cr_2O_3 as transition oxides has so many interesting properties, a natural question arises; what will happen if one substitutes the constituent of oxygen by another homologous (chalcogen) element X (X = S, Se, Te, et al). Considering the fabrication feasibility and crystal stability, we select CrTe_2 as an ideal research target. The bulk CrTe_2 is ferromagnetic materials with a Curie temperature(T_C) of 310 K, which make it promising in high- T_C ML

ferromagnets [43]. Recently, the exfoliated thin flakes of CrTe₂ were found to have an above room temperature T_C and an enhanced coercivity compared with its bulk. The ferromagnetism of CrTe₂ can persist up to 300 K. The 1T-CrTe₂, in which the Cr-rich hexagonal planes are sandwiched by Te-rich layers (**Figure 1.10 (a)**). Although CrTe₂ has strong itinerant ferromagnetism in bulk, its ML was predicted to be zigzag type AFM spin texture, the prediction is further proven in experiment with the magnetic easy axis in y - z plane (**Figure 1.10 (b-d)**)[44, 45]. However, the XMCD magnetic response of 1 ML CrTe₂ suggests that the ferromagnetism is kept for 1 ML CrTe₂ [46]. The magnetic structure 1 ML CrTe₂ may also depend on the fabrication methods, post-process, and vacuum level. Thus, it still remains debate for the magnetic configuration of 1 ML CrTe₂. Apart from this, a giant topological Hall effect was observed in CrTe₂/Bi₂Te₃ vdW heterostructure, which is originated from the coupling of CrTe₂ and CrTe₂ interface[47]. A systematically consideration of its magnetic configuration and related influence regarding electronic structure and physical properties of 1T-CrTe₂ in calculation is helpful to develop spintronics and storage devices.

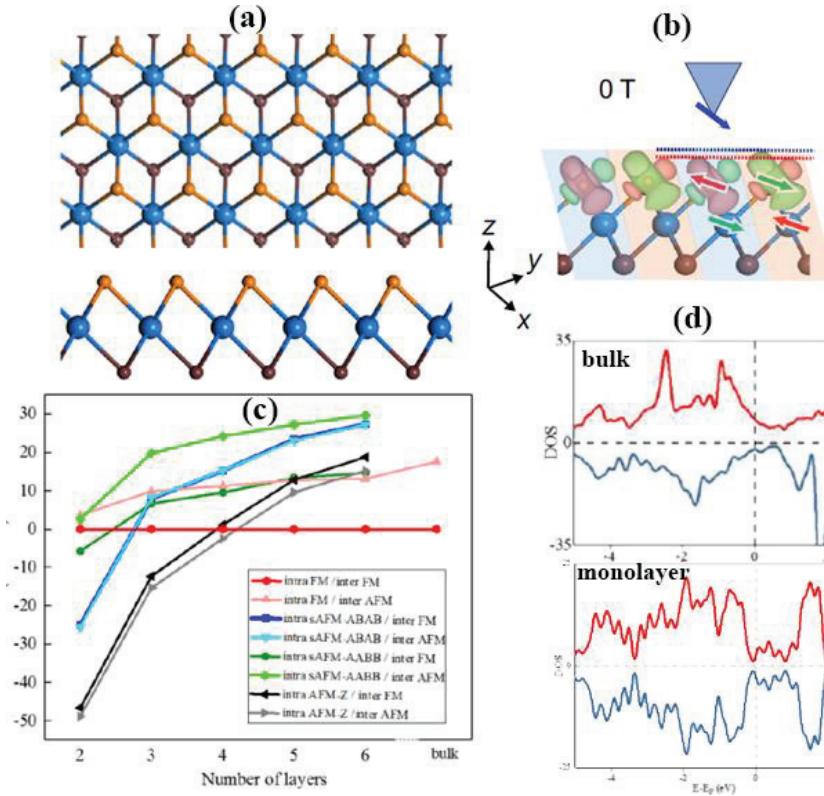


Figure 1.10 (a) Structure of 1T-CrTe₂ [44]; (b) simulated SPSTM measurement configurations at 0 T [45]; (c) The total energy of 1T-CrTe₂ with different magnetic states. (d) DOS of bulk and monolayer 1T-CrTe₂ [45].

1.5 Conclusion

In summary, multiferroic materials attract lots of attention in spintronic devices area due to its tunable magnetic/electric properties via electric/magnetic parameter. With unique *d* orbital filling and bonding with compounds, the transition metal oxides become ideal prototypical to study the intrinsic properties of multiferroics. As the first experimental confirmed single-phase multiferroic material, Cr₂O₃ has been widely researched last 30 years. However, due to its Mott insulator characteristic, there are rarely research focused on its band structure directly. The

physical properties of Cr_2O_3 films with FM edge states may also distinct from that of bulk especially its thickness reduces into several layers. The bulk CrTe_2 is ferromagnetic material with high $T_c \sim 310$ K. It thus makes CrTe_2 become the exfoliated ultra-thin vdW magnet with intrinsic long-range magnetic order above room temperature. However, the exact magnetic configuration of CrTe_2 thin film is controversial when its thickness down to the ultra-thin limit. The purpose of this thesis is to reveal the band structure of ultra-thin Cr_2O_3 and CrTe_2 films, with utilized the ARPES, XMCD, and DFT calculation.

Chapter 2 Experiment Details and DFT Calculation

2.1 Background

By combining the MBE fabrication method and in-situ ARPES/XMCD technique, it's become an achievable target to reveal the band structure, magnetic structure of ultra-thin Cr₂O₃ and CrTe₂ films, whereas related research is still lack. In this chapter, all the techniques and equipment that we used in experiment are summarized, including sample fabrication (MBE), structure characterization (AES, LEED, XAS) and physical properties characterization (ARPES). Besides, in order to better understanding the experimental result, the DFT calculation were also included in our work. The first-principles calculation related theories, corresponding calculation programs and tools are introduced.

2.2 Sample Fabrication and Structure Characterization

2.2.1 Molecular Beam Epitaxy (MBE)

MBE is a versatile technique for growing thin films, which is widely used in fabrication of sophisticated device structure. In MBE techniques, the vapor of compounds or species containing the constituent elements are generated by evaporation sources, then transported through vacuum reactor and finally deposited on substrate at high local temperature. The method make fabrication of complex heterostructures with large lattice mismatch possible. However, in such heterostructures, the strain energy of the deposited layers increases with its thickness. The growth

mode will transition from 2D to 3D growth mode is widely observed(**Figure 2.1**) [48]. Apart from this, growth of high strain thin films by MBE are also sensitive to the growth temperature, which will promote the epitaxial films (2D coverage) relaxing to its thermodynamic equilibrium states (island formation). The surfactant can impose the kinetic limitation on the sticking adatoms and further protect its 2D growth mode. Since the MBE method is realized in ultra-high vacuum environment, the synthesized films should be evaluated by surface sensitive methods, such as, LEED, AES and RHEED [49]. The fine fabrication process, detailed monitoring means, and UHV environment ensure that MBE is one of best methods to provide quantum wells, quantum wires, and quantum dots. The MBE method is superior in fabrication of high-quality thin films and opens a new route in devices fabrication and minimization.

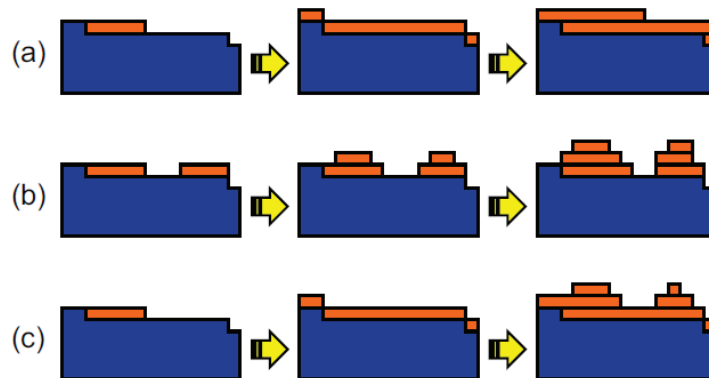


Figure 2.1 Thermodynamic thin film grow modes (a) Frank-van der Merwe(layer/2D) growth; (b) Volmer-Weber(island/3D) growth; (c) Stranski-Krastanov (2D+3D) growth mode[48].

2.2.2 Auger Electron Spectroscopy (AES)

Auger electron spectroscopy (AES) uses the electron beam to excite the inner-core electrons and eject Auger electrons from sample surface and analyzes the energy of emitted electrons to identify the elements type and content as shown in **Figure 2.2(a)**. By counting the Auger electrons which is specific to the elements, one can easily distinguish the element content (red curve in **Figure 2.2(b)**). Besides, it is convenient to show the differentiated spectrum to facilitate identifying and measuring peak positions (black curve in **Figure 2.2(b)**). The Auger electrons have relatively low kinetic energies and can be detected only from the topmost several layers of the thin films. AES is a surface-sensitive spectroscopy (0.4~10 nm), which has advantages in analysis of the ultrathin films and conducting materials. However, it also has some limitations: it has to work in UHV which is not friendly to the epoxies and organic compounds, and it is a semi-quantitative analysis which is difficult to standardization of the composition of material surface[50]. The AES provides quantitative elemental and chemical state information from surfaces of solid materials.

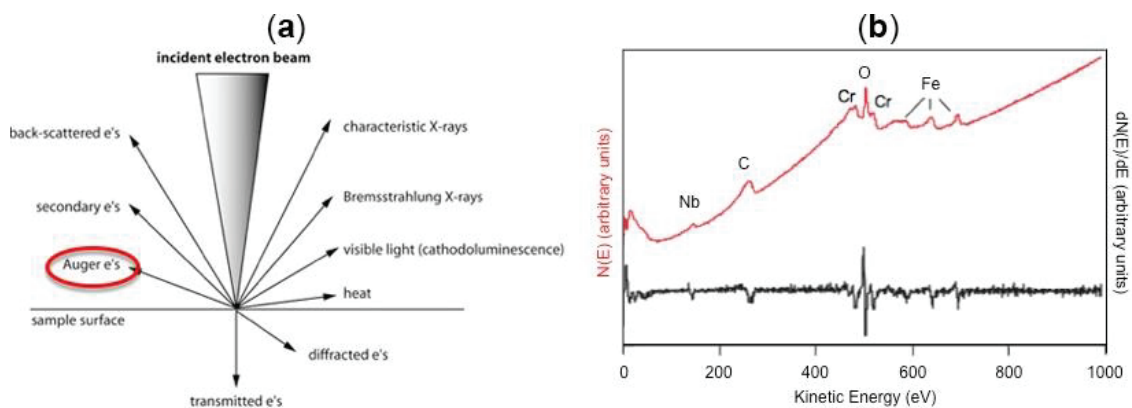


Figure 2.2 (a) Electron-sample interactions; (b) AES spectrum (red) and differentiated spectrum (black) [50].

2.2.3 Low-Energy Electron Diffraction (LEED)

Low-energy electron diffraction (LEED) is a technique for the structural investigation of surface, which is based on the diffraction of electrons with low kinetic energy. The concept of LEED originates from the Davisson and Germer's experiments [51], they found that the angular intensity distribution of the scattered electrons was in agreement with the concept of diffraction of wave-like electrons. The electrons generated by a thermionic electron gun, accelerated to sample surface and been scattered to the backscreen and recorded (**Figure 2.3(a)**) [52]. Due to the use of low-energy electrons, LEED is surface sensitive and can only be used in UHV environment to avoid the contamination, the inelastic mean-free-path (IMFP) as a function of the kinetic electron energy is shown in **Figure 2.3(b)**. The LEED has large scattering angles and sensitive to the surface structure. The qualitative analysis of the surface structure by LEED (lattice spacing, periodicity, symmetry, et al) can be deduced based on the relationship of crystal geometry and the diffraction pattern. For a more quantitative analysis, the diffraction spot profile and the electron energy dependence of spot intensity (I-V curves) can be employed to model a crystal structure near surface region.

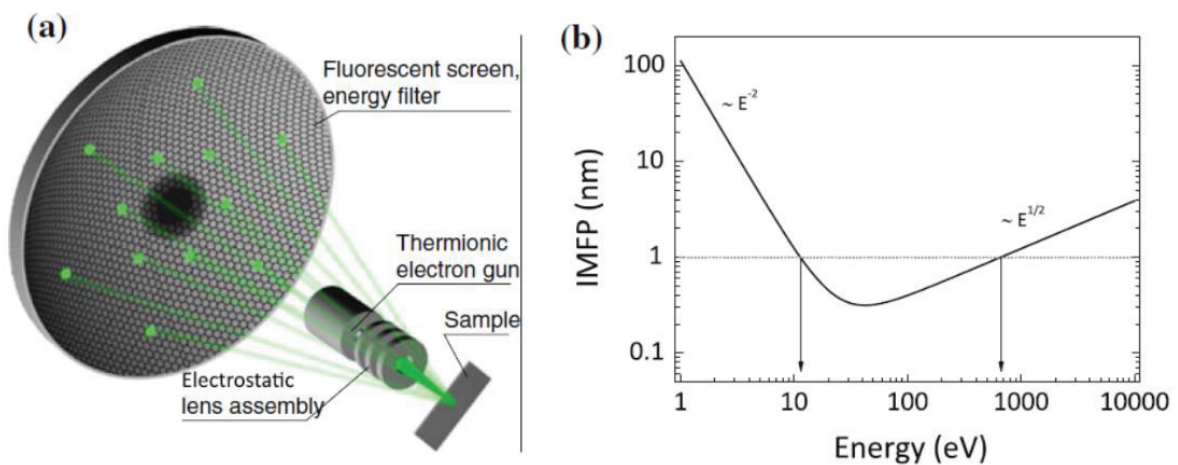


Figure 2.3 (a) Schematic of LEED principles; (b) a plot of the inelastic mean-free-path (IMFP) as a function of the kinetic electron energy[52].

2.2.4 X-Ray Absorption Spectroscopy (XAS)

X-ray absorption spectroscopy (XAS) is based on optical absorption corresponding to inner shell excitation, where the electron transits from core electronic states to the unoccupied states above the E_F . In the case of any sample exposed to the tunable X-ray beams, the absorption of X-rays shows a sudden increase in absorption at specific X-ray photon energies, which is specific to the absorbing element. The sharp increases in absorption are called absorption edge, and photon energy for the absorption edge jump coincides with required energy to excite a core electron into the lowest unoccupied molecular orbital (LUMO) or the continuum to produce a photoelectron. The absorption features contain many valuable electronic and structural information, such as bound valence states or quasibound states, core excitons in ionic crystals, unoccupied local electronic states in metals and insulators [53]. As shown in **Figure 2.4(a)**, the X-ray absorption decrease with increasing energy, the sharp rise at discrete energies is the absorption edges, and corresponding originates core level of orbitals are represented in **Figure 2.4(b)**.

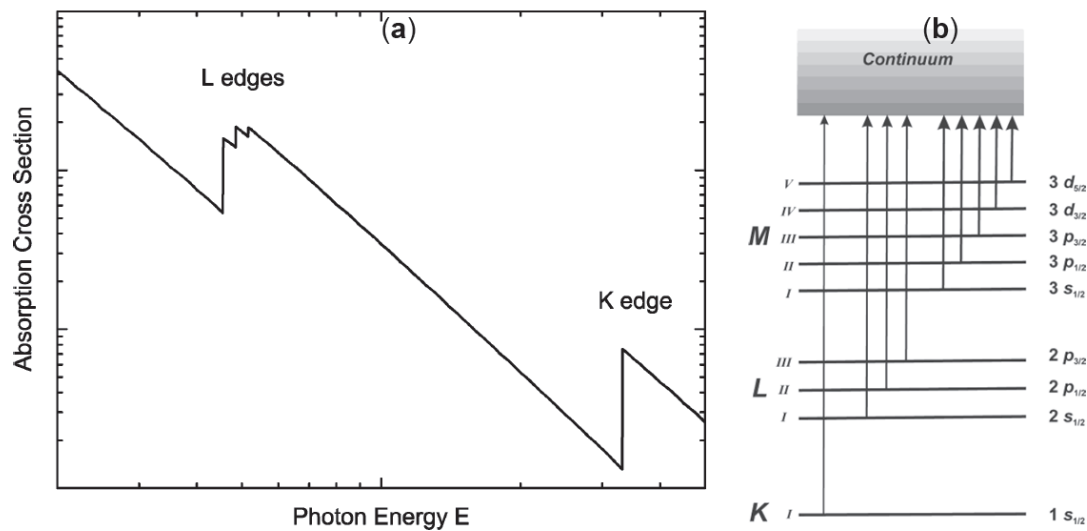


Figure 2.4 (a) Variation of the XAS of an atom as a function of the photon energy. (b) Transitions resulting from the absorption of X-rays [53].

2.3 Angle-Resolved Photoemission Spectroscopy (ARPES)

2.3.1 Photoelectric Effect

The photoelectric effect was first observed by Hertz [54] in which the light strike the surface of some metals can cause a detectable current originated from the photoinduced electron emission (**Figure 2.5**). It's worth noting that no matter how bright the light is, electrons can be ejected only if the energy of the light is higher than the threshold energy depending on metal (or if the case of sufficiently shorter wavelength). And the current increases as the intensity of the light but does not depend on the wavelength. The phenomenon is later explained as a manifestation of the quantum nature of light by Einstein [55]. He concluded the light consists of quantized or

particle-like photons with quantum of energy, and the energy can transfer to electron through collision. For the excellent work, he was honored with Nobel prize in 1921.

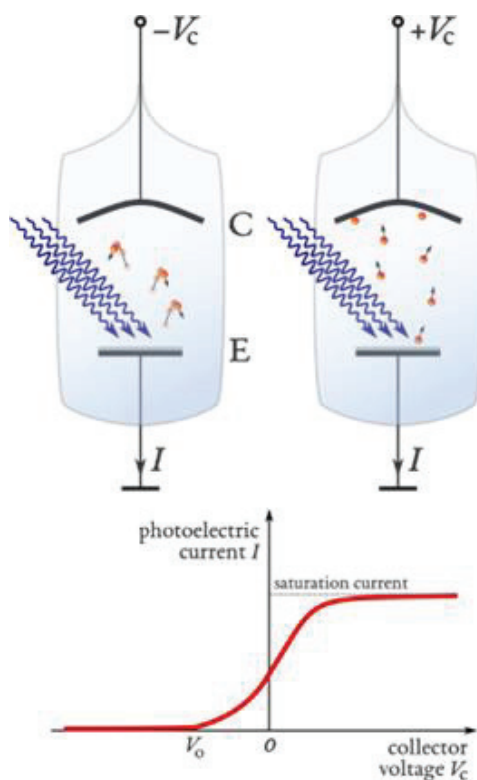


Figure 2.5 Schematic of experiment to demonstrate the photoelectric effect [56].

2.3.2 Introduction of Electron Spectroscopy

Thanks to the development of routine methods to obtain ultra-high vacuum (UHV) conditions, the electron-spectroscopic techniques, especially ARPES technique have grown significantly since about 1970 [57]. The electron escape depth is only of several Å as labeled in **Figure 2.6**, which shows a strong decrease with increasing the electron energy up to 100 eV, which

is characteristic for scattering lengths determined by electron-electron interaction[58]. Taking Au as an example (curve 3 in **Figure 2.6**), a typical metal used for calibration of the Fermi energy in ARPES experiment, shows a similar result of escape depth less than several nanometers despite of the kinetic energy varies from ultraviolet region (5~100 eV) to X-ray region (1000 eV). The probe range of photoemission spectroscopy is therefore limited to the several atomic layers of topmost sample. Considering the adsorption situation, under an exposure of 2.5 Langmuirs ($1\text{L} = 10^{-6}$ Torr·s) it takes several minutes to achieve coverage of 1 monolayer molecule on a surface. Thus, in order to get spectra from clean surface, the UHV level better than 10^{-10} torr is recognized as the precondition for studying solid surfaces.

If one focus on the bulk properties of solids, atomically clean and smooth surfaces are mandatory, or who interests in the surface states requires UHV condition to prevent interference from adsorbed contaminations. There are several advantages in electrons probe for surface spectroscopy, as compared with photon atom or ion[57], (1) easily focused, tunable, detect and account; (2) using electrostatic fields it is easy to analyze the kinetic energy and the emission angle of an electron further determining the momentum; (3) escape depth is only a few Å which are very useful in surface physics. Some disadvantages of working with electrons should also be specify explicitly, (1) UHV condition is required; (2) and atomic clean smooth surface is mandatory, experimental normally using in-situ fabricated sample or cleaving the sample in-situ to reduce such problems; (3) the limit escape depth of electrons sometimes make it difficult to distinguish between surface and bulk properties of sample, which can be partially solved using tunable light source; (4) PE spectra of semiconductors or insulators may be difficult to be observed clearly, because the energy reference points are not well defined in experimental spectra and the charge accumulation effect, where the measurement at higher temperature will weaken charging effect

but the resolution usually worse at higher temperature due to the atomic vibration and phase transition occurs in some cases.

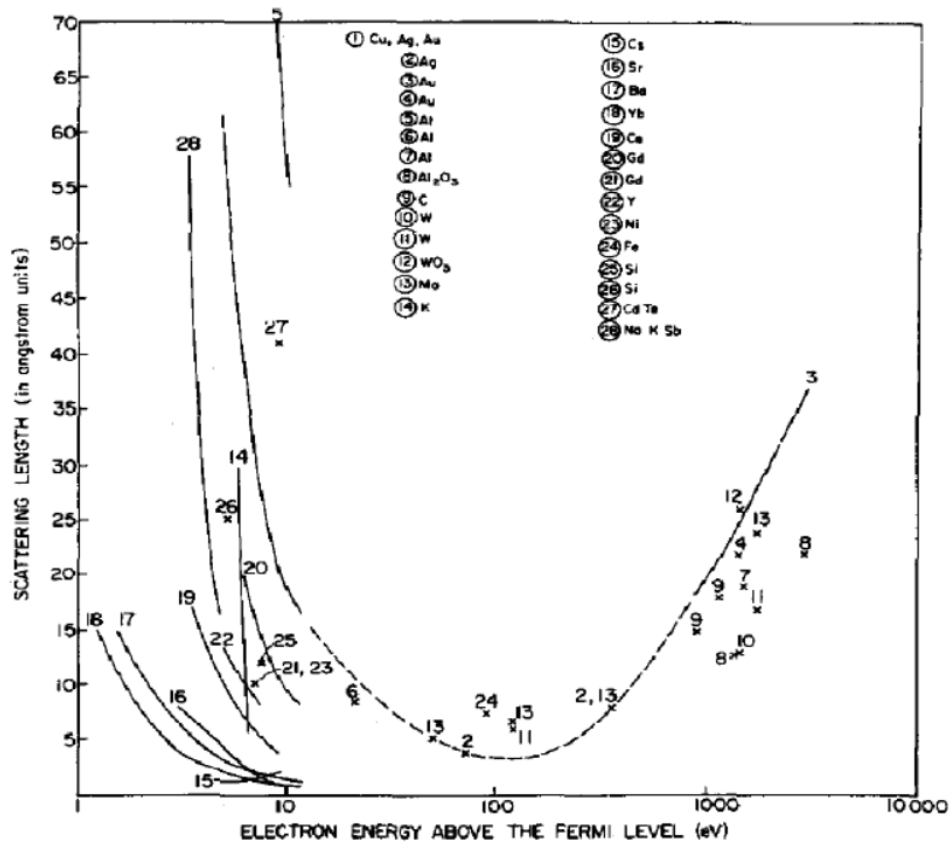


Figure 2.6 Electron escape depth in Å as a function of their kinetic energy for various materials.[58]

2.3.3 Basic Principles of ARPES

Angle-resolved photoemission spectroscopy (ARPES) is one of the most popular techniques in condensed physics for its direct detection the valance electronic structure of solids.

In the modern photoemission experiment, as shown in **Figure 2.7(a)**, when a light impinges on the sample surface, instantly the electrons will be excited and escape into vacuum if the absorbed photons is greater than the work function of material. Due to the complexity of the photoemission process in solids the quantitative analysis of the experimental data is often performed under independent-particle picture and of sudden approximation [59]. Normally, for the photoemission process, the initial (N electrons) must overlap with final states (N-1 electron) finitely and obey appropriate boundary conditions at surface of solids:

$$E_f^N - E_i^N = h\nu \quad 2-1$$

$$\vec{k}_f^N - \vec{k}_i^N = \vec{k}_{h\nu} \quad 2-2$$

where the indexes i and f refer to initial and final state and the $\vec{k}_{h\nu}$ is the momentum of incoming photon.

These photo-emitted electrons, known as photoelectrons, can be counted and analyzed with respect to their kinetic energy (E_{kin}) and momentum (\vec{p}) in an electronic analyzer [57]. The binding energy (E_B) of electrons can be determined by following equation:

$$E_{kin} = h\nu - \Phi - |E_B| \quad 2-3$$

where $h\nu$ is the photon energy, Φ is the work function of material, the minimum energy required for an electron at E_F to escape to the vacuum level (E_{vac}) The momentum p can be expressed by

$$E_{kin} = \frac{\vec{p}^2}{2m} \quad 2-4$$

$$\vec{p} = \hbar\vec{k} = \sqrt{2mE_{kin}} \quad 2-5$$

Here, m represents the mass of electrons, and \vec{k} designates the wave vector of Bloch states in a crystal. The single-electron energies E and their wave vectors \vec{k} relation $E(\vec{k})$ is called the band dispersion. The direction of \vec{k} is obtained from polar (θ) and azimuth angles (φ) of electrons leave the surface, and the vector component can be resolved into parallel and perpendicular components to the sample surface. The energy and momentum \vec{p} (wave vector \vec{k}) of electrons inside sample are directly connected to those of the photoexcited electrons inside crystal, and consequently related to those of the photoelectrons outside the crystal in the vacuum [60]. Within the noninteracting electron picture, and by taking advantage of total energy and momentum conservation[61], energy and wave vector photoelectrons parallel to the sample \vec{k}_{\parallel} is conserved [59]:

$$\vec{p}_{\parallel} = \hbar\vec{k}_{\parallel} = \sqrt{2mE_{kin}} (\sin\theta \cos\varphi \cdot \vec{k}_x + \sin\theta \sin\varphi \cdot \vec{k}_y) \quad 2-6$$

The momentum perpendicular to surface \vec{k}_{\perp} is not conserved because the translational symmetry breaks in solid surface. The determination of \vec{k}_{\perp} need a priori assumption of electron final states in the photoemission process as nearly-free electron description:

$$E_f(\vec{k}) = \frac{\hbar^2 \vec{k}^2}{2m} - |E_0| = \frac{\hbar^2 (\vec{k}_{\parallel}^2 + \vec{k}_{\perp}^2)}{2m} - |E_0| \quad 2-7$$

$$\vec{k}_{\perp} = \frac{1}{\hbar} \sqrt{2m(E_{kin} \cos^2\theta + V_0)} \quad 2-8$$

the inner potential $V_0 = |E_0| + \Phi$, corresponds to the energy of the bottom of the valence band referenced to vacuum level. The V_0 can be obtained by varying the incident photon energy (\vec{k}_z

dependent measurement) and fitting experimental periodicity along surface normal direction. The measurement therefore to be an effective way to probe the 3D Brillouin zone, which is crucial for studying topological materials [60].

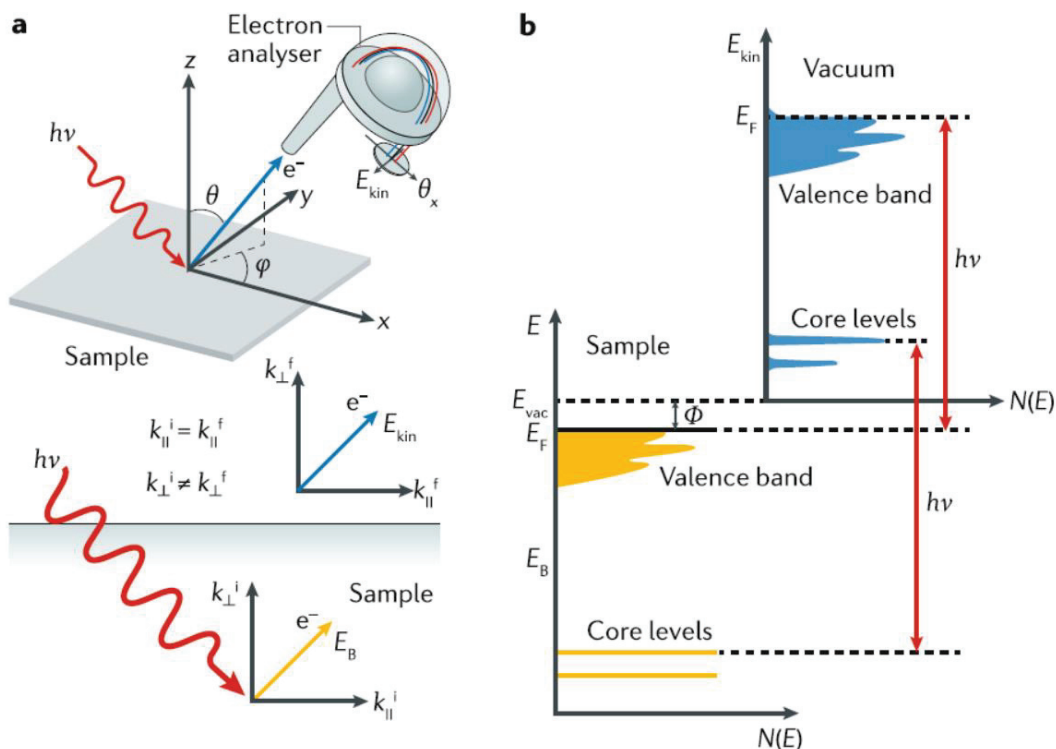


Figure 2.7 (a) Sketch and basic principles of ARPES experiment. (b) Relation between the energy levels in a solid and the electron energy distribution produced by photons of energy $h\omega$. [60]

2.3.4 Three Step Model

In one-electron theory, the transition probability w_{fi} of photoemission process for the N -electron system from initial Ψ_i^N to final Ψ_f^N states, can be obtained by **Fermi's Golden Rule**[62]:

$$w_{fi} = \frac{2\pi}{\hbar} \left| \langle \Psi_f^N | H_{\text{int}} | \Psi_i^N \rangle \right|^2 \delta(E_f^N - E_i^N - h\nu) \quad 2-9$$

where $E_i^N = E_i^{N-1} - E_B^k$ and are the initial-, final-state and binding energies of the N-particle system. The interaction with photon is treated as a perturbation given by

$$H_{\text{int}} = -\frac{e}{2mc} (\vec{A} \cdot \vec{p} + \vec{p} \cdot \vec{A}) = -\frac{e}{mc} \vec{A} \cdot \vec{p} \quad 2-10$$

where \vec{p} is the electronic momentum operator and \vec{A} is the exciting electromagnetic vector potential.

Within the three-step model the optical excitation process, the electron transport through solid and the escape across the surface are treated separately. By breaking up photoemission process into three steps, the model successfully interpretation the PE experiment. Within the approach, the photoemission process is subdivided into steps as shown in **Figure 2.8**:

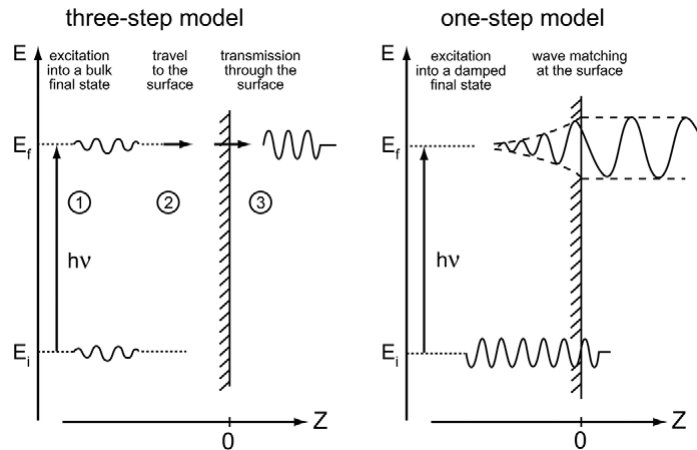


Figure 2.8 The three-step(left) and one-step(model) description of photoemission process.[59]

Step 1: optical excitation of electron in the bulk

Neglecting the momentum of photon, the optical excitation is a direct transition and keeping the momentum conservation of the matrix element, which contains all the information about the intrinsic electronic structure of the material. The internal energy distribution of photoexcited electrons $N_{\text{int}}(E, \hbar\nu)$ is given by

$$\begin{aligned} N_{\text{int}}(E, \hbar\nu) &\propto \sum_{f,i} \left| M_{fi}^t(k_i, k_f) \right|^2 \delta(E_f(k_f) - E_i(k_i) - \hbar\nu) \times \delta(E - [E_f(k_f) - \Phi]) \\ &\propto \left| M_{fi}^1 \right|^2 \text{DOS}(E_i) \delta(E - E_f + \phi) \end{aligned} \quad 2-11$$

where the first δ function imposes energy conservation during the excitation step, and the second δ function ensures that the kinetic energy measured outside the sample equals to the energy of final state inside minus the work function[57], the $\text{DOS}(E_i)$ is the density of occupied states.

Step 2: Transport the excited electron to the surface

Electrons moving towards the surface lose energy mainly due to two inelastic scattering events, electron-electron and electron-phonon scattering. The electron-phonon scattering is characterized by relatively weak electron-energy dependence and small energy losses, typically 10~50 meV [63]. The dominant scattering mechanism that reduces the number of photoexcited electrons reaching the surface is electron-electron interaction[57]. The electron-electron scattering is strongly energy dependent and the losses are a considerable fraction of the excitation energy. Besides, the electron-electron scattering is the very short scattering length of the electrons at higher energies.

Step 3: Escape of the photoelectron into vacuum

The electrons whose kinetic energy normal to the surface is sufficient to overcome the surface potential barrier, can escape to vacuum, while the other electrons with less energy will be

totally reflected into the bulk inside(**Figure 2.9**). Thus, the escape of photoelectron into vacuum is described by a transmission probability through the surface and depends on the energy of the excited electron as well as the material work function Φ . The escape process must satisfy the condition:

$$\frac{\hbar^2}{2m} k_{\perp}^2 \geq E_v - E_0 \quad 2-12$$

where the E_v is the lowest energy of valence band. The process of electrons transmit through the surface keeps the parallel component of the wave vector conserved as illustrated above (equation

$$\bar{p}_{\parallel} = \hbar \bar{k}_{\parallel} = \sqrt{2mE_{kin}} (\sin \theta \cos \varphi \cdot \bar{k}_x + \sin \theta \sin \varphi \cdot \bar{k}_y) \quad 2-6).$$

Based on equation $\bar{p}_{\parallel} = \hbar \bar{k}_{\parallel} = \sqrt{2mE_{kin}} (\sin \theta \cos \varphi \cdot \bar{k}_x + \sin \theta \sin \varphi \cdot \bar{k}_y)$ 2-6, the momentum not conservation along the parallel direction makes refraction of outgoing electrons, whose escape angle is larger than the angle of incident electrons. One can also find the detectable maximum of parallel component of internal wave vector, under the condition of $\sin \theta = 1$ which corresponding to escape angle of 90° .

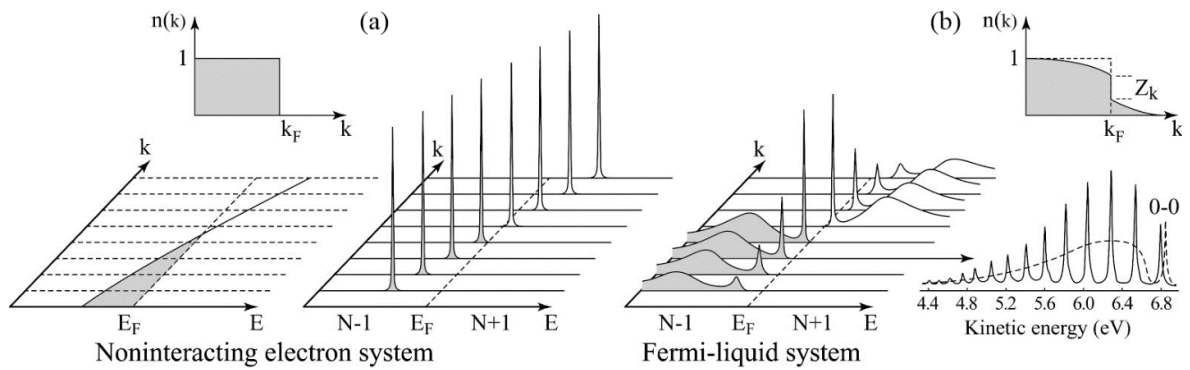


Figure 2.9 Momentum-resolved one-electron removal and addition spectra for (a) a noninteracting electron system with a single energy band dispersing across E_F and (b) for an interacting Fermi-liquid system[61].

2.3.5 Matrix Element Effect

Dipole selection rules, which can be used to determine the symmetry of the states that are involved in a direct transition, are important and have to be taken into account when analyzing experimental PE data, especially in cases of complex spectra or if polarized radiation is employed[57]. The matrix element term $I_0(\vec{k}, \nu, \vec{A}) \propto |M_{f,i}^{\vec{k}}|^2$ is highly responsible for the dependence of the photoemission data on photon energy and experimental geometry and may even result in complete suppression of the intensity[64]. The matrix element $M_{f,i}^{\vec{k}}$ in $\propto |M_{fi}^1|^2 \text{DOS}(E_i) \delta(E - E_f + \phi)$ 2-11 can be split up into surface region part $M_{f,i}^S$ (integration over a thickness which contains the region that deviates from the bulk) and true bulk region $M_{f,i}^B$ (correspond to the situation of the perfect crystal). In angle-resolved photoemission experiments with single crystals, the matrix elements have the form:

$$M_{f,i}^{\vec{k}} = \langle \phi_f^{\vec{k}} | \vec{A} \cdot \vec{p}_{op} | \phi_i^{\vec{k}} \rangle \quad 2-13$$

where the $\vec{p}_{op} = -i\hbar\nabla$ is the momentum operator. The $\phi_f^{\vec{k}} \propto d_n$, d_n can be the $t_{2g}(d_{xy}, d_{yz}, d_{zx})$ and e_g orbitals ($d_{x^2+y^2}$ and $d_{3z^2-r^2}$). The angular intensity distribution of emitted electrons is determined by the symmetry of d_n . In order to simplified the rule, the photoelectron detection plane is set to

the mirror plane of crystal (\mathcal{M}), and the vector potential \vec{A} can be parallel or normal to \mathcal{M} (Figure 2.10), which are referred as the parallel (p) and senkrecht (s) polarization geometries, respectively [65].

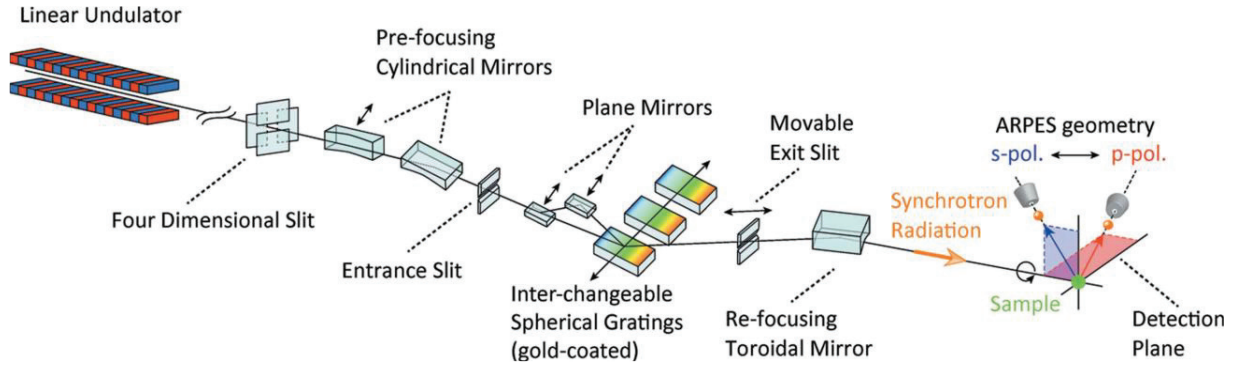


Figure 2.10 Schematic optical layout of the linear undulator beamline BL-1 at HiSOR [65].

The non-vanishing photoemission intensity is only realized if the entire matrix element $M_{f,i}^{\vec{k}}$ is a symmetric or even function with respect to the symmetry operation to \mathcal{M} . The final state $|\phi_f^{\vec{k}}\rangle$ should be even with respect to \mathcal{M} , because of the isotropic nature of final free-electron like states, the initial state $|\phi_i^{\vec{k}}\rangle$ and the dipole operator $\vec{A}\cdot\vec{p}_{op}$ have the same symmetry with respect to \mathcal{M} . The non-relativistic **dipole selection rule** can be summarized as follows,

$$\vec{A}\cdot\vec{p}_{op}:\text{even} \rightarrow |\phi_i^{\vec{k}}\rangle:\text{even} \Leftrightarrow \langle\phi_f^{\vec{k}}|\vec{A}\cdot\vec{p}_{op}|\phi_i^{\vec{k}}\rangle:\langle+|+|+\rangle$$

$$\vec{A}\cdot\vec{p}_{op}:\text{odd} \rightarrow |\phi_i^{\vec{k}}\rangle:\text{odd} \Leftrightarrow \langle\phi_f^{\vec{k}}|\vec{A}\cdot\vec{p}_{op}|\phi_i^{\vec{k}}\rangle:\langle+|-|- \rangle \quad 2-14$$

where $+$ ($-$) stands for the even (odd) function with respect to \mathcal{M} . The symmetry of the dipole operator $\vec{A} \cdot \vec{p}_{op}$ depends on the polarization direction of the vector potential \vec{A} . A measurement geometry with parallel (perpendicular) \vec{A} to \mathcal{M} , will induce an even (odd) symmetrized $\vec{A} \cdot \vec{p}_{op}$. Thus, the detectable initial state is limited to even (odd) symmetry with respect to \mathcal{M} in the $p(s)$ polarization geometry, indicating that even (odd) initial electronic states can be selectable observed by changing the polarization geometry.

When measuring ARPES at UPS photon energies, additional transitions are observed along with the k-conserving direction transition, which is confirmed to be related to the occupied DOS (DOS transitions). The “DOS transitions” is originated from the phonon-assisted indirect transitions, and related to the damping of the electron final state. The indirect transitions lead to emission via excitation into evanescent states in gaps and are called surface emission (gap emission), due to it localized near surface. It’s impossible to make a clear distinction between damped band states and evanescent gap states because both of them lead to a localization of the state near the surface and uncertainty \vec{k}_{\perp} [57].

2.3.6 Rotatable High-Resolution ARPES Station in HiSOR

In order to systematically utilize the dipole selection rule to reduce the number of valence bands according to their symmetry, BL1 of Hiroshima University Synchrotron Radiation Center (HiSOR) installed the rotatable ARPES system [66]. The electron-beam energy of HiSOR is 700MeV, and the critical wavelength is 1.42 nm. A 41-period linear undulator is installed at one of the straight sections of the ring. The beamline consists of four-dimensional slits(4DS), a water-cooled cylindrical mirror for horizontal focusing (M0), a cylindrical mirror for vertical focusing

(M1), an entrance slit (S1), spherical gratings (GR), a movable exit slit (S2), and a refocusing toroidal mirror (MF). Three changeable gold-coated spherical gratings G1, G2, and G3 cover the photon with photon energy ranges 26-350 eV with a photon flux of $>1 \times 10^{11}$ photons s^{-1} , and the electric field vector is parallel to the horizontal plane. The photoelectron detection analyzer system can be rotated from *p*-polarization to *s*-polarization which is perpendicular to the undulator light path, as plotted in **Figure 2.11**. In order to get better momentum resolution, it's better to select a lower incident photon energy such as 26~105 eV. In this energy range, the signals mainly come from the topmost several layers. By plotting energy dependent measurement, one can clearly distinguish the surface states of the materials.

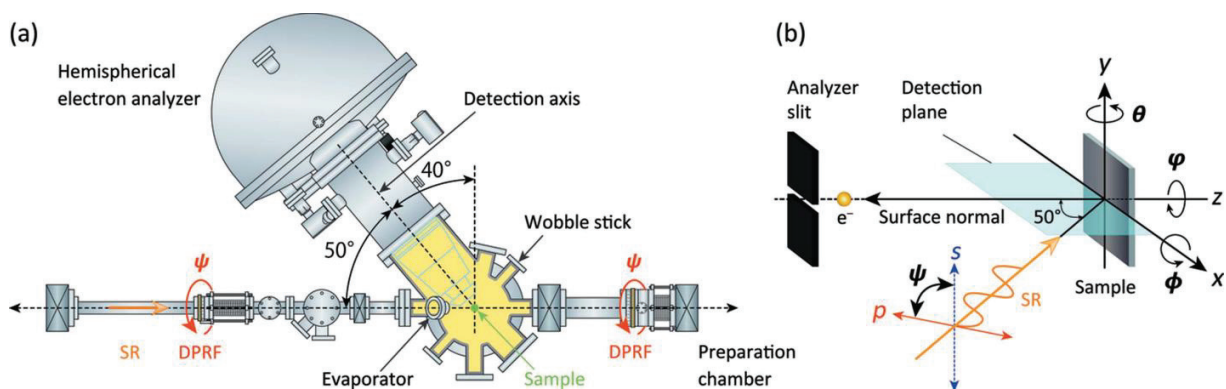


Figure 2.11 (a) Details of rotatable ARPES system in the *p*-polarization geometry. (b) Schematic of the ARPES geometry.[65]

The rotational angle of the hemispherical electron analyzer (VG-SCIEN TA, R4000) can be changed by a computer-controlled stepping motor allowing arbitrary linear polarization angle from 0 to 90° with maintaining the ultrahigh vacuum (10^{-9} Pa range) in the measurement chamber.

The analyzer and other vacuum components were fixed to a specially developed rotation frame (Aino Sangyo Co.) as shown in **Figure 2.12**. The 3-dimensional rotation orientation of sample is defined as polar(θ), tilt (ϕ), and azimuthal (φ), which corresponding to y , x , and z axes respectively. A six-axis (x , y , z with θ , ϕ and φ) manipulator is equipped with a liquid helium cooling system which can go down to 15 K. The system is designed to provide azimuth maps of the Fermi surfaces (FSs).

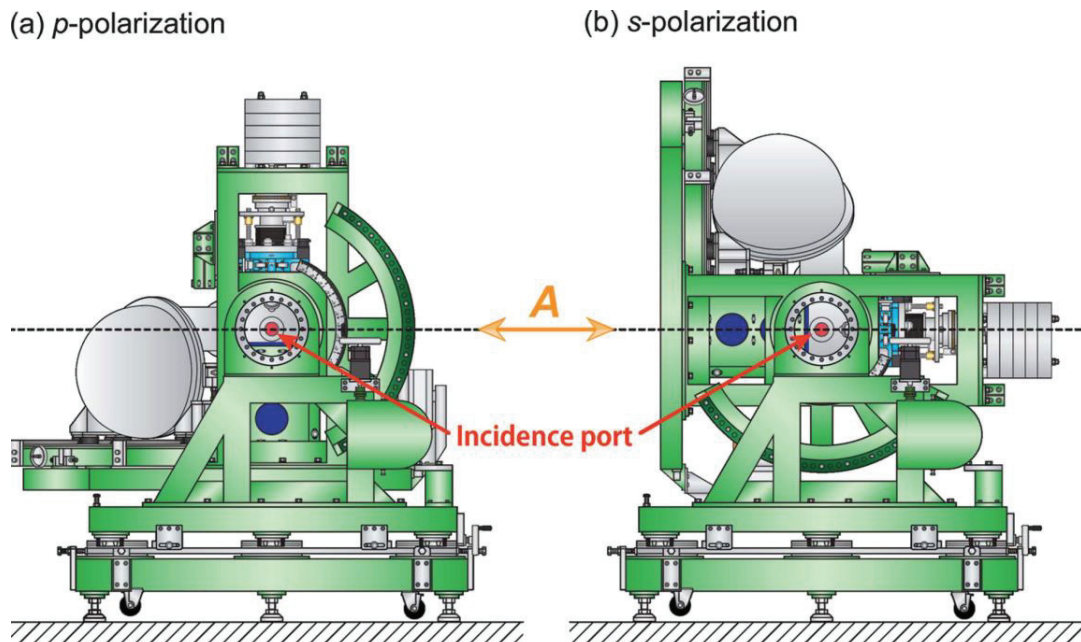


Figure 2.12 schematic side view of the rotatable ARPES system in (a) p -polarization geometry, (b) s -polarization.[65]

The ARPES system also equipped an independent in-situ fabrication and characterization chamber, as shown in **Figure 2.13**. The preparation chamber is equipped with a four-axis(x , y , z

with θ) preparations manipulator with sample holder heating stage for direct current or electron-bombardment heating. One can easily get a clean and flat surface for thin-films with below instruments, i.e., electron beam evaporators for in-situ deposition and the low-energy electron diffraction (LEED), Auger electron spectroscopy (AES), reflection high-energy diffraction (RHEED) for characterization and ion gun for cleaning the sample surface and thermocouple for detecting the temperature. Sample can be transferred between preparation chamber and measurement chamber with the help of the transfer rod and two-axis translator.

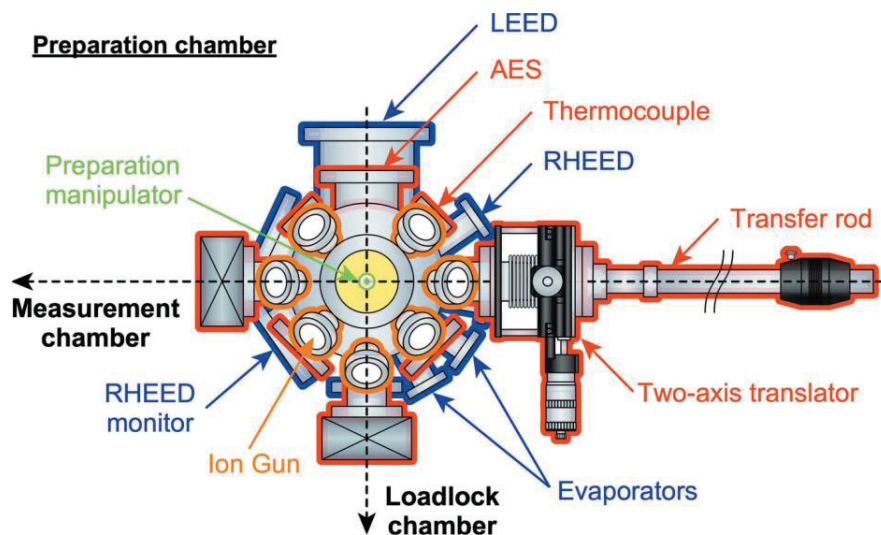


Figure 2.13 Schematic of preparation chamber.[65]

2.4 First-Principal Calculations

The determination of a many electrons problem (the band structure information) from ARPES is not always a trivial matter. There are many factors can impact the ARPES data, such as model of photon emission, matrix elements effect, experimental resolution, sample quality and

electron escape depth and so on. One of the most simplicity methods to overcome this problem is using first-principles calculation as a good complementary method to ARPES.

Over the past decades, first-principles calculation develops very rapidly and plays an important role in bridging the fundamental theory and the experimental phenomena. Band theory is seminal success in solid materials. Assisted by prediction of the first principles calculation, topological insulators, Weyl semimetals have been widely investigated.

2.4.1 Density Functional Theory (DFT)

By solving Schrödinger equation into separate mathematical problems (Born-Oppenheimer approximation), and utilize specific XC functional, one can get a numerical solution of Kohn-Sham equations by density functional theory (DFT) methods. It becomes realistic to get the numerical solution of Schrödinger equation due to the developing of calculation method and proximate method and their successively application in DFT. The accuracy of DFT depends on several reasons, (1) the intrinsic uncertainty due to unknown XC functional, (2) limited accuracy in calculation of electronic excited states underestimation of bandgaps in semiconductor/insulator and (3) strongly correlated systems with empirical parameters.[67]

The description of electron system in single crystal is complicated, even for the time-independent case, where multiple electrons affect each other and move in the electric field arisen from a set of nuclei. In that case, a more complete description of the Schrödinger equation is

$$\left[\frac{\hbar^2}{2m} \sum_{i=1}^N \nabla_i^2 + \sum_{i=1}^N V(\vec{r}_i) + \sum_{i=1}^N \sum_{j \leq i} U(\vec{r}_i, \vec{r}_j) \right] \Psi = E\Psi \quad 2-15$$

Here, m is the electron mass. The three terms in brackets in this equation define, in order, the kinetic energy of each electron, the interaction energy between each electron and the collection of atomic nuclei, and the interaction energy between different electrons. The $\Psi = \Psi(\vec{r}_1, \dots, \vec{r}_N)$ is the electronic wave function, and E is the ground-state energy of the electrons. Although the electronic wave function can be treated more simply as the product of individual function (Hartree product): $\Psi = \Psi_1(\vec{r})\Psi_2(\vec{r}), \dots, \Psi_N(\vec{r})$, the dimension of solving of the Schrödinger equation for realistic materials is growing geometrically with increasing number of atoms and electrons in the unit cell (UC). The situation is more complicated when the electron-electron interaction and the electron spin are added into consideration. The density of electrons at a particular position in space $n(\vec{r})$ can be written in terms of the individual electron wave functions:

$$n(\vec{r}) = 2 \sum_i \Psi_i^*(\vec{r})\Psi_i(\vec{r}) \quad 2-16$$

The term is the probability of the electrons in wave function $\Psi_i(\vec{r})$ and at a particular set of coordinates, the factor of 2 describes the electrons spin and the Pauli exclusion principle states in which each electron can be occupied by two separate electrons with two opposite spins. The $n(\vec{r})$ contains great amount of the information, which is a function of $3N$ coordinates.

Hohenberg-Kohn theorem and Kohn-Sham equations

Apart from written the equation into the sum of individual electron wave, another effective way to simplify the Schrödinger equation is by finding its ground-states, including the energy and

wave function of the ground state. By this way, solving the Schrödinger equation change from the issue with 3N dimensional coordinates into with 3 dimensions. This is **Hohenberg and Kohn theorem [68]**: *The total energy of an interacting inhomogeneous electron gas in the presence of an external potential is a functional of the electron density. The electron density that minimizes the energy of the overall functional is the true electron density corresponding to the full solution of the Schrödinger equation.* Based on the theorem, the single-electron energy functional can be rewritten as: $E_v[n'(\vec{r})] > E_v[n(\vec{r})]$

$$E[\Psi_i] = E_{known}[\Psi_i] + E_{xc}[\Psi_i] \quad 2-17$$

$$E_{known}[\Psi_i] = \frac{\hbar^2}{2m} \sum \int \Psi_i^* \nabla^2 \Psi_i d^3r + \int V(\vec{r})n(\vec{r})d^3r + \frac{e^2}{2} \iint \frac{n(\vec{r})n(\vec{r}')}{|\vec{r}' - \vec{r}|} d^3\vec{r}d^3\vec{r}' + E_{ion} \quad 2-18$$

$$E[\Psi_i] = E_{known}[\Psi_i] + E_{xc}[\Psi_i]$$

where the first term E_{known} in 2-17 can be split into the four terms in

$$E_{known}[\Psi_i] = \frac{\hbar^2}{2m} \sum \int \Psi_i^* \nabla^2 \Psi_i d^3r + \int V(\vec{r})n(\vec{r})d^3r + \frac{e^2}{2} \iint \frac{n(\vec{r})n(\vec{r}')}{|\vec{r}' - \vec{r}|} d^3\vec{r}d^3\vec{r}' + E_{ion} \quad 2-18, \text{ in}$$

equation order, the electron kinetic energies, the Coulomb interactions between the electrons and the nuclei, the Coulomb interactions between pairs of electrons, and the Coulomb interactions between pairs

$$E[\Psi_i] = E_{known}[\Psi_i] + E_{xc}[\Psi_i]$$

of nuclei. The second term E_{xc} in 2-17 the is the exchange-correlation functional, which includes the other quantum mechanical effects.

The Kohn-Sham equations (K-S equation), which has the form:

$$\left[\frac{\hbar^2}{2m} \nabla^2 + V(\vec{r}) + V_H(\vec{r}) + V_{xc}(\vec{r}) \right] \Psi_i(\vec{r}) = \varepsilon_i \Psi_i(\vec{r}) \quad 2-19$$

The solution of Kohn-Sham equation are single-electron wave functions that depend on only three spatial variables, $\Psi_i(\vec{r})$. The $V_H(\vec{r})$ is called Hartree potential and can be expressed by:

$$V_H(\vec{r}) = \frac{e^2}{2} \iint \frac{n(\vec{r})n(\vec{r}')}{|\vec{r}' - \vec{r}|} d^3\vec{r} d^3\vec{r}' \quad 2-20$$

This potential describes the Coulomb repulsion between the electron and the total electron density defined by all electrons. The V_{XC} can be defined as exchange and correlation contributions to the single-electron equations:

$$V_{XC}(\vec{r}) = \frac{\delta E_{XC}(\vec{r})}{\delta n(\vec{r})} \quad 2-21$$

The V_{XC} can be think to be a “functional derivative” which is not quite identical to normal derivative. **Figure 2.14** is the flowchart of using an algorithm to achieve an approximately numerical solution[69]. The one need to define an initial trial electron density $n(\vec{r})$ and solve K-S equations using the trial electron density to find the single-particle wave functions $\Psi_i(\vec{r})$. After that, calculate electron density and mix the trial-electron density and trial-wavevectors $\Psi_i(\vec{r})$ with initial values. Comparing the difference of them until the ΔE is less than the set value E_{break} . This is the iterative method to get a solution of K-S equation that is self-consistent.

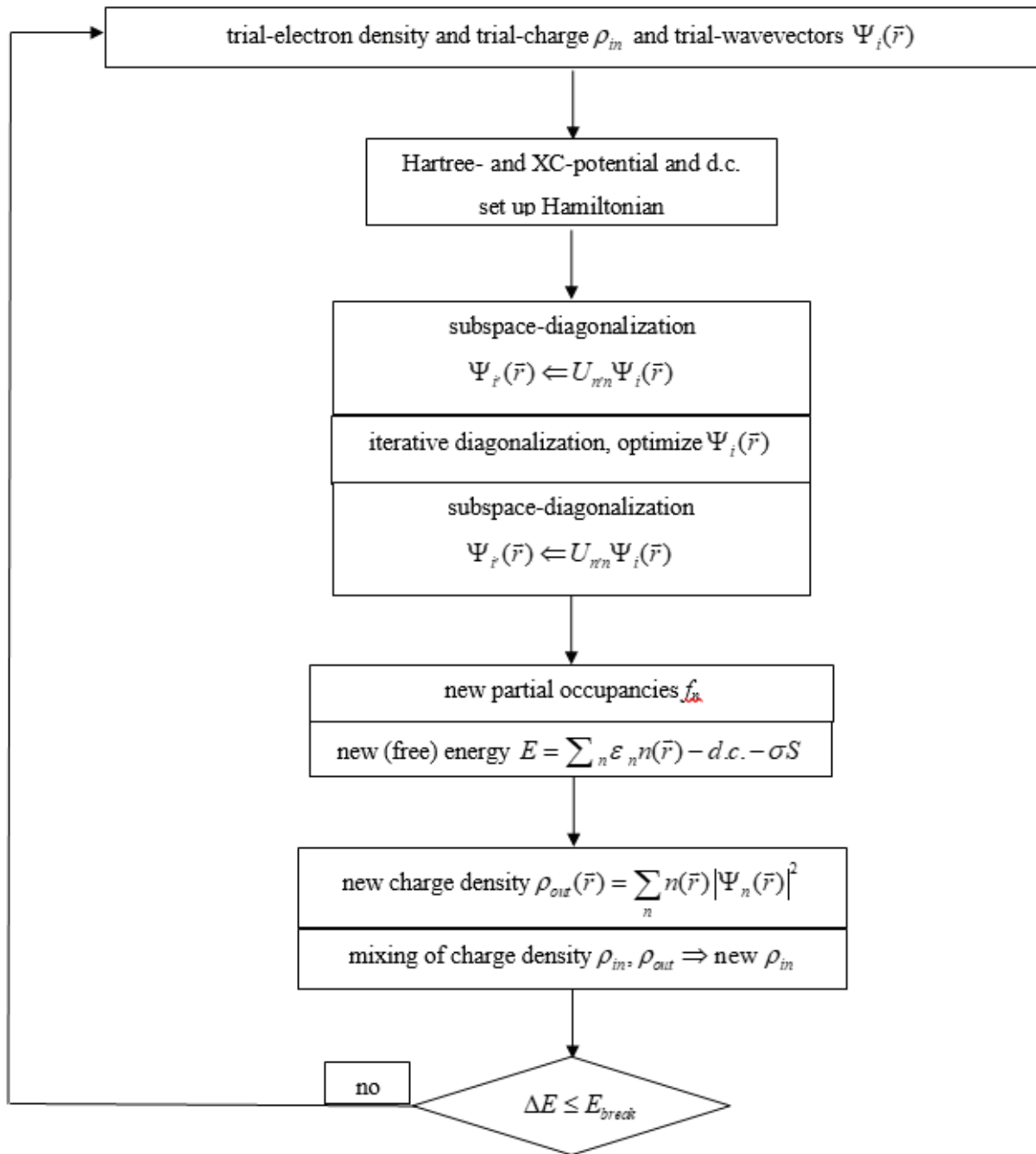


Figure 2.14 Calculation of KS-ground-state[69]

Exchange-Correlation Functional

For the uniform electron gas model, the electron density $n(\vec{r})$ is certain at all point in space. This uniform electron gas provides a practical way to use the KS equations. The exchange-correlation potential has local dependence on the density at each position, and can be written as:

$$V_{XC}(\vec{r}) = V_{XC}^{\text{electrongas}}[n(\vec{r})] \quad 2-22$$

This approximation uses the local density to define the approximate exchange-correlation functional, and is named to be *Local Density Approximation* (LDA). The methods can be extended to the spin-polarized regime which is called *Local Spin Density Approximation* (LSDA).

In most system, the electron density is typically rather far from spatially uniform, so there is good reason to believe that the LDA has limitations. The best well-known alternative correction functional for LDA exchange-correlation functional is called *Generalized Gradient Approximation* (GGA), in which depend on both the density and the gradient of the density. The electron density of GGA functional depend not only on the local value of the density, but on the extent to which the density is locally changing[70]. Most gradient corrected functionals are constructed with the correction being a term added to the LDA functional:

$$\varepsilon_{x/c}^{GGA}[\rho(\vec{r})] = \varepsilon_{x/c}^{LSD}[\rho(\vec{r})] + \Delta\varepsilon_x \left[\frac{|\nabla\rho(\vec{r})|}{\rho^{4/3}(\vec{r})} \right] \quad 2-23$$

A plenty of alternative GGA exchange functionals have been developed based on different rational function expansions of the reduced gradient, i.e., Perdew-Wang 91(91), Perdew-Burke-Ernzerhof (PBE), revised Perdew- Burke-Ernzerhof (RP), Perdew- Burke-Ernzerhof revised for solids (PBEsol). By taking second derivative of density i.e., the Laplacian, into consideration, the meta-GGA functionals have been developed. This method improved the performance of GGA but still

has challenging in its numerical stability. In this way, a hierarchy of functionals can be constructed gradually, description the solid accurately and include more and more detailed physical information.

2.4.2 Wave-Function-Based Methods

In order to representing the wave function or electron density of an isolated atom, one can assume that a series of functionals who can rapidly approach zero for different value of x . By Combined a series of such spatially localized functions with different spatial extents, symmetries and so on, to define a final function, one could describe a collection with multiple atoms. This type of function is helpful to describe periodic bulk defect-free materials and semi-infinite materials. The general method is using periodic functions to describe the *wave functions* or *electron densities* (DFT calculation). Normally, the wave-function-based methods hold a crucial advantage over electron densities methods in precisely description the Schrödinger equation. However, the wave-based methods consume much more computer time than electron densities methods. The wave function of N electron system should satisfy several mathematical properties, i.e., the Pauli exclusion principle.

2.4.3 Hartree-Fock Method

The Hamiltonian for a N electrons systems in which the electrons have no effect on each other, can be written as

$$H = \sum_{i=1}^N h_i \quad 2-24$$

where h_i describes the kinetic and potential energy of electron i . The solutions would satisfy $h\chi = E\chi$, whose eigenfunctions defined by this equation are called spin orbitals. The eigenfunctions of H are products of one-electron spin orbitals:

$$\psi(x_1, \dots, x_N) = \chi_{j_1}(x_1)\chi_{j_2}(x_2)\cdots\chi_{j_N}(x_N) \quad 2-25$$

The Slater determinant gives a better approximation for the N -electron system, which should satisfy the antisymmetry principle. As the determinant of a matrix of single-electron wave functions, the overall wave function can be expressed as

$$\psi' = \frac{1}{\sqrt{N!}} \begin{vmatrix} \psi_1(1)\alpha(1)\psi_1(1)\beta(1) & \cdots & \psi_N(1)\alpha(1)\psi_N(1)\beta(1) \\ \psi_1(2)\alpha(2)\psi_1(2)\beta(2) & \cdots & \psi_N(2)\alpha(2)\psi_N(2)\beta(2) \\ \vdots & \vdots & \vdots \\ \psi_1(N)\alpha(N)\psi_1(N)\beta(N) & \cdots & \psi_N(N)\alpha(N)\psi_N(N)\beta(N) \end{vmatrix} \quad 2-26$$

The coefficient of $1/\sqrt{N!}$ is a normalization factor. The equation satisfied the Pauli exclusion principle, and can be used for solving the Schrödinger equation including exchange. With a basis set in which the individual spin orbitals are expanded, the equations that the spin orbitals must satisfy, and a prescription for forming the final wave function once the spin orbital, one can perform an Hartree–Fock(HF) calculation. The solving of HF calculation is an iterative procedure similar to the solving the KS equations within a DFT calculation as shown in **Figure 2.14**.

2.4.4 Drawback of First Principles Calculation

Practical DFT calculations are not exact solutions of Schrödinger equation because the function applied in Hohenberg-Kohn theorem is unknown. Thus, the intrinsic uncertainty always exists between energies calculated with DFT and the real ground-states energies of Schrödinger equation. And in most cases, it's difficult to directly evaluate the uncertainty apart from carefully comparison with experimental measurements.

The DFT calculations have limited accuracy in the simulation of electronic excited states. This is because the Hohenberg-Kohn theorems are based on the ground-state energy. Besides, the most well-known inaccuracy in DFT is the underestimation of calculated band gaps in the semiconductors or insulators. The occupied states of crystalline materials are described by continuous functions named energy band. In this definition, the highest occupied energy (valence band, VB) of a metal overlap with the next unoccupied higher band (conduction band, CB) or has a not fully occupied band. The VB of semiconductor or insulator is completely filled while the CB is empty. Thereinto, materials with a large band gap are called insulators while materials with small band gap are called semiconductors. Standard GGA calculations with existing functionals have limited accuracy for band gaps. The discrepancy between calculation with experiment errors larger than 1 eV are common. The GGA+U method or using hybrid functional are effective for fixing this issue.

The DFT calculation also fails in accurate description when one need to add the van der Waals(vdW) attraction into consideration. The vdW interactions occur because of correlations that exist between temporary fluctuations in the electron density of one molecule and the energy of the electrons in another molecule responding to these fluctuations. The vdW interactions are a direct result of long-range electron correlations, a systematic method is needed to build if one need to add vdW into high-level wave-function-based methods. The accurate solution for a Schrödinger

equation with vdW also challenging in limited computational expense. The computational expense stems from solving of the mathematical problem posed by fundamental DFT theorem. The difficulty increases exponentially in computing technology as atoms number increase, which limited the DFT calculations to directly examine collections of atoms of this size. Thus, the DFT calculation must be executed based on clearly understanding of the physically relevant to real materials.

2.4.5 VASP Programs

Vienna Ab-initio Simulation Package(VASP) package is one of the most popular DFT codes using pseudopotential and a plane wave basis set. With efficient matrix diagonalization schemes, an efficient Pulay/Broyden charge density mixing, the projector-augmented wave(PAW) method, the VASP can be useful for systems with up to 4000 valence electrons[69]. VASP uses self-consistency cycle to solve KS ground state, with equipment of several diagonalization schemes (RMM-DISS, and blocked Davidson). It also includes a full featured symmetry code which can be used for determine the symmetry of arbitrary configurations and Monkhorst Pack k-point.

The general calculation will be done in a work directory and before starting a calculation, The following input files must be created in this directory:

1. The INCAR includes all of the calculation parameter, such as the calculation method, the energy/force convergence criteria, direction of force, how to move the ions, and the step of every movement and output files.

2. The POSCAR file includes all of the structure information required for calculation, i.e., atoms number, species, coordinates and spatial groups.

3. The POTCAR file can be copied from the pseudopotential library, include the information of atom mass, valence, the energy of the atomic reference configuration for which the pseudopotential was created.

4. The KPOINT file determine the k-points setting, for isolated atom or molecule, one k-point is enough. However, one has to balance the contradiction of enough k-points to describe a periodic system and the least computation expense. The number of k-points necessary for a calculation depends on the necessary precision and on the conductivity of system. Usually, metallic systems require much more k-points than semiconductors and insulators. The number of k-points also depends on the smearing method.

VASP can be used to calculate the equilibrium lattice constant, determine the equilibrium volume, the density of states (DOS) and band-structure. By taking a small trial step and performing a line minimization of the energy along the direction of the forces, then the total energy is re-evaluated. From the energy change and the initial and final forces, VASP calculates the position of the minimum. The DOS/band-structure calculation can be done by a simple static selfconsistent calculation and to use the DOSCAR or vasprun.xml to extract the information via vaspkit [71]. An accurate DOS/band-structure calculation might require very fine k-meshes. In order to increase the efficiency of DOS/band calculation, researchers often calculate the selfconsistent charge density using a few k-points. After that, read the precalculated charge files from the selfconsistent run to perform a nonselfconsistent calculation with denser k-points.

Chapter 3 DFT Calculation of Cr₂O₃/Graphene

Interface

3.1 Introduction

Cr₂O₃ is a typical Mott-insulator with a bandgap of 3.2 eV. Besides, Cr₂O₃ also a single-phase multiferroic material, which possess antiferromagnetic and magnetoelectric. The physical properties can be modulated by doping, strain, vacancies and reduce the film thickness. Some researchers found that the ultrathin Cr₂O₃ films will have a narrower bandgap. The finding prompt that the band structure of ultrathin films may different from the bulk, as well as its physical properties. But, till now, there is no direct investigation about the band structure of ultrathin Cr₂O₃ films. The reason is might because its bandgap is too large, which make it difficult to be detected in electronic spectroscopy (normally require samples are conductor). From the perspective of revealing the real electronic structure of ultrathin Cr₂O₃ films, a preliminary calculation before experiment will be much helpful. The prediction of ultrathin Cr₂O₃ films and Cr₂O₃-based heterointerface can save experimental resources and act as a guide for leading the direction of experiment.

3.2 General Calculation Parameters

All first-principle calculations were performed within the generalized gradient approximation (GGA) method using the VASP code [72, 73] and a plane wave energy cutoff of 520 eV. The exchange-correlation interaction was described by the Perdew–Burke–Ernzerh (PBE-GGA) [74].

The Hubbard U effects on the transition metals Ni and Cr are included within the DFT+ U approach, and a detailed U test for Cr_2O_3 is illustrated in **Figure 3.1**. The band gap is indeed underestimated in the calculations using GGA-PBE functional compared with other functional, such as HSE. However, with consideration of U , we find Cr_2O_3 shows a good agreement with previous calculations. We tested the U parameter for Cr_2O_3 . As seen from **Figure 3.1**, the band-gap varies with increasing the U . The band-gap of bulk Cr_2O_3 is 3.2 eV at $U=6$, which is highly agree with experimental value ~ 3.31 eV[32]. Besides, the main peak position of Cr $3d$ orbital is almost not changing with varying of U . The valance band of our calculation is also well agreed with our ARPES result. The changing of U for Ni element almost has no influence due to its metallic characteristic. We choose $U = 4.5$ for Ni element based on previous reports [75].

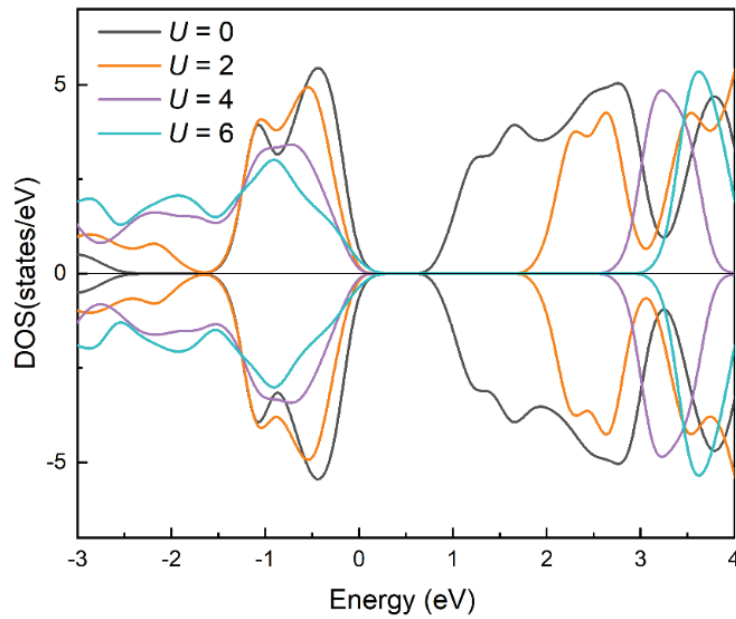


Figure 3.1 GGA+ U parameter test for Cr_2O_3 . [76]

The $U_{eff} = U - J = 6.0$ eV and $U_{eff} = 4.5$ eV are reasonable values for Ni-3d [75] and Cr-3d orbitals [77]. The DOS and band characteristics of bulk Ni and Cr₂O₃ were in all good agreement with the experimental results. The magnetic structures of Ni and Cr₂O₃ were assumed to be collinear ferromagnetic and antiferromagnetic configurations, respectively, and the magnetic moments pointed in the c direction of the heterostructure, as plotted by the green and purple arrows in **Figure 3.2**. The in-plane lattice constant of the bottom three layers of the substrate was fixed to the experimental values but relaxed along the c direction by minimizing the total energy difference to less than 10^{-6} eV, and the remaining forces to less than 2 meV/Å. A $7 \times 7 \times 7$ k -point was used for the Brillouin zone of bulk cases, whereas $5 \times 5 \times 1$ k -point was used for heterostructures [78]. The van der Waals (vdW) contribution by Grimme's semi-empirical correction was also considered in our calculations [79]. All slabs possessed 20 Å vacuum layers. Ni has a lattice parameter of $a_{Ni} = 3.55$ Å [39] and cuts along (111) plane with seven layers, thus making it an ideal substrate for the epitaxial growth of graphene ($a_{Gr} = 2.46$ Å). The Cr₂O₃ cut along the (0001) plane with the ordered stacking planes repeated in one layer of oxygen (in-plane distance $d_{O-O} = 2.86$ Å) and two close and shifted layers of AFM chromium (in-plane distance $d_{Cr-Cr} = 4.96$ Å).

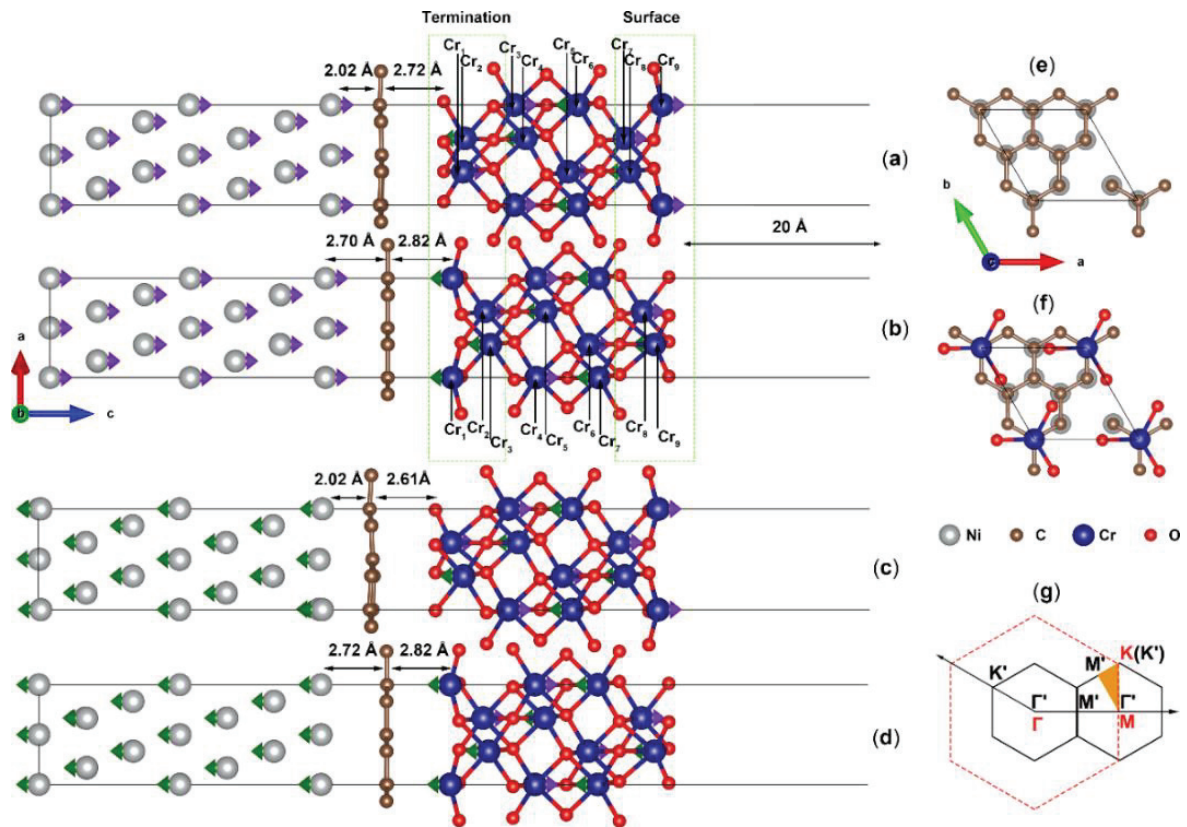


Figure 3.2 Two termination models of 1nm-Cr₂O₃/Gr/Ni(111). Models of (a) O- and (b) Cr-terminated Cr₂O₃/Gr/Ni(111) with the magnetization direction of Ni points to the surface; (c) O- and (d) Cr-terminated Cr₂O₃/Gr/Ni(111) with the magnetization direction of Ni points to the substrate. Interfacial configuration of atop model of (e) C/Ni(111) and (f) Cr₂O₃/Gr/Ni(111). (g) Brillouin zone of primitive graphene (red dash line) and folded of 2×2 supercell graphene (black line). [76]

3.3 Structure Modeling of Interfaces

The thicknesses of Cr₂O₃ in the calculation models were fixed to nine layers, which were based on 1nm-Cr₂O₃ thin films grown on the graphene-covered Ni(111) substrate in the experiment. The interfacial configuration was selected based on previous reports [80-83]. There are six symmetrical structures of Gr/Ni(111) top-hcp, top-fcc, bridge-top, bridge-hcp, hcp-fcc, and bridge-

fcc, which have similar energies [83]. The C atoms were located directly above the Ni atoms of the first (top site) and second layers (hcp site) in the top-hcp model. Despite the tiny disparity in the atomic configurations, all structures are stable around the C-Ni distance (d_{C-Ni}) of approximately 2.0–2.3 Å, which agrees well with the chemisorption results in the experiments [84]. The Dirac points are destroyed at d_{C-Ni} less than 2.3 Å because of the hybridization effect between the C and Ni valence bands. In this study, we employed the top-hcp model, which is the most stable of these models.

Takenaka *et al.* reported that the Cr₂O₃/Gr heterostructure is the most energetically stable model if Cr lies atop on C atoms. The spin structure induced by the ferromagnetic terminations of Cr₂O₃[35, 36] was included and carefully considered in the slab models. The Cr₂O₃ layer in contact with graphene and the vacuum is defined by the interface termination and surface, respectively (as shown in the green dotted frames in **Figure 3.2 (a, b)**). The final O- and Cr-terminated models are named according to the interface structure of the Cr₂O₃ slab in contact with graphene, as shown in **Figure 3.2 (a, b)**. In the final models, the interfacial Cr, C, and Ni were all placed at the atop position (**Figure 3.2 (e, f)**). The magnetization direction of Ni(111) points to the surface (purple arrows in **Figure 3.2 (a, b)**) or the inner substrate (green arrows in **Figure 3.2 (c, d)**) are both considered in our calculations.

3.3 Total Energy and Density of States

Table 3.1 lists the total energy and total energy per atom of the four models after optimization of the atomic distance. The reduction in the total energy per atom ΔE is calculated as

$$\Delta E = (E_{Gr/Ni} + E_{Cr2O3slab} - E_{Cr2O3/Gr/Ni}) / N_{atoms} , \quad 3-1$$

where $E_{\text{Gr/Ni}}$, $E_{\text{Cr}_2\text{O}_3\text{slab}}$, $E_{\text{Cr}_2\text{O}_3/\text{Gr/Ni}}$, and N_{atoms} are the total energy of the Gr/Ni, Cr₂O₃ slab, Cr₂O₃/Gr/Ni heterostructure, and number of atoms, respectively. The comparable negative values of ΔE indicate that all models can exist on the Gr/Ni(111) surface, although the Cr-terminated models are more stable than the O-terminated models. The variation of $d_{\text{C-Ni}}$ before and after flipping the magnetization direction of Ni(111) is less than 0.2 Å, as shown in **Figure 3.2(b, d)**. Meanwhile, changing the Cr₂O₃ termination from O- to Cr- leads to a larger difference, and the variation of $d_{\text{C-Ni}}$ is more than 0.68 Å as shown in **Figure 3.2(c, d)**. The magnetization direction flipping of Ni(111) had a negligible influence on $d_{\text{C-Ni}}$ and total energy. In later discussion, we will focus on the first two models in **Figure 3.2(a, b)** with the magnetization direction of Ni all pointing to the surface. The description of the magnetization direction of Ni has been omitted.

Table 3.1 Total energy of O- and Cr-terminated models with the magnetization direction of Ni points to surface/substrate

Total energy reduction (eV/atom)	Magnetization direction of Ni points to surface	Magnetization direction of Ni points to substrate
O-terminated	-0.333	-0.330
Cr-terminated	-0.347	-0.356

A common feature of the O- and Cr-terminated models after structural optimization is that the surface structures are compressed along the c direction. As can be observed from the surface part of **Figure 3.2(a, b)**, the topmost Cr layers are shifted to the nearest-neighbor O layers. The layer-to-layer distance near the surface is shortened and forms a reconstructed surface, which is

consistent with recent experimental reports [39, 85]. Lodesani *et. al* suggested that such peculiar surface can exist only if the films are ultrathin (< 1.6 nm) and in UHV environments [39].

The $d_{\text{C-Ni}}$ of Gr/Ni(111) in our calculation is 2.23 Å, which is slightly larger than $d_{\text{C-Ni}} = 2.17$ Å [82, 83] and 2.12 Å [83] in previous reports, which might be due to the van der Waals (vdW) contributions and algorithm selection. However, this does not change the unanimous conclusion that graphene is *n*-type on Ni(111). The O-terminated model has a smaller $d_{\text{C-Ni}}$ (2.01 Å) than the Cr-terminated model ($d_{\text{C-Ni}} = 2.70$ Å). The result for O-terminated Cr₂O₃/Gr/Ni(111) is more similar to the situation of oxygen intercalated into graphene/Ni(111), which has been observed in a previous ARPES study [86]. The intercalation into graphene is stable up to 500 K but completely disappears at 680 K [86]. Considering that the deintercalation temperature (680 K) is close to the substrate temperature (650 K) during deposition, both metastable O-terminated and Cr-terminated models can stably exist on the Gr/Ni(111) surface under such conditions.

3.4 Density of States

Here, we examined the DOS of the O- and Cr-terminated models. The DOS of C in freestanding graphene, Gr/Ni(111), and O/Cr-terminated Cr₂O₃/Gr/Ni(111) are shown in **Figure 3.3(a)–(d)**. Freestanding graphene is a zero-bandgap semimetal where the π and π^* states are localized at E_F and 1 eV above (**Figure 3.3(a)**). The π and π^* states in Gr/Ni(111) moved to lower energies and had more dispersive contributions than those in the freestanding type (**Figure 3.3(b)**). The shapes of π and π^* states of the O-terminated model are delocalized similar to that of Gr/Ni (**Figure 3.3(c)**). Meanwhile, the Cr-terminated model indicates localized π and π^* states similar to freestanding graphene but heavily *n*-doped (**Figure 3.3(d)**).

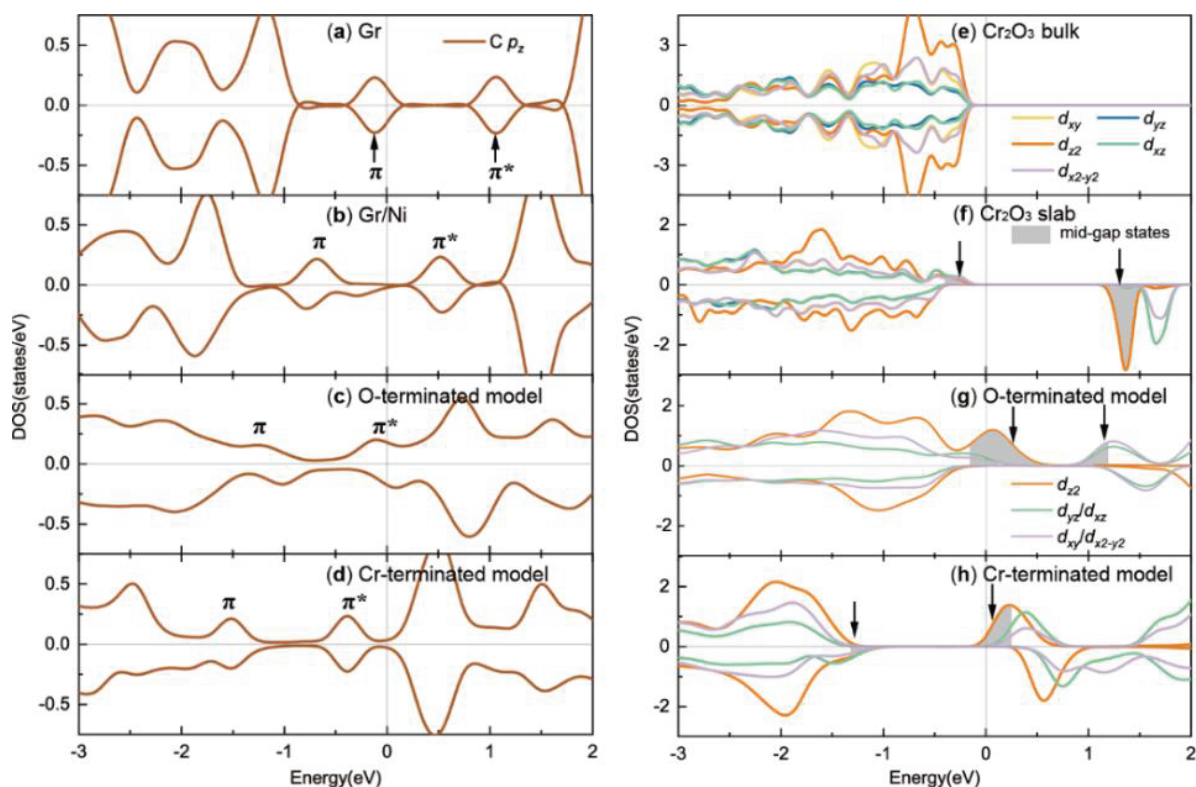


Figure 3.3 DOS of (a) freestanding 2×2 supercell graphene, (b) 2×2 graphene on Ni(111) surface, and graphene in (c) O- or (d) Cr-terminated model. DOS of (e) single crystal Cr_2O_3 , (f) 1nm- Cr_2O_3 slab, (g) O- and (h) Cr-terminated $\text{Cr}_2\text{O}_3/\text{Gr}/\text{Ni}(111)$ model. The mid-gap states of Cr are denoted by gray colors and arrows in the right panel. [76]

The element-resolved DOS of Cr in bulk Cr_2O_3 , slab Cr_2O_3 , and O- and Cr-terminated $\text{Cr}_2\text{O}_3/\text{Gr}/\text{Ni}(111)$ are plotted in **Figure 3.3(e)–(h)**. As shown in **Figure 3.3(e)**, the theoretical bandgap of bulk Cr_2O_3 (3.19 eV) agrees well with the experimental optical gap (3.31 eV) [32]. The Cr_2O_3 slab calculation exhibits mid-gap states (gray filled parts), while the insulating character remains (**Figure 3.3(f)**). Compared with the simple Cr_2O_3 slab in **Figure 3.3(f)**, E_F is increased in both the O- and Cr-terminated models owing to the charge transfer from Ni to Cr_2O_3 . Cr_2O_3 in the O-terminated model becomes a half-metal, which mainly originates from the Cr $3d_z^2$ orbital. Note that the Cr-terminated model has a narrower bandgap than that of the Cr_2O_3 slab.

Table 3.1 lists the core level energy of the bulk Ni, Cr₂O₃ slabs, and Cr- and O- models. One can deduce the band offset direction of heterostructure by comparing the difference of core states before and after heterostructure formation [87, 88]. The band offset ΔE of the heterostructure is defined by:

$$\Delta E = E_{core_bulk} - E_{core_hetero}, \quad 3-2$$

where E_{core_bulk} and E_{core_hetero} represent the energies of the core states of the bulk crystal and the heterostructures, respectively. Atoms away from the interface were selected to minimize the influence of the interface. The band of Cr₂O₃ in the O-terminated model is shifted to a higher binding energy direction; therefore, the spin-down band has a larger band offset (1.70 eV) than the spin-up band (1.20 eV). The band shifting comes from the charge transfer from one side of interface to the other side. The Cr-terminated model showed a band shift direction similar to that of the O-terminated model, spin-up (1.94 eV), and spin-down (2.59 eV).

Table 3.2 Core level energy and energy difference ΔE of Ni, bulk Cr₂O₃ and Cr₂O₃/Gr/Ni(111) heterostructure

Core level energy (eV)		Ni-1s	O-terminated Cr ₂ O ₃ -Cr 2p		Cr-terminated Cr ₂ O ₃ -Cr 2p	
Bulk (E_{core_bulk})	spin-up	-8.33	-43.52			
	spin-down	-8.47	-43.52			
Heterostructure (E_{core_hetero})		Ni-1s	p_x/p_y	p_z	p_x/p_y	p_z
	spin-up	-8.42	-44.72	-44.33	-45.46	-45.34
	spin-down	-8.48	-41.82	-40.62	-46.11	-46.04
ΔE	spin-up	-	-1.20	-	-1.94	-
	spin-down	-	1.70	-	-2.59	-

3.5 Band Structure

To better understand the band structure of the heterostructure models, we described the band folding of Cr₂O₃/Gr/Ni(111). Graphene's honeycomb lattice ($a_{\text{Gr}} = 2.46 \text{ \AA}$) matches the triangular lattice of Ni(111). The in-plane lattice of Cr₂O₃(0001) ($a = 4.97 \text{ \AA}$) is, however, twice that of graphene. Thus, the heterointerface of Cr₂O₃(0001) and Gr/Ni(111) forms a 2×2 superstructure with a lattice constant two times larger than that of graphene. The corresponding Brillouin zone length of Cr₂O₃/Gr/Ni(111) was folded to half that of Gr/Ni(111). The Dirac cone position after band folding is still located at the \bar{K}' point, whereas the $\bar{K}' \rightarrow \bar{\Gamma}'$ in the supercell represents $\bar{K}' \rightarrow \bar{M}'$ in the primitive cell, as shown in **Figure 3.2(g)**.

The corresponding band structures in the primitive graphene cell and 2×2 supercell graphene are discussed in detail. The length of the vector of 2×2 graphene is twice of that in the primitive cell, and the reciprocal-lattice vector is therefore half of that in the primitive cell. As shown in **Figure 3.4**, the red hexagons are Brillouin Zone (BZ) of primitive graphene, the black hexagons represent the BZ of the superstructure of graphene. We can get the band structure of 2×2 graphene supercell by folding the primitive cell. The $\bar{\Gamma} - \bar{K}$ direction of the primitive BZ includes $\bar{\Gamma}' - \bar{K}' - \bar{M} - \bar{K}'$ path of supercell. The path of $\bar{\Gamma} - \bar{M}$ in primitive cell corresponds to $\bar{\Gamma}' - \bar{M}' - \bar{\Gamma}'$ in the supercell. The \bar{K}' in supercell still presents the properties of primitive \bar{K} point. Due to band folding introduce more complex patterns in supercell BZ, it is difficult to compare the calculation band and ARPES band in a wide energy range intuitively (**Figure 3.5**). In the further discussion of manuscript, we will focus on the characteristic at the \bar{K}' point.

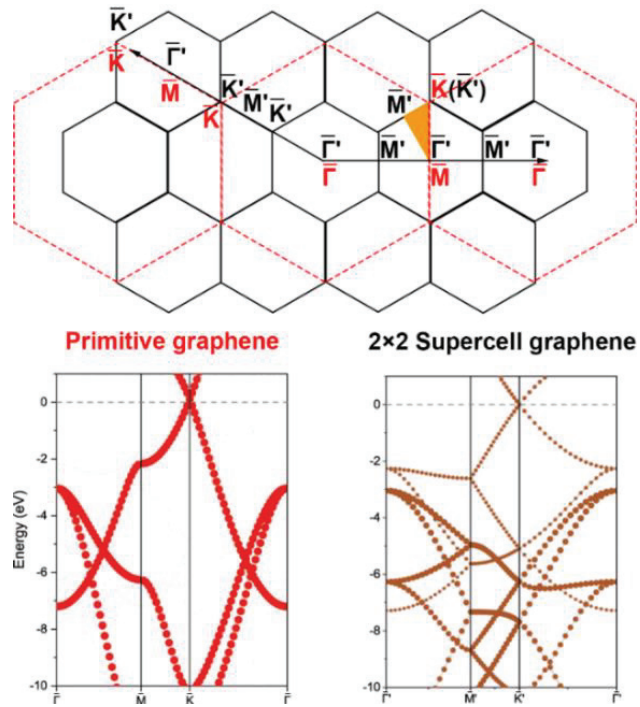


Figure 3.4 Schematic of graphene band folding, the red hypotenuse hexagons are BZ of primitive graphene, the black hexagons are BZ of supercell 2×2 graphene. The band structure of graphene before and after folding are plot by red and gray dot in lower panel. [76]

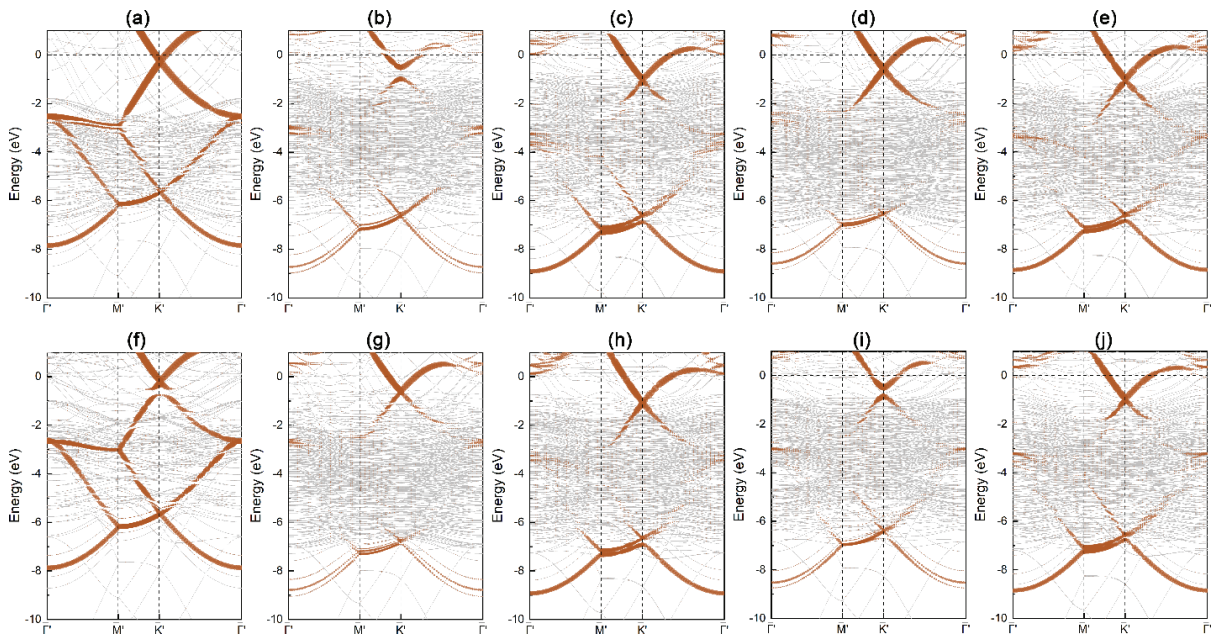


Figure 3.5 Spin-up band structures of graphene p_z orbitals (π band) of (a) C/Ni, (b) O- and (c)Cr-terminated model with magnetization points to substrate, (d) O- and (e) Cr- terminated model with magnetization direction points to substrate. (f)-(j) are corresponding spin-down band structures. [76]

The element-resolved valence band structures of the O- and Cr-terminated $\text{Cr}_2\text{O}_3/\text{Gr}/\text{Ni}(111)$ are illustrated in **Figure 3.6**. Spin-up(down) is defined with respect to the spin direction parallel (antiparallel) to Ni magnetization direction. The C and Cr bands are represented by the brown and blue circles, respectively. The C band dispersion of 2×2 freestanding graphene is shown in the left panel for reference. In **Figure 3.6(b, e)**, one can observe spontaneous charge transfer from Ni(111) to graphene, leading to n -doped graphene, which is due to the difference in the work function between graphene and Ni. The Dirac cone position of graphene is shifted to energy ~ -0.42 eV. The Dirac cone position of graphene in O-terminated $\text{Cr}_2\text{O}_3/\text{Gr}/\text{Ni}(111)$ is located at an energy of ~ -0.51 eV, which is similar to that of $\text{Gr}/\text{Ni}(111)$, as can be observed from the \bar{K}' point of **Figure 3.6(a, d)**. In addition, graphene has a bandgap in the spin-up state but recovers its linear characteristic in the spin-down states, which is distinct from the $\text{Gr}/\text{Ni}(111)$ in Figs. 4(a) and (d). The 1×1 LEED spot of $\text{Cr}_2\text{O}_3/\text{Gr}/\text{Ni}(111)$, which originated from the reconstructed ultrathin Cr_2O_3 film surface in UHV [39], is consistent with the interfacial structure.

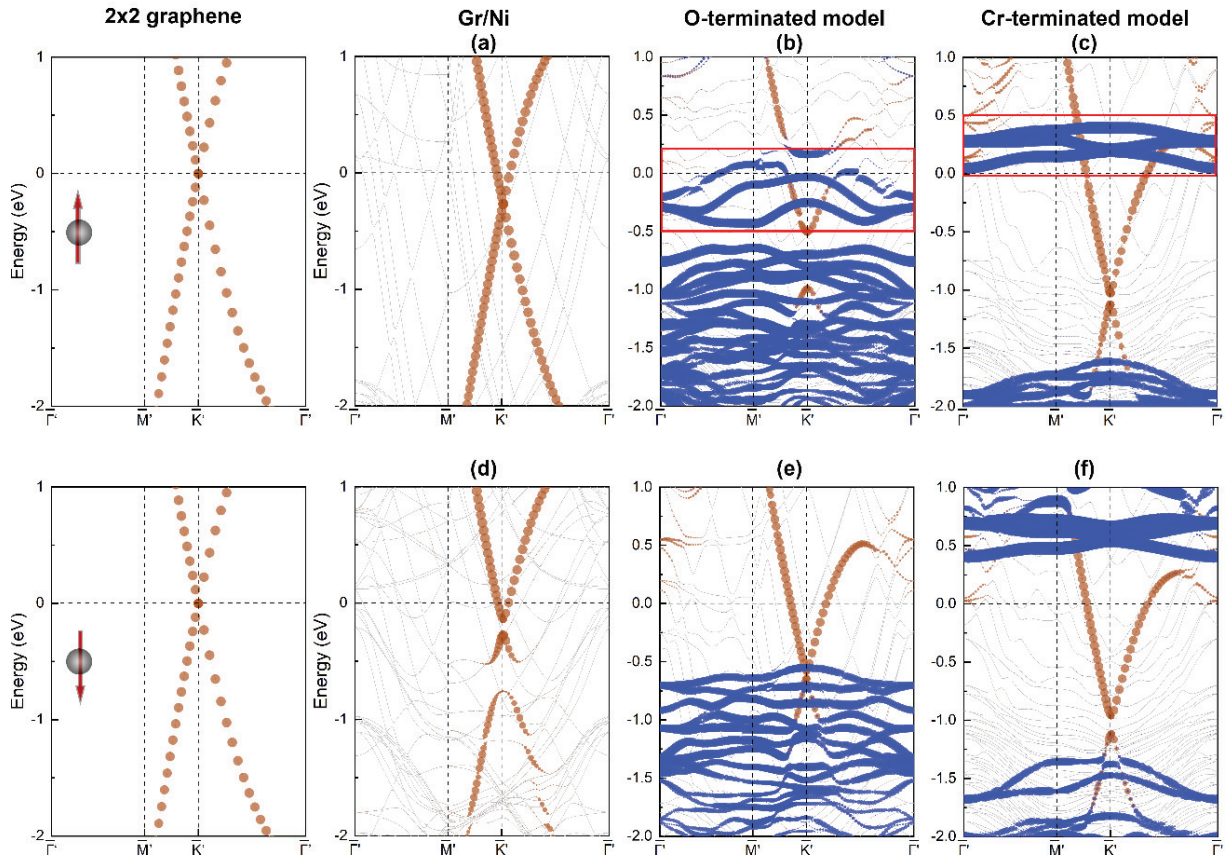


Figure 3.6 Spin-up band structure of (a) Gr/Ni(111), (b) O-terminated model, and (c) Cr-terminated model, (d-f) are corresponding spin-down band structures. Brown and blue lines represent C and Cr states, respectively. The carbon band of 2×2 graphene is given in the left panel for reference. The E_F is set to 0. The mid-gap states of Cr are highlighted by red frames. [76]

Another intriguing finding in the spin-up band is the appearance of mid-gap states of Cr_2O_3 near E_F converting Cr_2O_3 from an antiferromagnetic insulator to a half-metal, as highlighted by the red frame in the O-terminated model (**Figure 3.6(b)**). The mid-gap states overlap with the graphene states near E_F , which are mainly derived from the hybridized states between the C p_z and interfacial Cr d_z^2 orbitals (**Figure 3.3(g)**). The mid-gap states originate from the termination truncation of dangling bonds, as illustrated in the DOS (**Figure 3.3(f)**). Charge transfer from the Ni(111) substrate to Cr_2O_3 promotes interfacial band bending, which induces the mid-gap states

to fall into the valence band. Meanwhile, the spin-down channel of Cr_2O_3 retains its insulating properties. Reversing the magnetic direction of the substrate can flip the spin channel of the mid-gap states (**Figure 3.7**). Note that the transition from the insulator to half-metal of Cr_2O_3 is closely linked to the spin-dependent bandgap opening in graphene, as well as the magnetization direction of the substrate.

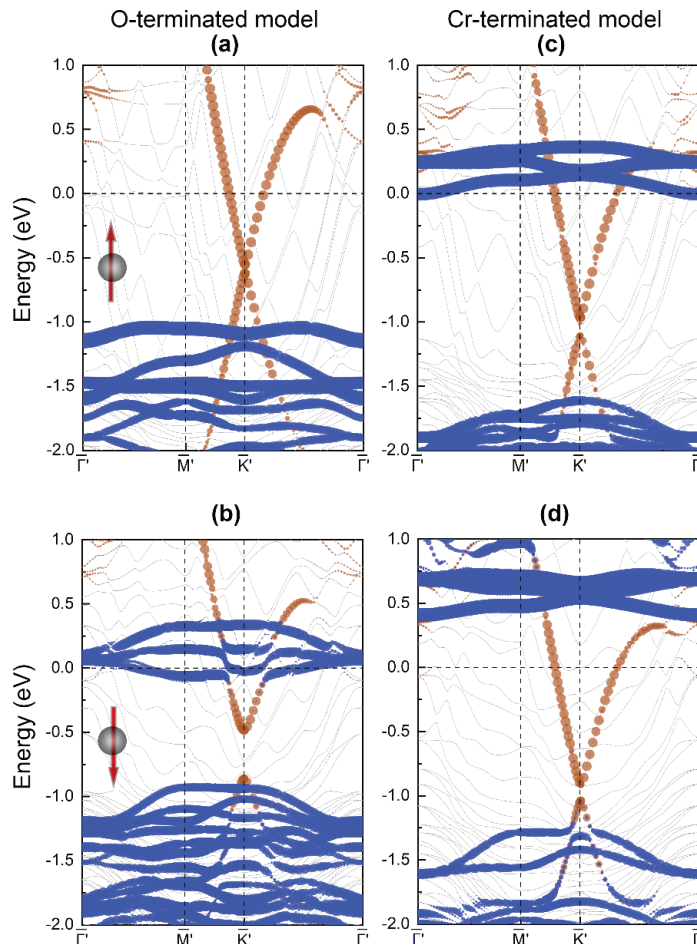


Figure 3.7 The element-resolved band structure of (a) spin-up (b) spin-down in O-terminated $\text{Cr}_2\text{O}_3/\text{Gr}/\text{Ni}(111)$ when magnetic direction of Ni point to substrate direction. (c) Spin-up and (d) spin-down bands for the corresponding Cr-terminated model. [76]

The characteristics of the graphene π -band in the Cr-terminated model are different from those in the O-terminated model, which shows a physisorption feature. This conclusion was

supported by the DOS (**Figure 3.3(d)**) and $d_{\text{C-Ni}} = 2.70 \text{ \AA}$. There is also a significant difference in the band alignment of the Cr-derived DOS in **Figure 3.3(g, h)**. By inspecting the linear characteristic of the Dirac cone at the \bar{K}' point (**Figure 3.6(c, f)**), graphene is almost recovered features in the freestanding model with narrow bandgaps (spin-up 0.12 eV and spin-down 0.15 eV). The Dirac cone position is located at energy $\sim -0.97 \text{ eV}$, which is 0.46 eV lower than the uncovered graphene on Ni. In addition, Cr_2O_3 in the Cr-terminated model retains its indirect bandgap (spin-up $\sim 1.61 \text{ eV}$, spin-down $\sim 1.76 \text{ eV}$). The valence band maximum (VBM) and conduction band minimum (CBM) of the Cr_2O_3 films were located at the \bar{K}' and $\bar{\Gamma}'$ points, respectively. Note that the spin-filter effect of graphene was not obvious in the Cr-terminated model. The lineshape and bandgap of graphene agree with previous $\text{Cr}_2\text{O}_3/\text{graphene}$ studies [38], while both Cr_2O_3 and graphene band structures are energetically lowered because of Ni substrate-induced the charge transfer. Apart from charge-transfer-induced band offset, the insulating feature of the simple Cr_2O_3 slab remains in the Cr-terminated model.

3.6 Conclusion

The structural models, DOS and band structure of $\text{Cr}_2\text{O}_3/\text{Gr}$ on Ni(111) substrate was been investigated via the first-principles calculations. The coexistence of O- and Cr-terminated Cr_2O_3 on Gr/Ni(111) was predicted by the DFT calculations. The spin-polarized Cr- $3d_z^2$ mid-gap states were predicated to exist near E_F in O-terminated model calculations. The mid-gap states originate from the hybridization between the interfacial C p_z and Cr d orbitals, the spin direction of which can be flipped by reversing the substrate magnetization direction. The spin channel controllability of half-metallic mid-gap states can be applied for spin injection or transcription of the boundary ferromagnetic states of Cr_2O_3 into graphene. For the Cr-terminated model, graphene recovers its

linear band dispersion similar to that of the freestanding type while the Cr_2O_3 maintains an indirect bandgap. The spin direction of mid-gap states can be manipulated by the substrate magnetization direction, which enhances the options for the graphene-based spintronic devices.

Chapter 4 ARPES Study of Cr₂O₃/Graphene Interface

4.1 Introduction

Based on previous calculation, a novel spin mid-gap states which can flip with substrate Ni(111) magnetization direction, was found in Cr-terminated Cr₂O₃ model. Benefited from the in-situ MBE fabrication, transfer, and characterization and measurement system, detection of the band structure of Cr₂O₃ ultrathin films is possible to achieve in BL1 of HiSOR. The directly characterization of Cr₂O₃ ultrathin films is meaningful for verifying the conclusion of calculation and also paving a way for further possible applications in devices. In this chapter, we will reveal the interface and terminational band structure by ARPES, and focus on inspecting the mid-gap states of Cr₂O₃ ultrathin films.

4.2 Experimental Methods

All experiments were performed *in-situ* under UHV conditions ($p \sim 10^{-9}$ Pa). The Ni(111) single crystal was cleaned using several cycles of ion sputtering (1 keV Ar⁺ ions for 180 min) and annealing (923 K for 5 min) until no contamination was detected by AES. Graphene was grown on a Ni(111) surface at 773 K by exposing propylene (C₃H₆) gas at a partial pressure of $p_{\text{C}_3\text{H}_6} = 1 \times 10^{-4}$ Pa for 5 min and post-annealed at 773 K under UHV conditions for 5 min. Under these conditions, the graphene synthesis reaction is self-limiting^[89]. No further growth of extra-carbon layer was possible on the graphene-passivated surfaces. Therefore, the synthesis always results in the formation of a complete single graphene monolayer, which has been proven by the stable C/Ni

AES intensity ratio. A LEED study of the Gr/Ni(111) system revealed a well-ordered $p(1\times 1)$ -structure, as expected from the slight lattice mismatch of only 1.3%.

Ultrathin Cr₂O₃ films were grown by evaporating Cr on the Gr/Ni(111) surface at a pressure of $p_{\text{O}_2} = 2\times 10^{-4}$ Pa and a substrate temperature of 650 K [39]. The average deposition rate of Cr was calibrated using a quartz crystal microbalance and maintained at 0.45 Å/min, the corresponding growth speed of Cr₂O₃ has converted to 1 Å/min. All experiments were performed at Hiroshima Synchrotron Radiation Center (HiSOR), Hiroshima University. The Cr₂O₃ quality was confirmed by in-situ AES spectra and cross-checked by the XAS experiment at BL-14 in HiSOR.

The ARPES experiments were performed on the linear undulator beamline BL-1 at HiSOR [65], employing a high-resolution ARPES spectrometer (VG-SCIENTA R4000). The electric-field vector and the k direction in the ARPES experiments lie within the plane of incidence of linearly polarized undulator radiation (p -polarization geometry). The samples were measured at 30 K in an ultrahigh vacuum better than 5×10^{-9} Pa. The overall energy and angular resolutions of the ARPES experiments were set at 15-30 meV and 0.8°, respectively.

4.3 Sample Characterization

The Cr₂O₃ ultrathin films for the ARPES experiment were grown on Gr/Ni(111) using the molecular beam epitaxy (MBE) method in ultrahigh vacuum (UHV). The graphene quality was confirmed by low energy electron diffraction (LEED) and cross-checked by the Auger electron spectroscopy (AES) spectrum of the C-KVV line (**Figure 4.1(a–d)**). The C-KVV in the AES spectra indicates that the film included both sp^2 hybridized carbon and carbidic carbon [25]. The AES spectra show that the Cr LMV and O KVV lines overlap near 500 eV, which makes it difficult

to directly analyze the chemical composition of Cr_2O_3 using the sensitivity factor. However, the Cr and O peak intensity ratio was almost constant regardless of the oxygen pressure, which varied between 5×10^{-5} and 3×10^{-4} Pa, indicating that the Cr/O ratio was saturated. Therefore, we assumed that, the Cr_2O_3 thin films grown at $p_{\text{O}_2} = 1 \times 10^{-4}$ Pa were uniform. Furthermore, the Cr $L_{2,3}$ X-ray absorption spectrum (XAS) in **Figure 4.1(f)** agrees well with previously reported XAS spectra for Cr^{3+} [40]. Other possible oxidation states, such as Cr^{2+} , Cr^{4+} , and Cr^{6+} , were excluded because the peak shapes in the corresponding XAS spectra were completely different [40].

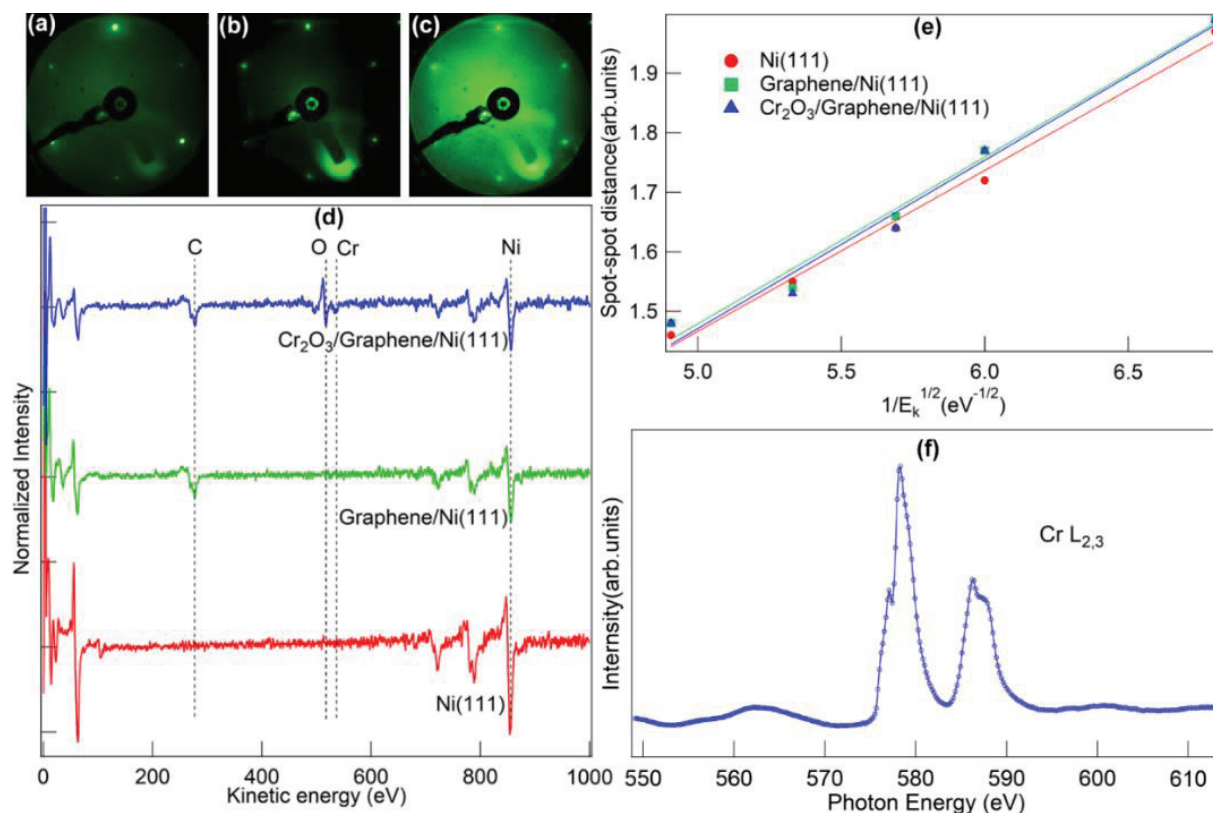


Figure 4.1 (a)-(c) LEED pattern of Ni(111), Gr/Ni(111), 0.7nm-Cr₂O₃/Gr/Ni(111), (d) corresponding differentiated AES spectra at electron energy of 60 eV; (e) spot-spot distance of 0.7nm-Cr₂O₃/Gr/Ni(111); (f) Cr $L_{2,3}$ XAS spectrum of 0.7nm-Cr₂O₃/Gr/Ni(111). [76]

The LEED spots also support the existence of the Cr₂O₃ surface reconstruction. In **Figure 4.1(a-c)**, the LEED pattern of Cr₂O₃/Gr/Ni(111) is similar to that of Gr/Ni(111), but the background is brighter. **Figure 4.1(e)** shows the measured distance between the diffraction spots for Cr₂O₃/Gr/Ni(111) (red circles), Gr/Ni(111) (green squares), and Ni(111) (blue triangles) as a function of $1/\sqrt{E_k}$. The spot-spot distance of 0.7 nm-Cr₂O₃/Gr/Ni(111) coincides with that of Gr/Ni(111). Thus, the surface of Cr₂O₃/Gr/Ni(111) was different from that of bulk Cr₂O₃ [90], whose spot-spot distance should be smaller than that of Gr/Ni(111). The experimental distances were fitted using a straight line passing through the origin of the axes. These three lines are close to each other, indicating that the surface of the Cr₂O₃ thin film has nearly the same in-plane lattice constant as the Gr/Ni(111) substrate [91]. The surface of the Cr₂O₃ thin film was highly compressed and reconstructed, which is consistent with the calculated surface configuration in **Figure 3.2** and the experimental observation by Lodesani *et al* [39]. Our LEED pattern confirms that the epitaxial Cr₂O₃ ultrathin films have the similar lattice constant with Gr/Ni, which is in agreement with previous studies[39, 42]. The calculation confirmed that the surface was reconstructed and compressed along with *c* directions.

4.4 ARPES Experiment

To examine the calculated band structures of Cr₂O₃/Gr/Ni(111), we measured ARPES spectra at the $\bar{\Gamma}$ point with different thicknesses of Cr₂O₃ (0, 0.5, 0.7 and 1.0 nm) (**Figure 4.2**). The corresponding energy distribution curve (EDC) intensity is shown in **Figure 4.3**. For Gr/Ni(111), the main peak of Ni-3*d* is located at energy \sim -1.49 eV. As the thickness of Cr₂O₃ reaches to 0.5 nm, the spectral intensity of the Cr-3*d* main peak is mixed with the Ni-3*d* main peak and moves to lower energy (-1.51 eV) (**Figure 4.3**). The broad spectral features at an energy of -8~-4 eV mainly

originate from O-2*p* states, which are hybridized with Cr-3*d* states [92]. As the thickness of Cr₂O₃ increased to 1 nm, the signals from Cr₂O₃ thin film were enhanced, while those from the substrate and graphene were suppressed. The Ni-3*d* and C-2*p* signals almost disappeared after the deposition of the 0.7nm-Cr₂O₃ film. The Cr 3*d* states form a weakly dispersive band at an energy of -1.89 eV, which is consistent with previous PES [93] and STS experiments [39]. This state is associated with emission from the Cr 3*d* *t*_{2g} spin-up states and acts as the initial state for bandgap excitation.

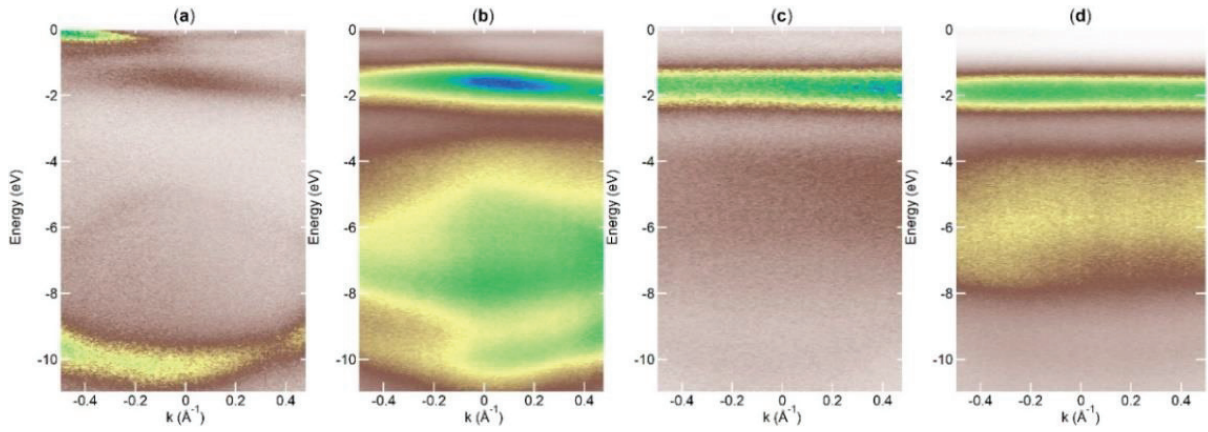


Figure 4.2 ARPES intensities at Γ point of (a) 0 nm, (b) 0.5 nm, (c) 0.7 nm, and (d) 1 nm-Cr₂O₃ thin films deposited on Gr/Ni(111).

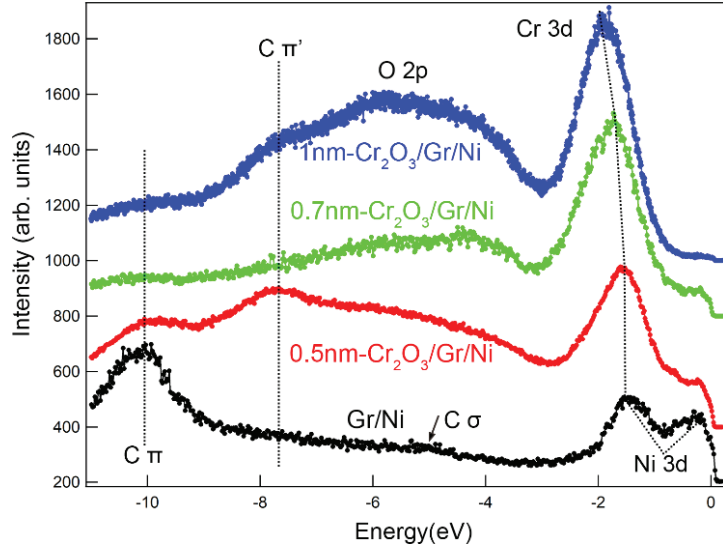


Figure 4.3 EDC of Gr/Ni(111), 0.5nm-Cr₂O₃/Gr/Ni(111), 0.7nm-Cr₂O₃/Gr/Ni(111), 1nm-Cr₂O₃/Gr/Ni(111) at Γ point. [76]

As the position of Ni-3d states in ARPES is close to that of the Cr-3d states, we crosschecked the existence of the Cr-3d states by resonant photoemission spectroscopy at the Cr $3p \rightarrow 3d$ excitation threshold [94, 95] (Figure 4.4). One can see from the resonance feature in Figure 4.4, the Cr component emphasized in low photon energy due to the resonance behavior, while the substrate Ni emphasized in high energy due to the cross-section effect. The corresponding EDC cut around $\bar{\Gamma}$ point spectra are plotted in Figure 4.5. As shown in the $h\nu$ -dependent EDC spectra in Figure 4.5, the peak at energy ~ -1.89 eV is significantly enhanced at $h\nu = 45\sim 55$ eV, confirming the existence of the Cr-3d state. This result is consistent with previous results [94, 95] that maximum Cr-3d resonance energy was observed between $h\nu = 45\sim 55$ eV. Interestingly, the states near E_F also exhibited a similar resonant enhancement in the range of $h\nu = 45\sim 55$ eV. It indicates that Cr 3d also contributes to the states at -0.2 eV near E_F , which is hard to distinguish in detail from the

background signals of Ni(111) without resonant photoemission spectroscopy. In **Figure 4.3**, one can recognize a peak at -0.2 eV for both 0.5-nm and 0.7-nm Cr₂O₃/Gr/Ni(111). But the peak disappears for 1-nm sample, indicating that it originates from the interface.

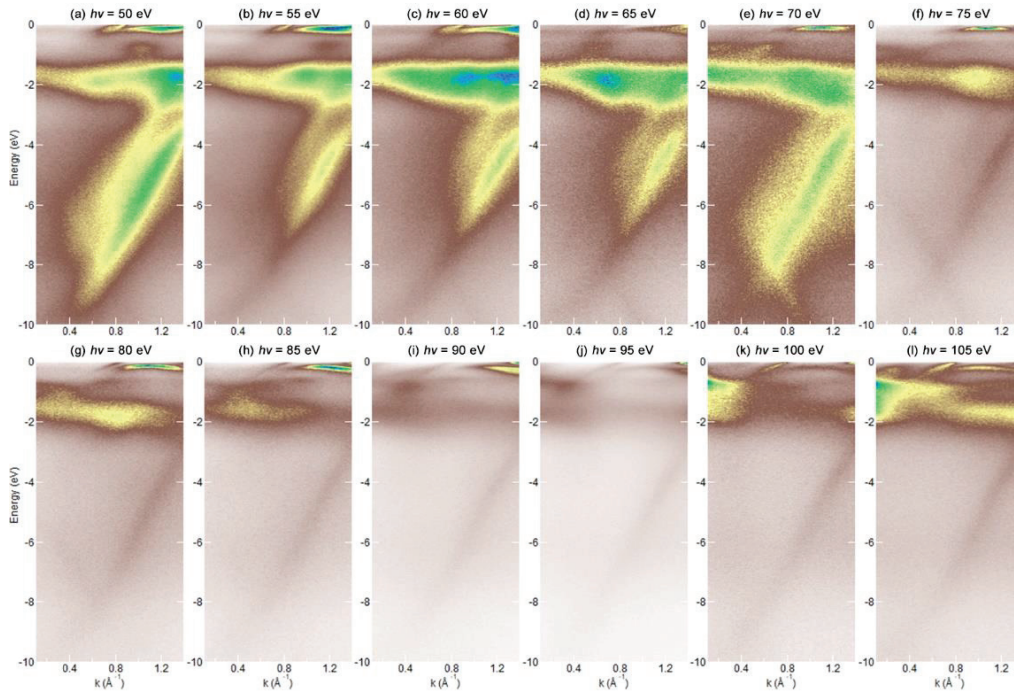


Figure 4.4 ARPES spectra of 0.7nm-Cr₂O₃/Gr/Ni(111) along $\overline{\Gamma K}$ direction.

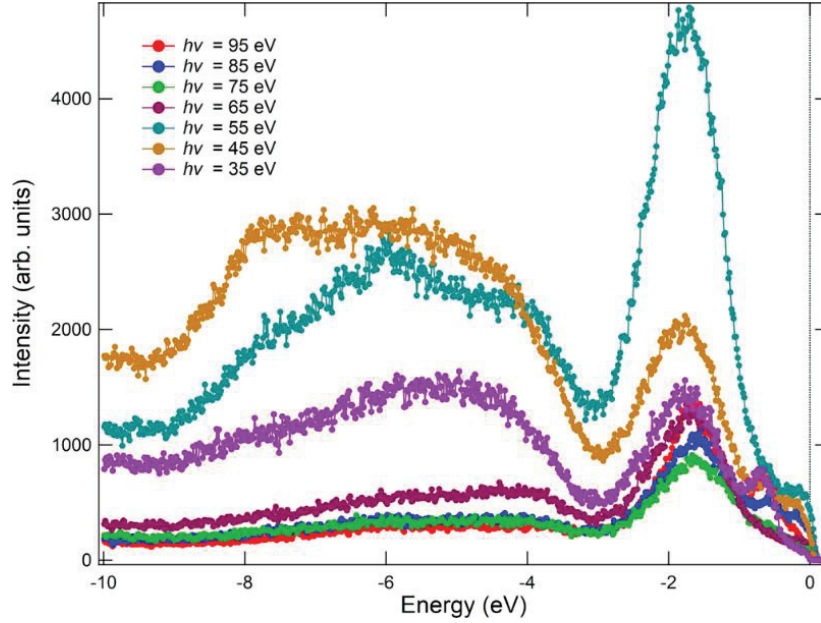


Figure 4.5 Photon energy dependence of 0.7nm-Cr₂O₃/Gr/Ni(111) around $\bar{\Gamma}$ point. [76]

To confirm the mid-gap state-derived peak feature, we overlay the Fermi-Dirac distribution function on the energy distribution curve (EDC) from the 0.7nm-Cr₂O₃/Gr/Ni(111) sample in **Figure 4.6**. As shown in the **Figure 4.6**, the mid-gap state exists at -0.2 eV, which is distinct from the Fermi edge spectral feature. The spectral intensity near E_F varying with the thickness of Cr₂O₃ hints that the band originates from the interfacial mid-gap states of Cr-3d. For the Cr₂O₃ bulk crystal, the mid-gap states cannot be detected in the photoelectron spectra because they are located above E_F . Such mid-gap states can be observed if the film is sufficiently thin. When Cr₂O₃ ultrathin films were deposited on Ni substrate, the charge transfer from the Ni substrate modified the energy position for free-standing Cr₂O₃ ultrathin films, as shown in the gray part of the DOS in **Figure 3.3 (g, h)**. The mid-gap states of the O-terminated model (**Figure 3.6 (c)**) perfectly explain the photoemission resonance enhancement near E_F .

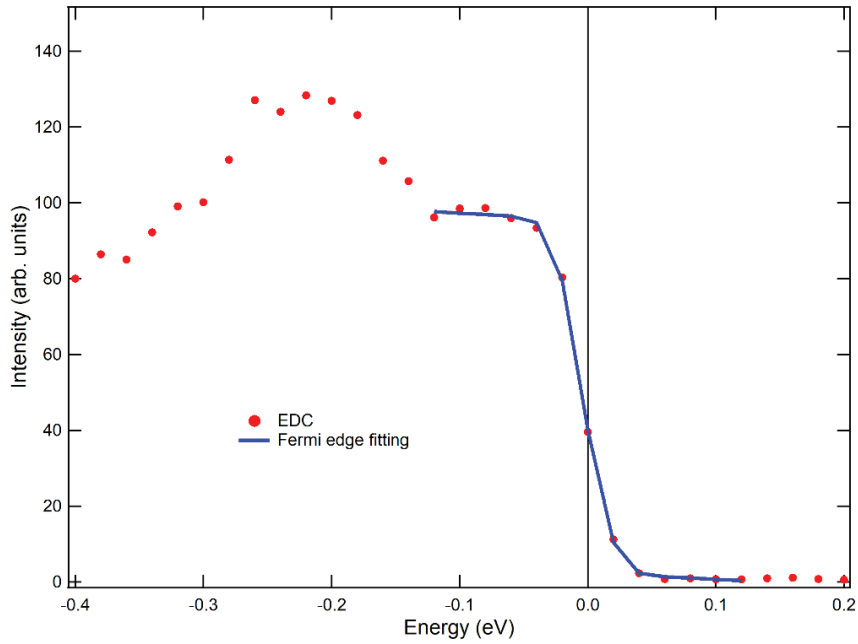


Figure 4.6 EDC curve and fitting of 0.7nm-Cr₂O₃/Gr/Ni(111) sample; the data was collected at $h\nu = 50$ eV. [76]

The ARPES spectra of Cr₂O₃/Gr/Ni(111) after two times differentiation along the $\bar{\Gamma}\bar{K}$ and $\bar{\Gamma}\bar{M}$ directions are shown in **Figure 4.7**. One can find that the main spectral features of the Gr/Ni(111) sample (**Figure 4.7(a, d)**) are in good agreement with previous reports [26, 84, 96]. The as-grown monolayer graphene on Ni(111) is *n*-type, and the bottom of the π band is approximately -10 eV. In **Figure 4.7 (f, h)**, the mid-gap states are confirmed in a 0.7 nm-sample both along the $\bar{\Gamma}\bar{K}$ and $\bar{\Gamma}\bar{M}$ directions. As observed from the EDC in **Figure 4.3**, a new π' band appears at energy of -7.8 eV after the Cr₂O₃ deposition. The π' band (energy of -7.8 eV) coexists with the previous π band (energy of -10 eV) regardless of the variation of Cr₂O₃ thickness. In previous reports, the adsorption of adatoms (Au, nitrogen [84], [97]) on Gr/Ni(111) resulted in a similar increase in the energy of π band. Assuming the adatom-derived energy shift, the π band at energy of -10 eV should

be replaced by the π' band at energy of -7.8 eV after the graphene surface is fully covered by adatoms [97]. However, the replacement of π by the π' band was not observed in our repeated experiments, indicating that the observed spectral features cannot be simply explained by intercalation theory [86, 97]. The calculation gives a possible explanation for the phenomena, that is, O- and Cr-terminated Cr_2O_3 thin films coexist on the surface of Gr/Ni(111). The graphene π band of the Cr_2O_3 deposited sample shows an n -doped dispersion and a weak bandgap at the \bar{K} point (**Figure 4.7(b)**), corresponding to the O-terminated model (**Figure 3.6(b, e)**). The π' band has quasi-linear characteristics around the \bar{K} point, which is consistent with the Cr-terminated model in **Figure 3.6(c, f)**. According to the ARPES results, the spectral features at ~ -1.9 eV are mainly derived from the Cr $3d$ states, in agreement with the theoretical band dispersion of the Cr-terminated model in **Figure 3.6(c, f)** and theoretical DOS in **Figure 3.3 (g)**. Note that a weak band appears near E_F (energy ~ -0.2 eV), which originates from the mid-gap states, as predicted by the calculation in **Figure 3.6(b, c)**. The coexistence of π' and π bands in the experiment is consistent with the calculation, because the Dirac cone positions of O- and Cr- terminated models are different for the same calculation parameters.

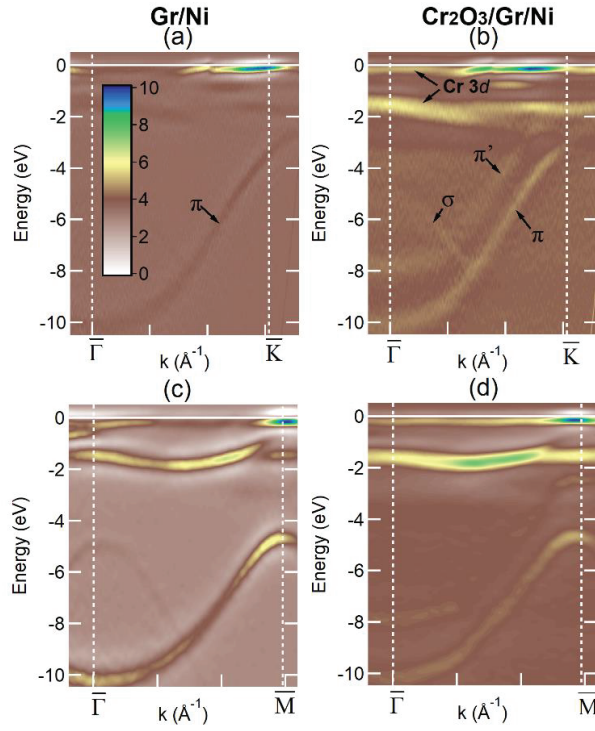


Figure 4.7 ARPES intensities after 2 times differentiation along $\overline{\Gamma\text{K}}$ direction of (a) Gr/Ni(111) and (b) 0.7nm-Cr₂O₃/Gr/Ni(111); ARPES intensities along $\overline{\Gamma\text{M}}$ direction of (c) Gr/Ni(111) and (d) 0.7nm-Cr₂O₃/Gr/Ni. [76]

4.5 Discussion

Next, we examined the details of the band dispersion near E_F as shown in **Figure 4.8(a-d)**. The band dispersion of Cr 3d states is flatter than that of Ni 3d states. By inspecting the band dispersion along the $\overline{\Gamma\text{K}}$ direction in **Figure 4.8(a, b)**, Gr/Ni has no flat states near E_F , but flat band features emerge after the Cr₂O₃ layer growth. The $\overline{\Gamma\text{M}}$ direction bands show that the Cr-based flat band was newly developed at an energy of -0.2 eV. In **Figure 4.8(c, d)**, there are two dispersive bands at the $\overline{\Gamma}$ point for Gr/Ni, whereas only a flat band is observed along the $\overline{\Gamma\text{M}}$ direction for

$\text{Cr}_2\text{O}_3/\text{Gr}/\text{Ni}$. The zoomed-in ARPES spectra along the $\overline{\Gamma\text{K}}$ and $\overline{\Gamma\text{M}}$ directions clearly indicate the existence of dispersionless $\text{Cr-}3d$ mid-gap states.

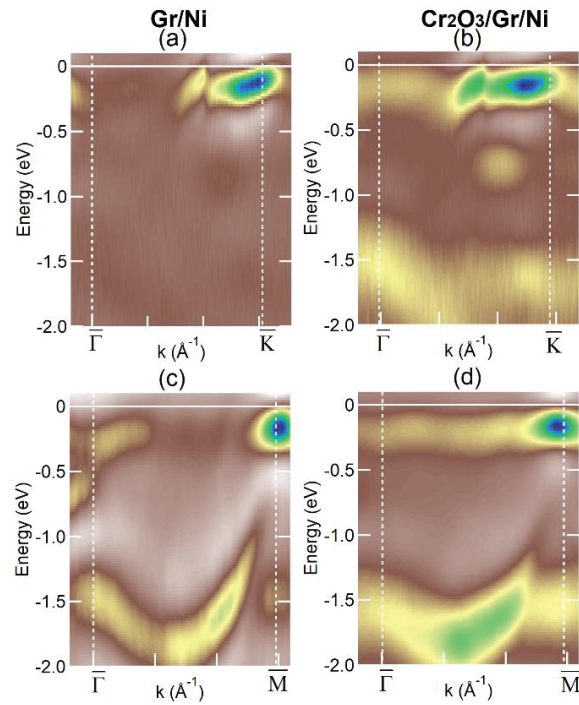


Figure 4.8 Zoom-in ARPES intensities of **Figure 4.7** along $\overline{\Gamma\text{K}}$ direction of (a) $\text{Gr}/\text{Ni}(111)$ and (b) $0.7\text{nm-Cr}_2\text{O}_3/\text{Gr}/\text{Ni}(111)$; zoom-in ARPES intensities along $\overline{\Gamma\text{M}}$ direction of (c) $\text{Gr}/\text{Ni}(111)$ and (d) $0.7\text{nm-Cr}_2\text{O}_3/\text{Gr}/\text{Ni}$. All the data collected at $h\nu = 50$ eV. [76]

The calculated band structures of Ni element in the O- and Cr-terminated models are plotted in **Figure 4.9**. The corresponding DOS for each model was supplied. By comparing the Cr (blue lines) and Ni bands (gray lines) in **Figure 4.9**, Cr $3d$ is mixed with Ni $3d$ near E_F . As shown in the red frames in **Figure 4.9(a, c)**, the spin-resolved DOS of Cr also shows an amplitude comparable to that of the Ni-DOS near E_F . Note that Cr_2O_3 in the Cr-terminated model maintained its insulating

properties. The calculations for the O- and Cr-terminated models show that the Ni bands are more dispersive and pass the E_F whereas the mid-gap states of Cr are flatter and localized within a narrow energy range near E_F . Thus, the calculation results are consistent with the ARPES spectra and the corresponding resonant photoemission experiments.

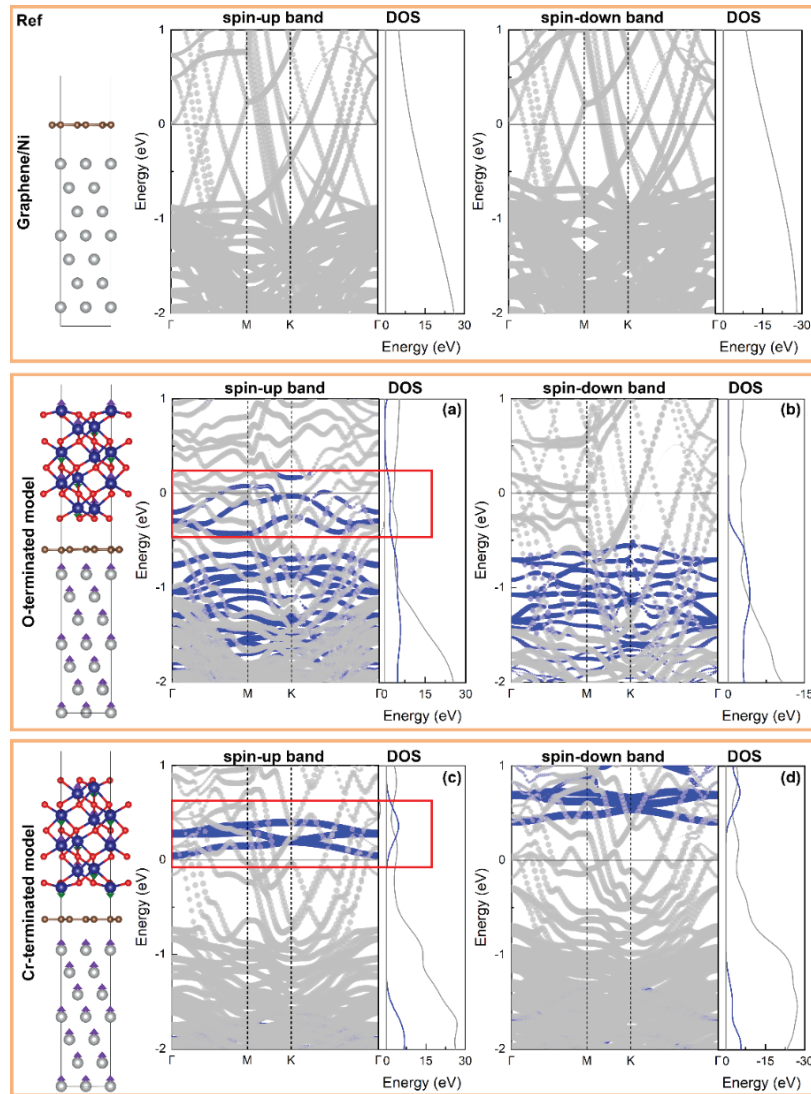


Figure 4.9 (a) spin-up and (b) spin-down band/DOS of Ni element in O-terminated model; (c) spin-up and (d) spin-down band/DOS of Ni element in Cr-terminated model. The Cr and Ni bands are plotted via blue and gray colors. [76]

Considering the deposition temperature (~ 650 K) of the Cr_2O_3 thin film which is much higher than the energy difference between the O- and Cr-terminated $\text{Cr}_2\text{O}_3/\text{Gr}/\text{Ni}(111)$ models in our calculation, the coexistence of different types of interface termination is possible from the viewpoint of thermal energy. In addition, the O- and Cr-terminated models represent the interface structure that are compatible with the observed LEED spots (**Figure 4.1 (a-c)**). As shown in **Figure 3.2 (a, b)**, the LEED pattern was highly influenced by the surface structure. Our calculations confirm that both the surfaces of the O- and Cr-terminated models are reconstructed and compressed along the c directions, which is consistent with the fact that the LEED spots of $\text{Cr}_2\text{O}_3/\text{Gr}/\text{Ni}(111)$ are the same as those of $\text{Gr}/\text{Ni}(111)$ [42]. Furthermore, the calculated $d_{\text{C-Ni}}$ in $\text{Gr}/\text{Ni}(111)$ agrees well with the previous calculation[80-82] and experimental value (2.1 Å) [98].

4.6 Conclusion

Ultrathin Cr_2O_3 films with thickness varies from 0 to 1 nm were fabricated on graphene covered $\text{Ni}(111)$ surface by MBE method. The quality of sample was confirmed by in-situ AES, LEED and XAS. The interfacial valence structure of $\text{Cr}_2\text{O}_3/\text{Gr}/\text{Ni}(111)$ was been investigated in detail using ARPES. The coexistence of π and π' bands are observed in ARPES measurements, which is consistent with the prediction in Cr- and O- termination models calculation, respectively. More interestingly, the near E_F states were observed and confirmed to have Cr characteristic by zoom-in ARPES spectra. The states show a similar resonant behavior as Cr-3d main peaks, which enhance around 45~55 eV. The means that the near E_F states originate from the hybridized mid-gap states of Cr_2O_3 . The Ni-contribution to near E_F states can be omitted due to its more dispersive and passing natures at the E_F , while the Cr-mid gap states is just proved from its flatter dispersion

and localized nature. Our ARPES results confirm the existence of mid-gap states on Cr_2O_3 for the first time, which is consistent with our DFT prediction. The experiment suggested that termination is critical for ultrathin Cr_2O_3 films band structure. By controlling the surface configuration, Cr_2O_3 have potential to applied in spintronic devices.

Chapter 5 DFT Calculation Study of Ultrathin CrTe₂ Films

5.1 Introduction

The discovery intrinsic ferromagnetism at ultrathin van der Waals(vdW) films CrTe₂ have attracted considerable interest. The bulk CrTe₂ possesses FM ground states with a high Curie temperature of 310 K. The basic structure of bulk CrTe₂ is shown in **Figure 5.1(a, b)**, the corresponding element resolved band is shown in **Figure 5.1(c)**. Recent research found that the ultrathin CrTe₂ films exhibit FM properties at room temperature [99], while the others observed its AFM order at atomic scale in ML crystal[44]. There is also a prediction that the magnetism is varies with strain or doping. The conffliction makes it being an open issue to study the magnetism configuration of ultrathin CrTe₂ films. This chapter is devoted to calculation study of ultrathin CrTe₂ films, providing a guideline for experimental works.

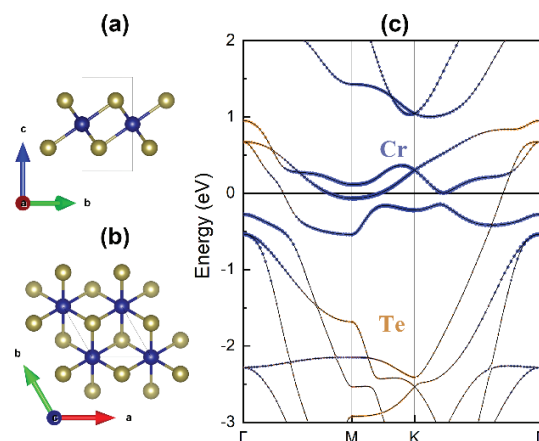


Figure 5.1 (a) Side view and (b) top view of bulk CrTe₂, Cr and Te are represented by blue and yellow, respectively; (c) element-resolved band structure of CrTe₂ (van der Waals effect and Hubbard U effect of Cr are included).

5.2 Simulation Parameters

The first-principle calculations of CrTe₂ were performed within the generalized gradient approximation (GGA) method using the VASP code [72, 73] and a plane wave energy cutoff of 520 eV. The exchange-correlation interaction was described by the Perdew–Burke–Ernzerh (PBE-GGA) [74]. The Hubbard $U = 2$ eV for Cr is included based on previous reports [12, 44, 100]. All atoms were allowed to relax until the residual force per atom was less than 0.01 eV/Å and energy difference was less than 10^{-6} eV. The initial magnetic moment of Cr was set to be 5 μ_B . The uniform Monkhorst-Pack k mesh of $9 \times 9 \times 9$ and $7 \times 7 \times 1$ were adopted for bulk and slabs integration over the Brillouin zone, respectively. All the slabs possess vacuum layers of 15 Å along the out-of-plane direction to eliminate the interaction among layers. The vdW correction was adopted [79] with a long-range dispersion correction (DFT-D2) in slab models. Magnetic configuration of slabs is shown in **Figure 5.2**. The 2×2 supercell was selected for match the basic requirement of the AFM magnetic configuration.

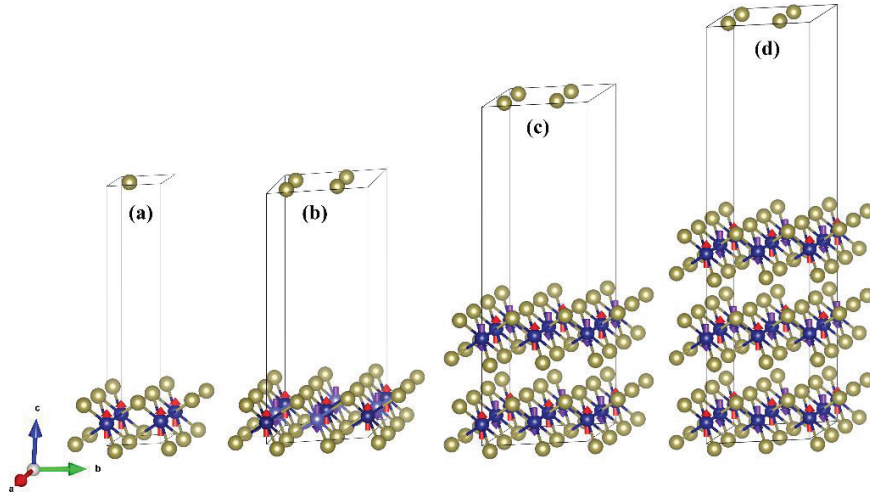


Figure 5.2 (a) FM configuration of 1UC CrTe₂, (b)-(d) are zigzag-AFM configuration of 1-3UC CrTe₂.

5.3 Magnetic Configuration

When thickness of CrTe₂ decrease to several layers, its electronic properties change dramatically. Recently, magnetic response of 1 ML CrTe₂ has been investigated via XMCD, which suggests that the ferromagnetism is kept for 1 ML CrTe₂ [46]. The slab model of 1UC slab with FM configuration is shown in **Figure 5.2(a)**, whose thickness is changed in the calculation, keeping common atomic configuration in each layer. In order to determine the trend of electronic properties of CrTe₂ changes with thickness, the thickness dependence of DOS and spin-polarization of CrTe₂ are plotted in **Figure 5.3**. To simplify the calculation, FM ground states are selected for all the slabs. As seen from **Figure 5.3 (a)**, the DOS accumulated with similar trends as thickness increase, the bulk properties are almost recovered for 3UC slabs. Besides, the thickness dependent spin-polarization shows a different characteristic, as found in **Figure 5.3 (b)**. It is clear that the spin-polarization oscillation of 1UC (red curve) and 2UC (orange curve) films are stronger than that of

the others, which are originated from the lack of interlayer interactions. Besides, the spin-polarization of 1UC-CrTe₂ (red curve) near E_F is smaller than those of 2-7 UC CrTe₂. Thus, we will keep the focus on the different magnetic configuration of 1-3UC slabs in further discussion.

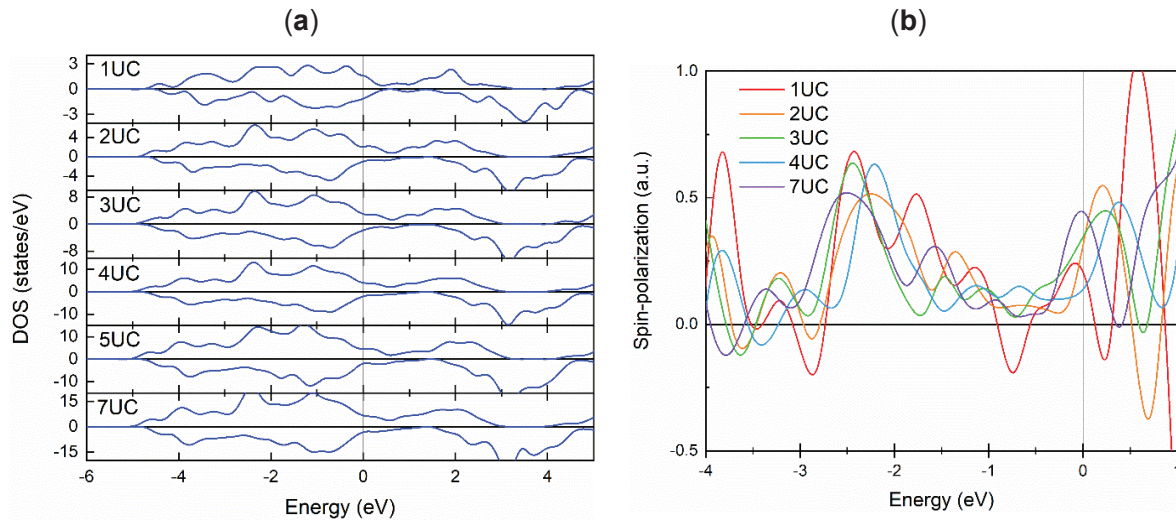


Figure 5.3 (a) Spin-resolved DOS and (b) spin-polarization of 1-7 UC CrTe₂ slabs with FM ground states.

There are several reports discussed the magnetic configurations of 1T- CrTe₂. Based on their prediction, the zigzag antiferromagnetic configuration has the lowest binding energy. Thus, we also considered innerlayer and interlayer AFM zigzag configuration in calculation, as highlighted by the arrow directions in **Figure 5.2(b-d)**. The DOS of 1-3UC slabs with AFM configuration is shown in **Figure 5.4**. It is clear that the unoccupied states at 3.5 eV above E_F for 1UC and 2UC are more dispersive than that of the 3UC slab, which is originated from the surface dangling bonds. The DOS of 3UC slab shows a localized characteristic. The detailed orbital-resolved bands are shown in **Figure 5.5**, one can see the unoccupied states at 3.5 eV of 1UC and

2UC is contributed by in-plane orbitals including Cr- $3d_{xy}$, d_{yz} , d_{zx} , $d_{x^2-y^2}$ orbitals (left panel) and Te- p_x/p_y orbitals (right panel).

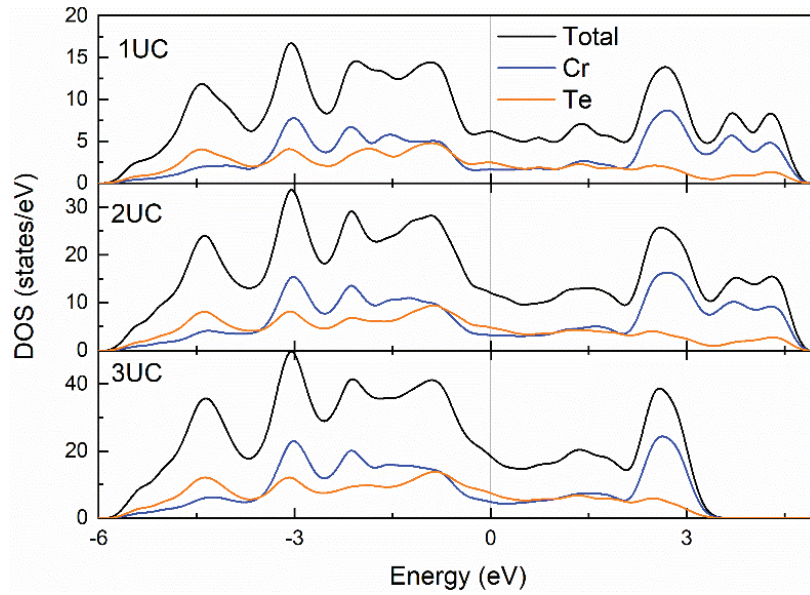


Figure 5.4 DOS of 1-3 UC CrTe₂ slabs with AFM configuration.

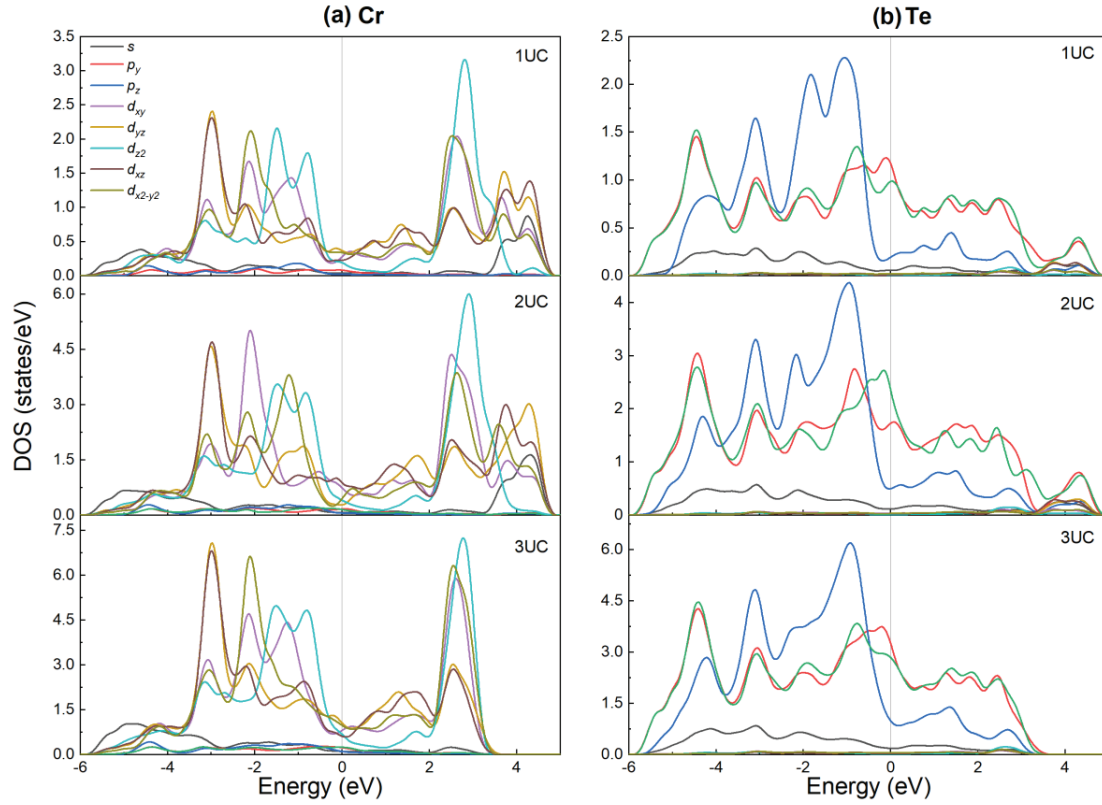


Figure 5.5 (a) orbital-resolved DOS of Cr element in 1-3UC CrTe₂ slabs; (b) orbital-resolved DOS of Te element in 1-3UC CrTe₂ slabs.

5.4 CrTe₂/Graphene

In order to consider the effect of buffer layer, graphene is introduced in the bottoms of slabs, as shown in **Figure 5.6**. The most energy stable models are selected based on previous report [44], in which Te atoms embedded on the center position of honeycombed graphene, as seen from **Figure 5.6(a)**. The CrTe₂ slabs were enlarged to 2×2 to match the 3×3 graphene supercell. The in-plane lattice constant is fixed to 3×3 graphene supercell and the lattice mismatch level is about 3.94%. The thickness of CrTe₂ is fixed to 1 and 2 UC with a 15 Å vacuum layer. The FM configuration for CrTe₂ is fixed. The optimized interlayer-distance between CrTe₂ and graphene

for 1UC and 2UC models are 4.44 Å, and 3.56 Å, respectively. The large interlayer distance means CrTe₂ is physisorption on graphene and has weak interaction with substrate.

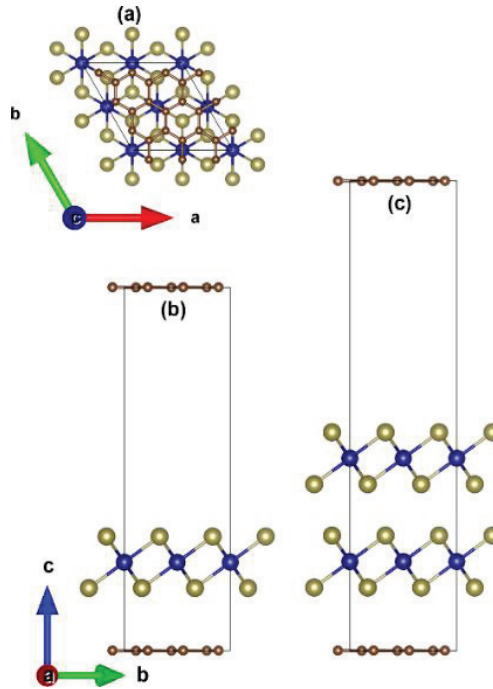


Figure 5.6 (a) Top view of CrTe₂/graphene model, side view of (b) 1UC, (c) 2UC CrTe₂/graphene model.

The DOS for 1UC and 2UC CrTe₂/graphene slabs are plotted in left and right panel, respectively, as seen from **Figure 5.7**. The basic DOS distribution of 1UC slab are similar to that of 2UC. It should be noticed that a peak shows up near E_F in 1UC-CrTe₂ as highlighted by red frame, which is contributed by the spin-up channel of Cr- $3d_z^2$ orbitals and Te- p_z orbital. As we can see from the spin-polarization of 1UC and 2UC CrTe₂ on graphene in **Figure 5.8**, the spin-polarization of 1UC is stronger than that of 2UC films. By comparing the spin polarization of 1UC

and 2UC CrTe₂ with/without graphene (**Figure 5.8/Figure 5.3 (b)**), it is obvious that the graphene weakened the spin-oscillation of ultrathin CrTe₂ films and made it shows a more bulk-like characteristic. The recovery of bulk properties in 1UC and 2UC CrTe₂ on graphene hints that the oscillation comes from the unpaired dangling bonds.

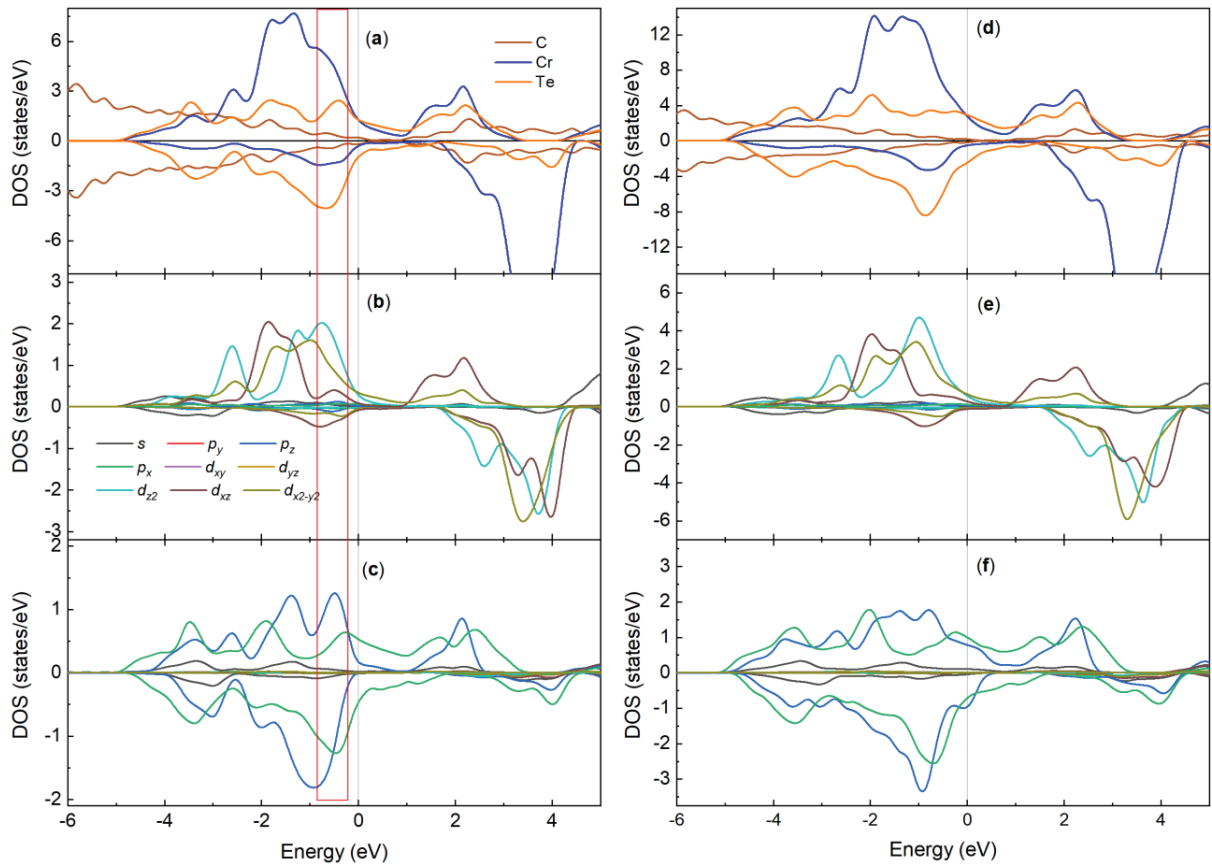


Figure 5.7 Left panel: (a) Element-resolved DOS, (b) Cr-orbital contribution, (c) Te-orbital contribution for 1UC CrTe₂/graphene model; right panel: (c)-(d) are corresponding DOS for 2UC CrTe₂/graphene model.

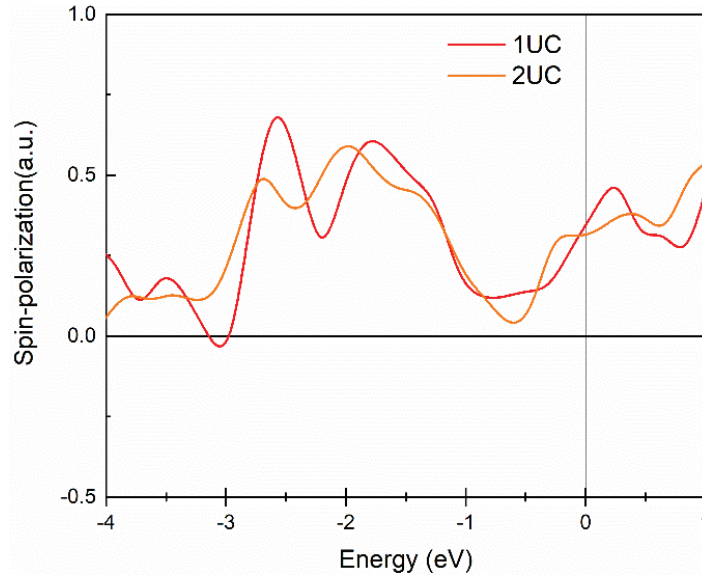


Figure 5.8 Spin-polarization of 1UC and 2UC CrTe₂/graphene model.

5.5 Conclusion

To sum up, we calculated the thickness dependent CrTe₂ slabs with the consideration of van der Waals effect and Hubbard U effect. Both of the magnetic configuration and substrate will influence the spin distribution. With the FM configuration, the 3-7UC CrTe₂ slabs recover to bulk characteristic gradually, while the 1 and 2 UC films shows stronger spin-oscillation. With the AFM configuration, the unoccupied in-plane states (Cr-3 d_{xy} , d_{yz} , d_{zx} , $d_{x^2-y^2}$ orbitals and Te- p_x/p_y orbitals) shown up for 1UC and 2UC CrTe₂ slabs. The graphene buffer layer will weaken the spin-oscillation of 1UC and 2UC CrTe₂ slabs and made it recover to its bulk characteristic. The preliminary calculation can act as a guide before experiment and helpful for understanding the electronic structure of ultrathin CrTe₂ films.

Chapter 6 Summary

In summary, the multiferroic materials have attract wide attention due to its adjustable ferroic properties by additional parameters. Thereinto, Cr_2O_3 would be a great research target for its intrinsic multiferroic characteristic. In this work, we use first-principles density functional theory (DFT) calculations and ARPES to study the band structure of $\text{Cr}_2\text{O}_3/\text{Gr}/\text{Ni}(111)$ heterostructure. Our calculations have shown that the electronic band structures are distinct between the O- and Cr-terminated interfaces of the $\text{Cr}_2\text{O}_3/\text{Gr}/\text{Ni}(111)$ heterostructure. An interesting spin-polarized mid-gap states are predicted to exist in the O-terminated model, whose spin direction can be flipped by reversing the substrate magnetization direction. In the ARPES experiments, we have observed the existence of such mid-gap band at the energy of ~ -0.20 eV in interface of Cr_2O_3 and graphene. The mid-gap band was further confirmed to have a Cr nature by resonance photoemission spectroscopy of Cr. Our findings indicate that one can control the spin-polarized mid-gap states in the antiferromagnetic Cr_2O_3 as well as the bandgap of graphene by interface engineering, paving the way for spintronic applications.

The DFT calculation for CrTe_2 slabs is performed for the thickness-controlled experiments in the future. The effect of thickness, magnetic configuration and graphene buffer layer are both considered during calculation. We find that the thickness is crucial for its properties, the CrTe_2 slabs recovers to its bulk properties as thickness increases. Besides, the 1UC and 2UC slabs show a stronger spin-oscillation than that of others. With the AFM magnetic configuration, there will be an unusual unoccupied state at 3.5 eV above the E_F , which is distributed by the in-plane states. The graphene buffer layer will weaken the spin-oscillation of 1UC and 2UC films, and make it recovers to bulk properties.

Reference

- [1] N.A. Spaldin, M. Fiebig, The Renaissance of Magnetoelectric Multiferroics, *Science*, 309 (2005).
- [2] M.N. Baibich, J.M. Broto, A. Fert, F. Nguyen Van Dau, F. Petroff, P. Etienne, G. Creuzet, A. Friederich, J. Chazelas, Giant magnetoresistance of (001)Fe/(001)Cr magnetic superlattices, *Phys Rev Lett*, 61 (1988) 2472-2475.
- [3] P. Curie, Sur la symétrie dans les phénomènes physiques, symétrie d'un champ électrique et d'un champ magnétique, *Journal de Physique Théorique et Appliquée*, 3 (1894) 393-415.
- [4] G.T. Rado, V.J. Folen, Observation of the Magnetically Induced Magnetoelectric Effect and Evidence for Antiferromagnetic Domains, *Physical Review Letters*, 7 (1961) 310-311.
- [5] P.R. Wallace, The Band Theory of Graphite, *Physical Review*, 71 (1947) 622-634.
- [6] Y. Zhang, Y.W. Tan, H.L. Stormer, P. Kim, Experimental observation of the quantum Hall effect and Berry's phase in graphene, *Nature*, 438 (2005) 201-204.
- [7] P. Blake, E.W. Hill, A.H. Castro Neto, K.S. Novoselov, D. Jiang, R. Yang, T.J. Booth, A.K. Geim, Making graphene visible, *Applied Physics Letters*, 91 (2007).
- [8] Hanggu Lee, Xiaoding Wei, Jeffrey W. Kysar, J. Hone, Measurement of the Elastic Properties and Intrinsic Strength of Monolayer Graphene, *Science*, 321 (2008).
- [9] Alexander A. Balandin, Suchismita Ghosh, W. Bao, Irene Calizo, D. Teweldebrhan, Feng Miao, C.N. Lau, Superior Thermal Conductivity of Single-Layer Graphene, *Nano Lett*, 8 (2008) 902-907.
- [10] A. Varykhalov, J. Sanchez-Barriga, A.M. Shikin, C. Biswas, E. Vescovo, A. Rybkin, D. Marchenko, O. Rader, Electronic and magnetic properties of quasifreestanding graphene on Ni, *Phys Rev Lett*, 101 (2008) 157601.
- [11] G. Yang, L. Li, W.B. Lee, M.C. Ng, Structure of graphene and its disorders: a review, *Sci Technol Adv Mater*, 19 (2018) 613-648.
- [12] X. Yang, X. Zhou, W. Feng, Y. Yao, Tunable magneto-optical effect, anomalous Hall effect, and anomalous Nernst effect in the two-dimensional room-temperature ferromagnet $1T\text{-CrTe}_2$, *Physical Review B*, 103 (2021).
- [13] I. Zanella, S. Guerini, S.B. Fagan, J. Mendes Filho, A.G. Souza Filho, Chemical doping-induced gap opening and spin polarization in graphene, *Physical Review B*, 77 (2008).
- [14] Y.-J. Kang, J. Kang, K.J. Chang, Electronic structure of graphene and doping effect on SiO_2 , *Physical Review B*, 78 (2008) 115404.
- [15] B. Zhou, S. Ji, Z. Tian, W. Cheng, X. Wang, W. Mi, Proximity effect induced spin filtering and gap opening in graphene by half-metallic monolayer Cr_2C ferromagnet, *Carbon*, 132 (2018) 25-31.
- [16] S. Qi, J. Jiang, X. Wang, W. Mi, Valley polarization, magnetic anisotropy and Dzyaloshinskii-Moriya interaction of two-dimensional graphene/Janus 2H-VSeX ($X = \text{S, Te}$) heterostructures, *Carbon*, 174 (2021) 540-555.
- [17] N. Feng, W. Mi, X. Wang, H. Bai, First-principles study on the interfacial magnetic and electronic properties of $\text{Fe}_4\text{N}(0\ 0\ 1)/\text{Si}$ and $\text{Fe}_4\text{N}(1\ 1\ 1)/\text{graphene}$ bilayers, *Computational Materials Science*, 96 (2015) 256-262.
- [18] W. Mi, H. Yang, Y. Cheng, G. Chen, H. Bai, Magnetic and electronic properties of $\text{Fe}_3\text{O}_4/\text{graphene}$ heterostructures: First principles perspective, *J. Appl. Phys.*, 113 (2013) 083711.
- [19] S.Y. Zhou, G.-H. Gweon, A.V. Fedorov, P.N. First, W.A. de Heer, D.-H. Lee, F. Guinea, A.H. Castro Neto, and A. Lanzara, Substrate-induced band gap opening in epitaxial graphene.
- [20] V.M. Karpan, P.A. Khomyakov, G. Giovannetti, A.A. Starikov, P.J. Kelly, $\text{Ni}(111)|\text{graphene}|h\text{-BN}$ junctions as ideal spin injectors, *Physical Review B*, 84 (2011).
- [21] I. Hamada, M. Otani, Comparative van der Waals density-functional study of graphene on metal surfaces, *Physical Review B*, 82 (2010) 153412.
- [22] G. Giovannetti, P.A. Khomyakov, G. Brocks, V.M. Karpan, J. van den Brink, P.J. Kelly, Doping graphene with metal contacts, *Phys Rev Lett*, 101 (2008) 026803.

- [23] P.A. Khomyakov, G. Giovannetti, P.C. Rusu, G. Brocks, J. van den Brink, P.J. Kelly, First-principles study of the interaction and charge transfer between graphene and metals, *Physical Review B*, 79 (2009) 195425.
- [24] R. Balog, B. Jorgensen, L. Nilsson, M. Andersen, E. Rienks, M. Bianchi, M. Fanetti, E. Laegsgaard, A. Baraldi, S. Lizzit, Z. Sljivancanin, F. Besenbacher, B. Hammer, T.G. Pedersen, P. Hofmann, L. Hornekaer, Bandgap opening in graphene induced by patterned hydrogen adsorption, *Nat Mater*, 9 (2010) 315-319.
- [25] J. Lahiri, T. S Miller, A. J Ross, L. Adamska, I.I. Oleynik, M. Batzill, Graphene growth and stability at nickel surfaces, *New Journal of Physics*, 13 (2011) 025001, 025001-025019.
- [26] A. Grüneis, D.V. Vyalikh, Tunable hybridization between electronic states of graphene and a metal surface, *Physical Review B*, 77 (2008) 193401, 193401-193404.
- [27] N. Mishra, J. Boeckl, N. Motta, F. Iacopi, Graphene growth on silicon carbide: A review, *physica status solidi (a)*, 213 (2016) 2277-2289.
- [28] C. Xia, S. Watcharinyanon, A.A. Zakharov, R. Yakimova, L. Hultman, L.I. Johansson, C. Virojanadara, Si intercalation/deintercalation of graphene on 6H-SiC(0001), *Physical Review B*, 85 (2012).
- [29] Y. Kota, H. Imamura, M. Sasaki, Effect of lattice deformation on exchange coupling constants in Cr₂O₃, *Journal of Applied Physics*, 115 (2014).
- [30] D.Ž. Alikhanov R A, Kowalska A, S. KRASNIC, Neutron investigation of the Spin System Dynamics in α -Cr₂O₃, *physica status solidi (b)*, 32 (1969) 41-48.
- [31] I.E. Dzyaloshinskii, On the magneto-electrical effects in antiferromagnets, *Soviet Physics JETP* 10, 628-629 (1960) 708-709.
- [32] Y. Guo, S.J. Clark, J. Robertson, Electronic and magnetic properties of Ti₂O₃, Cr₂O₃, and Fe₂O₃ calculated by the screened exchange hybrid density functional, *Journal of Physics: Condensed Matter*, 24 (2012) 325504, 325501-325508.
- [33] T.S.a.T. Olsen, Magnons in antiferromagnetic bcc-Cr and Cr₂O₃ from time-dependent density functional theory, *arXiv preprint*, (2022) 2203.04796, 02022.
- [34] J.Y. Chen, X.X. Li, W.Z. Zhou, J.L. Yang, F.P. Ouyang, X. Xiong, Large-Spin-Gap Nodal-Line Half-Metal and High-Temperature Ferromagnetic Semiconductor in Cr₂X₃(X=O,S,Se) Monolayers, *Advanced Electronic Materials*, (2019).
- [35] N. Wu, X. He, A.L. Wysocki, U. Lanke, T. Komesu, K.D. Belashchenko, C. Binek, P.A. Dowben, Imaging and control of surface magnetization domains in a magnetoelectric antiferromagnet, *Physics Review Letter*, 106 (2011) 087202.
- [36] X. He, Y. Wang, N. Wu, A.N. Caruso, E. Vescovo, K.D. Belashchenko, P.A. Dowben, C. Binek, Robust isothermal electric control of exchange bias at room temperature, *Nature Materials*, 9 (2010) 579-585.
- [37] Y. Cheng, S. Yu, M. Zhu, J. Hwang, F. Yang, Evidence of the Topological Hall Effect in Pt/Antiferromagnetic Insulator Bilayers, *Phys Rev Lett*, 123 (2019) 237206.
- [38] H. Takenaka, S. Sandhoefner, A.A. Kovalev, E.Y. Tsymbal, Magnetoelectric control of topological phases in graphene, *Physical Review B*, 100 (2019) 125156.
- [39] A. Lodesani, A. Picone, A. Brambilla, D. Giannotti, M.S. Jagadeesh, A. Calloni, G. Bussetti, G. Berti, M. Zani, M. Finazzi, L. Duo, F. Ciccacci, Graphene as an ideal buffer layer for the growth of high-quality ultrathin Cr₂O₃ layers on Ni(111), *ACS Nano*, 13 (2019) 4361-4367.
- [40] M. Asa, G. Vinai, J.L. Hart, C. Autieri, C. Rinaldi, P. Torelli, G. Panaccione, M.L. Taheri, S. Picozzi, M. Cantoni, Interdiffusion-driven synthesis of tetragonal chromium (III) oxide on BaTiO₃, *Physical Review Materials*, 2 (2018) 033401, 033401-033410.
- [41] T.C. Kaspar, D.K. Schreiber, S.R. Spurgeon, M.E. McBriarty, G.M. Carroll, D.R. Gamelin, S.A. Chambers, Built-In Potential in Fe₂O₃-Cr₂O₃ Superlattices for Improved Photoexcited Carrier Separation, *Adv Mater*, 28 (2016) 1616-1622.

- [42] A. Kramer, L. Bignardi, P. Lacovig, S. Lizzit, M. Batzill, Comparison of surface structures of corundum Cr₂O₃(0 0 0 1) and V₂O₃(0 0 0 1) ultrathin films by x-ray photoelectron diffraction, *Journal of Physics: Condensed Matter*, 30 (2018).
- [43] D.C. Freitas, R. Weht, A. Sulpice, G. Remenyi, P. Strobel, F. Gay, J. Marcus, M. Nunez-Regueiro, Ferromagnetism in layered metastable 1T-CrTe₂, *J Phys Condens Matter*, 27 (2015) 176002.
- [44] J.J. Xian, C. Wang, J.H. Nie, R. Li, M. Han, J. Lin, W.H. Zhang, Z.Y. Liu, Z.M. Zhang, M.P. Miao, Y. Yi, S. Wu, X. Chen, J. Han, Z. Xia, W. Ji, Y.S. Fu, Spin mapping of intralayer antiferromagnetism and field-induced spin reorientation in monolayer CrTe₂, *Nat Commun*, 13 (2022) 257.
- [45] L.X. Gao P, Yang J. , Thickness Dependent Magnetic Transition in Few Layer 1T Phase CrTe₂, *Journal of Physical Chemistry Letters*, 12 (2021) 6847-6851.
- [46] X. Zhang, Q. Lu, W. Liu, W. Niu, J. Sun, J. Cook, M. Vaninger, P.F. Miceli, D.J. Singh, S.W. Lian, T.R. Chang, X. He, J. Du, L. He, R. Zhang, G. Bian, Y. Xu, Room-temperature intrinsic ferromagnetism in epitaxial CrTe₂ ultrathin films, *Nat Commun*, 12 (2021) 2492.
- [47] X. Zhang, S.C. Ambhire, Q. Lu, W. Niu, J. Cook, J.S. Jiang, D. Hong, L. Alahmed, L. He, R. Zhang, Y. Xu, S.S. Zhang, P. Li, G. Bian, Giant Topological Hall Effect in van der Waals Heterostructures of CrTe₂/Bi₂Te₃, *ACS Nano*, 15 (2021) 15710-15719.
- [48] M. Opel, Spintronic oxides grown by laser-MBE, *Journal of Physics D: Applied Physics*, 45 (2012).
- [49] M.A.H.T.a.H. Sitter, MBE growth physics. application to device technology, *Microelectronics Journal*, 27 (1997) 257-296.
- [50] D. Mogk, Auger Electron Spectroscopy, in.
- [51] C. Davisson, L.H. Germer, Diffraction of Electrons by a Crystal of Nickel, *Physical Review*, 30 (1927) 705-740.
- [52] M. Gulde, Development of an Ultrafast Low-Energy Electron Diffraction Setup, in, the University of Göttingen.
- [53] C.B.a.M. Chergui, ultrafast x-ray absorption spectroscopy, *Chem. Rev.*, 104 (2004) 1781–1812.
- [54] V.D. J. Franck and G. Hertz, Photoelectric effect Hertz, *Phys. Ges.*, (1914) 457.
- [55] A. Einstein, quantum Photoelectric effect, *Ann. Physik*, 17 (1905) 132.
- [56] Wikipedia, Photoelectric effect, in, pp. https://en.wikipedia.org/wiki/Photoelectric_effect.
- [57] S. Hüfner, *Photoelectron Spectroscopy: Principles and Applications*, Springer, 2003.
- [58] I.L.a.W.E. SPICER, The probing depth in photoemission and Auger-electron spectroscopy, *Journal of Electron Spectroscopy and Related Phenomena*, 3 (1974) 409-413.
- [59] A. Damascelli, Probing the Electronic Structure of Complex Systems by ARPES, *Physica Scripta T109* (2004) 61–74.
- [60] B. Lv, T. Qian, H. Ding, Angle-resolved photoemission spectroscopy and its application to topological materials, *Nature Reviews Physics*, 1 (2019) 609-626.
- [61] H.Z. Damascelli A, Shen Z X. , Angle-resolved photoemission studies of the cuprate superconductor-2003, *REVIEWS OF MODERN PHYSICS*, 75 (2003) 473.
- [62] I. Adawi, Theory of the Surface Photoelectric Effect for One and Two Photons, *Physical Review*, 134 (1964) A788-A798.
- [63] L. Hedin, S. Lundqvist, Effects of Electron-Electron and Electron-Phonon Interactions on the One-Electron States of Solids, in, 1970, pp. 1-181.
- [64] A. Damascelli, Z. Hussain, Z.-X. Shen, Angle-resolved photoemission studies of the cuprate superconductors, *REVIEWS OF MODERN PHYSICS*, 75.
- [65] H. Iwasawa, K. Shimada, E.F. Schwier, M. Zheng, Y. Kojima, H. Hayashi, J. Jiang, M. Higashiguchi, Y. Aiura, H. Namatame, M. Taniguchi, Rotatable high-resolution ARPES system for tunable linear-polarization geometry, *J Synchrotron Radiat*, 24 (2017) 836-841.
- [66] Kenya Shimada, Masashi Arita, Yukiharu Takeda, Hiroyuki Fujino, Kenichi Kobayashi, Takamasa Narimura, Hirofumi Namatame, M. Taniguchi, High-resolution, Low-temperature Photoemission Spectroscopy At The Hisor Linear Undulator Beamline, *Surface Review and Letters*, 9 529–534.
- [67] D.S. SHOLL; J.A. STECKEL, *DENSITY FUNCTIONAL THEORY: A practical approach*.
- [68] P. Hohenberg, W. Kohn, Inhomogeneous Electron Gas, *Physical Review*, 136 (1964) B864-B871.

- [69] M.M. Georg Kresse, and Jürgen Furthmüller, VASP the GUIDE.
- [70] C.J. Cramer, Essentials of Computational Chemistry Theories and Models, Wiley, 2004.
- [71] V. Wang, N. Xu, J.-C. Liu, G. Tang, W.-T. Geng, VASPKIT: A user-friendly interface facilitating high-throughput computing and analysis using VASP code, Computer Physics Communications, 267 (2021).
- [72] G.K.J. Furthmüller, Efficient iterative schemes for ab initio total-energy calculations using a plane-wave basis set, Physical Review B, 54 (1996) 11169, 11169-11186.
- [73] J.F.b. G. Kresse, Efficiency of ab-initio total energy calculations for metals and semiconductors using a plane-wave basis set, Computational Materials Science, 6 (1996) 15-50.
- [74] B.K. Perdew John P., Wang Yue, Generalized gradient approximation for the exchange-correlation hole of a many-electron system, Physical Review B 54 (1996) 16533, 16533-16539.
- [75] W.B. Zhang, N. Yu, W.Y. Yu, B.Y. Tang, Stability and magnetism of vacancy in NiO: A GGA+U study, The European Physical Journal B, 64 (2008) 153-158.
- [76] X. Hou, M. Wumiti, S. Kumar, K. Shimada, M. Sawada, Observation of mid-gap states emerging in the O-terminated interface of Cr₂O₃/graphene: A combined study of ab initio prediction and photoemission analysis, Applied Surface Science, 594 (2022).
- [77] A. Rohrbach, J. Hafner, G. Kresse, Ab initio study of the (0001) surfaces of hematite and chromia: Influence of strong electronic correlations, Physical Review B, 70 (2004) 125426, 125421-125417.
- [78] H.J. Monkhorst, J.D. Pack, Special points for Brillouin-zone integrations, Physical Review B, 13 (1976) 5188-5192.
- [79] S. Grimme, Semiempirical GGA-type density functional constructed with a long-range dispersion correction, Journal of Computational Chemistry, 27 (2006) 1787-1799.
- [80] M. Fuentes-Cabrera, M.I. Baskes, A.V. Melechko, M.L. Simpson, Bridge structure for the graphene/Ni(111) system: A first principles study, Physical Review B, 77 (2008) 035405, 035401-035405.
- [81] W.B. Zhang, C. Chen, P.Y. Tang, First-principles study for stability and binding mechanism of graphene/Ni(111) interface: Role of vdW interaction, Journal of Chemical Physics, 141 (2014) 044708, 044701-044708.
- [82] F. Mittendorfer, A. Garhofer, J. Redinger, J. Klimeš, J. Harl, G. Kresse, Graphene on Ni(111): Strong interaction and weak adsorption, Physical Review B, 84 (2011) 201401, 201401-201404.
- [83] G. Bertoni, L. Calmels, A. Altibelli, V. Serin, First-principles calculation of the electronic structure and EELS spectra at the graphene/Ni(111) interface, Physical Review B, 71 (2005) 075402, 075401-075408.
- [84] A. Varykhalov, D. Marchenko, J. Sánchez-Barriga, M.R. Scholz, B. Verberck, B. Trauzettel, T.O. Wehling, C. Carbone, O. Rader, Intact Dirac Cones at Broken Sublattice Symmetry: Photoemission Study of Graphene on Ni and Co, Physical Review X, 2 (2012) 041017, 041011-041010.
- [85] A. Calloni, G. Berti, A. Brambilla, M. Riva, A. Picone, G. Bussetti, M. Finazzi, F. Ciccacci, L. Duo, Electron spectroscopy investigation of the oxidation of ultra-thin films of Ni and Cr on Fe(001), Journal of Physics: Condensed Matter, 26 (2014) 445001, 445001-445011.
- [86] L. Bignardi, P. Lacovig, M.M. Dalmiglio, F. Orlando, A. Ghafari, L. Petaccia, A. Baraldi, R. Larciprete, S. Lizzit, Key role of rotated domains in oxygen intercalation at graphene on Ni(1 1 1), 2D Materials, 4 (2017).
- [87] Z. Zhang, Q. Qian, B. Li, K.J. Chen, Interface engineering of monolayer MoS₂/GaN hybrid heterostructure: Modified band alignment for photocatalytic water splitting application by nitridation treatment, ACS Applied: Materials & Interfaces, 10 (2018) 17419-17426.
- [88] Q. Peng, Z. Wang, B. Sa, B. Wu, Z. Sun, Electronic structures and enhanced optical properties of blue phosphorene/transition metal dichalcogenides van der Waals heterostructures, Scientific Reports, 6 (2016) 31994, 31991-31910.
- [89] A. Grüneis, K. Kummer, D.V. Vyalikh, Dynamics of graphene growth on a metal surface: a time-dependent photoemission study, New Journal of Physics, 11 (2009) 073050, 073051-073059.
- [90] F.P. Fehlner, N.F. Mott, Low-Temperature Oxidation, Oxidation of Metals, 2, 1, 59-99 (1970).
- [91] S. Cao, N. Wu, W. Echtenkamp, V. Lauter, H. Ambaye, T. Komesu, C. Binck, P.A. Dowben, The surface stability of Cr₂O₃(0001), Journal of Physics: Condensed Matter, 27 (2015) 255003, 255001-255006.

- [92] C.A. Ventrice, Jr., D. Ehrlich, E.L. Garfunkel, B. Dillmann, D. Heskett, H. Freund, Metallic-to-nonmetallic transition of Na coadsorbed with CO₂ and H₂O on the Cr₂O₃(111)/Cr(110) surface, *Physical Review B*, 46 (1992) 12892-12895.
- [93] V. Maurice, S. Cadot, P. Marcus, XPS, LEED and STM study of thin oxide films formed on Cr(110), *Surface Science* 458 (2000) 195–215.
- [94] X. Li, L. Liu, V.E. Henrich, Resonant photoemission determination of the valence electronic structure of Cr₂O₃, *Solid State Communications*, 84 (1992) 1103-1106.
- [95] N.K. Sugawara H, Miya T, et al., Extreme ultraviolet photoemission from chromium metal, *Journal of the Physical Society of Japan*, 53(1): 279-283 (1984).
- [96] C. Oshima, A. Itoha, E. Rokuta, T. Tanaka, K. Yamashita, T. Sakurai, A hetero-epitaxial-double-atomic-layer system of monolayer graphene/monolayer *h*-BN on Ni(111), *Solid State Communications* 116 (2000) 37-40.
- [97] D. Usachov, O. Vilkov, A. Gruneis, D. Haberer, A. Fedorov, V.K. Adamchuk, A.B. Preobrajenski, P. Dudin, A. Barinov, M. Oehzelt, C. Laubschat, D.V. Vyalikh, Nitrogen-doped graphene: efficient growth, structure, and electronic properties, *Nano Lett*, 11 (2011) 5401-5407.
- [98] Y. Gamo, A. Nagashima, M. Wakabayashi, M. Terai, C. Oshima, Atomic structure of monolayer graphite formed on Ni(111), *Surface Science* 374 (1997) 61-64.
- [99] X. Sun, W. Li, X. Wang, Q. Sui, T. Zhang, Z. Wang, L. Liu, D. Li, S. Feng, S. Zhong, H. Wang, V. Bouchiat, M. Nunez Regueiro, N. Rougemaille, J. Coraux, A. Purbawati, A. Hadj-Azzem, Z. Wang, B. Dong, X. Wu, T. Yang, G. Yu, B. Wang, Z. Han, X. Han, Z. Zhang, Room temperature ferromagnetism in ultra-thin van der Waals crystals of 1T-CrTe₂, *Nano Research*, 13 (2020) 3358-3363.
- [100] X. Sui, T. Hu, J. Wang, B.-L. Gu, W. Duan, M.-s. Miao, Voltage-controllable colossal magnetocrystalline anisotropy in single-layer transition metal dichalcogenides, *Physical Review B*, 96 (2017).

Acknowledgement

First of all, I would like to show my highest respect to my supervisor, Sawada Masahiro, my supervisor. For his instructed me and helped me through all difficulties step by step. His profound knowledge, sharp thinking with patient and tolerant attitude, really let me thinking a lot of things beyond science. I learnt a lot from him, not only in experiment knowledge, data analysis, research skills, but also enlighten me to grow up to be a better researcher. His selfless dedication during the last 3 years is wealth of my entire life.

Besides, I would also like to show my sincerely gratitude to Kenya Shimada sensei, for encouraging and give me many valuable advices for the experiment, discussion and manuscript writing. During the last past three years, I met many excellent young people who strive for academics, Dr. Shiv Kumar, Dr. Ke Zhang, Dr. Shilong Wu, Dr. Mingtian Zhen, Dr. Xiaoxiao Wang, Dr. Masuer Wumiti, Amit Kumar, Cheng Zhang, et. al. Their enthusiastic and selfless support and discussion during my experiment help me growth.

I would also like to thanks myself. Although I struggled for a quite long time, the hope is never lost in my heart. I'm so glad that I've passed through the hardest time by myself, and the future is shining and hopeful. Last but not least, I would like to thanks my family and friends. Thanks for my beloved parents and my eld sister. Thanks for their always stand with me, thanks for understanding, encourage and support from all perspective. Thanks for my lovely cat, thanks for his unconditional love and accompany. Thanks for him waiting for me patiently no matter how late I come home. Thanks to my dear friends, Qingqing Lv, Fujuan Xu, Xue Jia, Qi Pei, and so on, for their listen to my situation and help when I'm depressed. Finally, I would like to thanks to dear

Mr. Shao. Thanks for your showing up just in time, your appearance making my PhD life becomes beautiful and colorful and become a full circle.

Xueyao Hou

June 2022

